

**Radiation Effects on Magnetic Tunnel Junctions and Novel Magnetic
thin Films**

A Dissertation presented to
the Graduate Faculty of the School of Arts and Sciences
University of Virginia

in Candidacy for the Degree of
Doctor of Philosophy (Department of Physics)

By
Nattawut Anuniwat

January 2015

TABLE OF CONTENTS

ACKNOWLEDGEMENT	vi
ABSTRACT	viii
FIGURE CAPTIONS	x
TABLE CAPTIONS	xvii
CHAPTER 1. Introduction.....	1
1.1 Motivation.....	1
1.2 Objectives	2
1.3 Dissertation Outline	3
CHAPTER 2. Background.....	5
2.1 Spintronics and MRAM.....	5
2.1.1 Discovery of giant magnetoresistance (GMR)	5
2.1.2 Magnetic tunnel junction (MTJ)	8
2.1.3 Spin torque transfer.....	13
2.2 Perpendicular material candidates for irradiation study	16
2.2.1 Crystalline L ₁₀ MnAl.....	16
2.2.2 Amorphous TbFeCo.....	17
2.2.3 Interfacial anisotropy of multilayer structures.....	21
2.3 Radiation damages in magnetic materials and structures	23
2.3.1 Radiation damages	23
2.3.2 Effects of radiation on magnetic materials	26
2.3.3 Effects of radiation on magnetic tunnel junctions	28

CHAPTER 3. Experiments	30
3.1 Structural characterizations.....	30
3.1.1 X-ray diffraction (XRD)	30
3.1.2 X-ray reflectivity (XRR).....	33
3.1.3 X-ray diffuse scattering.....	34
3.2 Atomic force microscopy.....	36
3.2.1 Surface morphology.....	36
3.2.2 Magnetic domain imaging	37
3.3 Magnetic property characterization	37
3.3.1 Vibrating Sample Magnetometer (VSM).....	37
3.3.2 Magneto optical Kerr effect.....	39
3.4 Transport Characterization.....	40
3.4.1 Hall bar device fabrication.....	40
3.4.2 Resistivity measurement	41
3.4.3 Magnetoresistance and Hall measurement.....	41
3.5 Pulse switching measurement.....	46
CHAPTER 4. Irradiation of perpendicular magnetic tunnel junctions.....	48
4.1 Introduction.....	48
4.2 PMTJ films stacks.....	48
4.2.1 CoFeB/MgO and Co/Pd superlattice	50
4.2.2 PMTJ stack.....	59
4.3 Effects of irradiations on PMTJ devices.....	64
4.3.1 Pre-irradiation characterization of PMTJ devices.....	64

4.3.2 Radiation species and the total fluence	69
4.4.3 Post-irradiation characterization	70
4.5 Summary	81
CHAPTER 5. L1 ₀ MnAl system	83
5.1 Introduction	83
5.2 Proton irradiation	83
5.3 Structural Characterization	84
5.3.1 Recovery of Chemical Ordering	84
5.3.2 Displacement damage and inter-diffusion	87
5.4 Postmortem magnetic Properties	90
5.5 Transport properties	94
5.5.1 Anomalous Hall Resistance (R_{XY}) and Magnetoresistance (R_{XX})	94
5.5.2 Electrical Resistivity	100
5.6 Summary	102
CHAPTER 6. Amorphous Rare earth—Transition alloys	103
6.1 Introduction	103
6.2 Pre-rad characterization	104
6.2.1 Structural and compositional determination	104
6.2.2 Magnetic properties	105
6.2.3 Strain-induced enhancement of coercivity	106
6.3 Irradiation of TbFeCo films	109
6.3.1 Simulation of proton irradiation	110
6.3.2 Electric properties after proton irradiation	111

6.3.3 Magnetic properties after proton irradiation	112
6.3.4 Magneto transport properties after proton irradiation.....	114
6.4 Summary	122
CHAPTER 7. Conclusions and future work.....	124
7.1 Summary	124
7.2 Suggested future work	127
BIBLIOGRAPHY	129

ACKNOWLEDGEMENT

This dissertation would not have been possible without the guidance and the help of several individuals who in one way or another contributed and extended their valuable assistance in the preparation and completion of this study.

First and foremost, I owe my deepest gratitude to both my advisors, Prof. Stu Wolf and Prof. Jiwei Lu who have tirelessly supported me throughout my thesis. Their guidance on research direction, writing manuscripts, or even lesson in life, is little by little, shaping me to become more independent researcher. With their patience and knowledge whilst allowing me the room to work in my own pace, one simply could not wish for a better or friendlier mentor.

I am also grateful to our collaborations: (NRL folks) Dr. Bradley Weaver, Dr. Patrick McMarr for providing irradiation sources and sharing their expertise on radiation effects. A long day with Pat in the lab is memorable. His work ethic and unique character are truly appreciated. I also want to express gratitude to Dr. Eugene Chen from Samsung (Formerly Grandis Inc.) for providing samples and stimulated discussion during teleconference. I would like to thank Prof. Joe Poon and his group (Manli Ding, Xiaopu Li) for providing amorphous samples and characterizing samples. I'm really appreciated! I'd also like to thank Prof. Blaine Norum who served as my thesis committee in such a short notice.

I also want to thanks Wolf/Lu's group members for making the lab such a wonderful work place. Dr. Nam Dao, I'll remember our time in the lab together. Your profound knowledge and advices are very much appreciated. Mandy Gu, please enjoy your time at IBM, you are a good scientist, Let them know that! Linqiang (Collins!)..that's how I stumbled to get your name, my advice to you is always writing!

Yuhan Wang, Karen Freedy, keep on working hard and don't hesitate to ask for helps when you really need them. I'd like to express my special appreciation to the group alumni :Yishen Cui, I wish you a great success in your life (all the best to little Amy as well); Ryan Comes, I hope your professor career will soon begin (Go Hoos!); Hongxue Liu, Wei Chen I wish a great success in your career.

I like to thanks my best friends, Kiadtisak Saenboonruang and Parinya Anantachaisilp. It was a pleasure to become friends with you gentleman for over a decade! I'll cherish all the memories we have created here at UVa. One could never ask for a better friend. There are so many people I may not mention such as Thai community, physics folks, etc. I'd like to thank you all and wish you the best!.

In the end, I'd also like to dedicate a very special gratitude to Salinporn (Lin) Kittiwatanakul for your support in everyway. Your patience, kindness and love help me get through some difficult times my life. Over a decade we knew each other, I am happy every single day. You are truly my "everything". Now that I am away, all I want for you is taking care of yourself better so that you can finish your first marathon! I'd also like to express my gratitude to my parents and my sister for their unconditional love and supports. I'd like to dedicate this dissertation to my dear family and DPST scholarship. Without them, I would not been able to come here and earn my Ph.D. I promised I will do my best to serve my country.

ABSTRACT

Spintronics, which utilizes spin polarized currents in memory and logic device, promises new paradigms for information processing and storage. However, the spin-related disordering effect caused by the irradiation has not been systematically investigated for ferromagnetic materials. The first generation of Magnetoresistive Random Access Memory (MRAM) is known to be “Rad hard”. However, advances in the magnetic nanostructures and new materials for the scalability of MRAM and other potential applications require a re-evaluation of their radiation hardness.

In this dissertation, as the key elements for the MRAM technology, the Spin Transfer Torque – Magnetic tunnel junction (STT-MTJ) devices with perpendicular magnetic anisotropy along with novel magnetic materials have been examined. Various radiation sources, including protons, Neon ions, and x-rays are used to irradiate the MTJ devices followed by the characterization of critical metrics for the device performance such as TMR, the device retention, and the switching currents to identify plausible failure mechanisms in MTJ devices associated with the irradiation species. The STT-MTJ shows “Rad Hard” properties after irradiation with the fluence and total ionization doses (TID) beyond CMOS threshold standard. The localized annealing, which is a by-product of the ionization process, improves the crystallinity of the MgO tunnel barrier that results in the small but appreciable increase of TMR after the accumulated irradiation of 10keV-energy x-ray with TID of 1 Mrad. The MTJ devices also maintain their normal functions after exposing to 2 MeV-energy Neon ions and protons separately. However, after proton irradiation, two of 60 nm devices exhibited unstable behavior during the retention test, which may be caused by the trapped charges.

Proton radiation affects the highly ordered $L1_0$ MnAl system by which the modification of magnetic properties results from the combined effect of irradiation-induced thermal annealing and atomic displacement. A highly ordered pre-rad MnAl is more susceptible to displacement damages which manifests itself in a continuing reduction of chemical ordering with irradiation doses going from $S \sim 0.97$ to ~ 0.8 to ~ 0.72 at a total fluence $\sim 1 \times 10^{15} \text{ H}^+/\text{cm}^2$. After the final irradiation with the total fluence $2 \times 10^{15} \text{ H}^+/\text{cm}^2$, the change in the chemical ordering reverses and S becomes ~ 0.81 , which results from the thermal annealing induced by the high fluence proton beam.

In amorphous TbFeCo materials, both the displacement and ionization damage are observed. The displacement damages are displayed through small enhancements of the coercive field, and an increase of resistance as the material becomes more porous. Meanwhile, the changes of the magnetic properties such as the magnetization, the compensation temperature can be attributed to the ionization damages.

FIGURE CAPTIONS

Figure 2.1 Schematic of spin dependent transports through different configurations, parallel(P) and antiparallel(AP) of “spin valve” structure	5
Figure 2.2 (a) Schematic density of state (DOS) of ferromagnet Co filled with spin-up and spin-down electron at Fermi level. The numbers indicate magnetic moment of each band(adapted from lecture note “Spin Transport, Dynamics and Quantum information” Prof.Stu Wolf, UVa 2013) (b) spin polarized current after passing ferromagnetic material (adapted from W. Chen, PhD dissertation: Structural and Material Exploration of Magnetic Tunnel Junctions. UVa 2010)	7
Figure 2.3 Schematic of electron tunneling in MTJ with different magnetic configurations (adapted from lecture note “Spin Transport, Dynamics and Quantum information” Prof.Stu Wolf, UVa 2013).....	9
Figure 2.4 (a) comparison of tunneling process in amorphous Al-O based and crystalline MgO-based MTJ (adapted from[21]) (b) Tunneling DOS of majority-spin states in Fe/MgO (8ML)/Fe with parallel magnetic state(adapted from ref [24])	11
Figure 2.5 1T1MTJ architecture of 1 bit MRAM with read and program modes (adapted from lecture note “Spin Transport, Dynamics and Quantum information” Prof.Stu Wolf, UVa 2013).....	12
Figure 2.6 Spin torque transfer in F/I/F structures. The red layer is the fixed layer while the blue layer represents the free layer (adapted from ref [13])	14
Figure 2.7 Reduced $L1_0$ structure to distorted B2 structure (Courtesy to Yishen Cui) ...	16
Figure 2.8 (a) Schematic of ferrimagnetism, rare-earth and iron group couple antiferromagnetically(adapted from ref[58]) (b) temperature dependence of sublattices’	

magnetization. The moment of ferrimagnetic materials is the net moment of each sublattice. Two critical temperatures occurred where the magnetic moment disappear including compensation temperature(T_{Comp}) and Curie temperature (T_C) (adapt from ref [59]).....	19
Figure 2.9 Composition dependence of magnetic properties of TbFeCo with Tb content from 15 - 35 atomic %	20
Figure 3.1 Schematic of basic XRD geometry on material with lattice spacing d	31
Figure 3.2 Schematic of $2\theta/\omega$ scan in Rigaku SmartLab XRD tool (adapted from ref[98])	31
Figure 3.3 (a) XRR profile of ITO film on glass substrate (b) FFT of the XRR. The numbers on top of the peaks show the calculated layer thicknesses. The numbers in the parentheses show the depth from the surface	34
Figure 3.4 Schematic of rocking x-ray diffraction scattering measurement. The 2θ angle is fixed while angle of incidence ω vary from 0 to 2θ	35
Figure 3.5 Schematic of the basic AFM mechanism (adapted from Http://Commons.Wikimedia.org/Wiki/File:AFM_Schematic_(en).Svg (n.d.).)	37
Figure 3.6 Schematic of 3 basics configurations of Kerr effect: (a) polar Kerr; (b) longitudinal Kerr; (c) transverse Kerr (adapted from ref[105]).....	39
Figure 3.7 A Hall bar device with (a) Hall measurement configuration (b) magnetoresistance configuration	42
Figure 3.8 Comparison of side jump mechanism (a) characterized by displacement Δy of carrier trajectory (b) skew scattering characterized by Hall angle θ_S (adapt from ref[107])	43

Figure 3.9 Schematic of pulse switching measurement set up	46
Figure 4.1 Schematic of the complete pMTJ structure. Two ferromagnetic structures consist of CoFeB/MgO (free layer: sample#1) and CoPd superlattice (SAF layer: sample#2) are investigated individually.	49
Figure 4.2 AFM images of unirradiated and samples irradiated with $1 \times 10^{14} \text{ H}^+/\text{cm}^2$. G1A: CoFeB/MgO; G3A: [Co/Pd] superlattice.....	51
Figure 4.3 X-ray reflectivity spectra of (a) CoFeB/Mgo sample and (c) Co/Pd superlattice sample pre- and post- proton irradiation. The corresponding FFT of CoFeB/MgO and Co/Pd sample are also illustrated in (b) and (d) respectively.	53
Figure 4.4 Semi-log plots of X-Ray diffusion scattering curve for 2θ fixed at 3° of CoFeB/MgO sample (a) and Co/Pd supperlattice sample (b)	56
Figure 4.5 In-plane hysteresis loops of virgin and irradiation for G1A (a) and G3A (c) samples and MOKE measurement of G1A (b) and G3A (d)	58
Figure 4.6 AFM images over 20 by 20 μm^2 of (a) as received, (b) total fluence of $1 \times 10^{15} \text{ H}^+/\text{cm}^2$ and (c) total fluence of $5 \times 10^{15} \text{ H}^+/\text{cm}^2$ respectively.....	60
Figure 4.7 Pre-rad and post-rad x-ray reflectivity comparison of PMTJ#1 is shown in (a) and PMTJ#2 in (c) The corresponding FFT of PMTJ#1 and PMTJ#2 samples are demonstrated in (b) and (d) respectively. The dash lines represent capping layer interface and seeding layer interface.....	61
Figure 4.8 XDS curves of PMTJ#1 at fixed $2\theta = 2.01^\circ$ (a) and 2.89° (b)	62
Figure 4.9 MOKE measurement of PMTJ as a function of proton total fluence. MOKE loopers demonstrate that PMA of PMTJ is unaffected by irradiation up to $5 \times 10^{15} \text{ H}^+/\text{cm}^2$	63

Figure 4.10 Devices layout with diameter ranging from 20 – 500 nm. Each devices are labeled according to their position including flash field(F), block(B) , column(C) and row(R).	64
Figure 4.11 Schematic of side view and top view of pMTJ device.	65
Figure 4.12 Functionality test result of a 150 nm pMTJ device represents switching characteristic. A sequence is defined as a negative voltage pulse and current measurement at 25 mV followed by a positive voltage pulse to change resistance state and same current measurement at 25 mV	66
Figure 4.13 (a) R_{High} and R_{Low} of PMTJ devices as a function of the device size. The resistance data is from the conversion of current measurement from functionality test (b) Average TMR of PMTJ devices as a function of device size.	68
Figure 4.14 (a) Functionality test of a 70nm device pre-rad and post-rad (1Mrad) (b) retention tests on the same device pre-rad and post-rad comparison. The device was pre-set to high current state. Additional low current state retention was performed only for this device.	71
Figure 4.15 (a) A comparison of TMR (calculated from functionality data) plot as a function of device sizes (b) Change in TMR as a function of device sizes after the x-ray exposure	72
Figure 4.16 Retention test on 60 nm device after proton exposure. The device exhibits an unstable state that randomly switches between the high and low resistance states during repeated read.	75
Figure 4.17 Functionality test of the same 60nm device shows that the device failed to switch after write voltage pulse was applied around the 83 th cycle	75

Figure 4.18 (a) TMR vs. Device size for before and after proton irradiation. The total fluence is $1 \times 10^{12} \text{ H}^+/\text{cm}^2$. (b) ΔTMR of devices after Neon exposure.....	76
Figure 4.19 (a) Comparison pre-rad and post Neon exposure TMR value as a function of device size (b) TMR variation of devices after Neon fluence $1 \times 10^{11} \text{ ions}/\text{cm}^2$	79
Figure 4.20 (a) TMR vs. device size before and after Neon fluence $1 \times 10^{12} \text{ ions}/\text{cm}^2$ (b) ΔTMR of devices after Neon exposure.....	80
Figure 5.1 (a) XRD spectra of a 30 nm thick MnAl film for different irradiation fluences; (b) Chemical ordering as a function of total fluence (TF).....	85
Figure 5.2 SIMS results of Ta (5 nm) /MnAl (30 nm) /MgO (substrate) (a) before the irradiation; (b) after the irradiation with 2 MeV proton with the total fluence of $2 \times 10^{15} \text{ cm}^{-2}$ (right). The dashed lines correspond to the approximation positions of the Ta/MnAl interface.....	88
Figure 5.3 (a) 3-D simulation of 2 MeV proton range in Ta/MnAl/MgO test structure. The average range is 28.5 μm . (b) Depth profile of induced defects showing the Ta/MnAl and MnAl/MgO interface (Courtesy of B.Weaver)	89
Figure 5.4 Recoil distributions of Mn and Al showing intermixing with the Ta and MgO layers (Courtesy of B.Weaver)	90
Figure 5.5 (a) Perpendicular normalized magnetization curves of the MnAl film for pre- and post-irradiation measured at room temperature by MOKE. (b) Saturation moment (M_S) as a function of total fluence (TF).....	91
Figure 5.6 Magnetic force microscope images of (a) Virgin and (b) after the total fluence $2 \times 10^{15} \text{ p}^+/\text{cm}^2$	92
Figure 5.7 Illustration of the disordering process in the BCT structure	93

Figure 5.8 (a) Hall resistance (R_{xy}) mimics the out-of-plane magnetization loop nicely (b) Hall resistance vs. Magnetic field (H) measured as a function of total fluence at 300 K. The same Hall bar device was measured after each exposure to the proton beam.	94
Figure 5.9 Magneto-resistance of Hall device: sample structure [Ta (5 nm) /MnAl (30 nm) /MgO(substrate)] as a function of total fluence(TF) of proton irradiation. (a) at 300K and (b) at 50K.	96
Figure 5.10 (a) $\rho_{xx}\rho_{xy}$ vs ρ_{xx} plot of various total fluence show linear relationship following the scaling equation of AHE nicely. (b) The evolution of skew and side-jump scattering coefficient as a function of total fluence.	98
Figure 5.11 Temperature dependence of the normalized resistances for virgin and irradiated MnAl Hall bar device.	100
Figure 5.12 MR% of irradiated and virgin Hallbar measured at 2K.....	101
Figure 6.1 (a) Bright field TEM image of a 35 nm TbFeCo film deposited on SiO ₂ /Si. A 15 nm MgO layer was used to cap the film; (b) HRTEM image of the TbFeCo film. The inset is a FFT pattern of the image. (Courtesy of M. Ding).....	104
Figure 6.2 In-plane and out-of-plane hysteresis loops of virgin sample.....	106
Figure 6.3 (a) Hall resistance vs. magnetic field for two Hall bar devices with the widths of 50 and 500 μm at room temperature (b) Coercive field vs. 1/width of Hall bar for TbFeCo films with various thicknesses measured at room temperature.	106
Figure 6.4 SRIM simulation results (a) depth profile of film structure reveals large cascades in TbFeCo layer (b) Zoom-in image of the large cascade (c) Tb recoil distribution is influenced by the large cascade signature (Courtesy of B.Weaver)	110

Figure 6.5 Resistance ratio of the irradiated and the virgin Hall bar at room temperature	111
Figure 6.6 Comparison of pre-rad and post-rad measurement. (a) In-plane measurement of magnetization vs. magnetic field of $Tb_{30}Fe_{63.5}Co_{6.5}$ with 35nm thickness and (b) Saturation moment vs. temperature as a function of proton fluence.	112
Figure 6.7 Pre-rad and post-rad comparison of (a) coercive field (H_C) and (b) Hall resistivity (ρ_H) as a function of temperature	115
Figure 6.8 Atomistic simulation of sublattices' moment of $Tb_{30}Fe_{63.5}Co_{6.5}$ as a function of temperature. T_{comp} defined as the temperature in which exhibit lowest net magnetization $\sim 350\text{ C}^\circ$ (Courtesy of Xiaopu Li).....	118
Figure 6.9 (a) Magnetoresistance of 50 μm and 500 μm wide Hall bars at 300K. Two antisymmetric peaks occurred around H_C (b) Normalized MR of 500 μm wide Hall bar as a function of radiation total fluence.	120

TABLE CAPTIONS

Table 2.1 Radiation damages on materials (adapted from ref [80]).....	25
Table 4.1 2MeV-energy Proton irradiation procedure and total fluence (TF).....	50
Table 4.2 Comparison of FFT Peaks before and after irradiation for CoFeB/MgO sample.	54
Table 4.3 CIPT measurement of PMTJ stack	64
Table 4.4 Pre-rad device-to-device variability of high and low resistance state of MTJ devices.....	67
Table 4.5 Various irradiation sources and their corresponding damages that performed on PMTJ devices.....	70
Table 4.6 Comparison of ability to absorbed x-ray and first ionization energy of individual PMTJ materials.....	73
Table 4.7 Estimated total number of proton hits per device	74
Table 4.8 Radiation Hardness evaluation of STT-MTJ with perpendicular magnetic anisotropy.....	82
Table 5.1 Irradiation procedures and the total fluence.....	84
Table 5.2 Chemical ordering (S) and peak parameters of (001) and (002) extracted from XRD spectra of MnAl thin films	86
Table 6.1 Proton irradiation procedure on TbFeCo materials.....	109

CHAPTER 1. Introduction

1.1 Motivation

“Ferromagnetic and ferroelectric solids can contain imperfections in the form of spin disorder but in the interest of simplicity, we shall omit such topics from detailed consideration...” F. Seitz, in *Imperfections in Nearly Perfect Crystals* published in 1952[1].

For the current society that is filled with the enormous interactive information from very complex calculations to “Big Data” to enormous social media interactions, it is vital for the technology to adapt for faster processing, fast growing data and low power consumption. Tremendous efforts on semiconductor-based technologies are made to maintain Moore’s Law. Even so, the Si based CMOS technology is near the end of “scaling”[2-4].

Spintronics emerges as a new paradigm for information processing and storage[5-8]. Compared to charge based electronics, the advantages of magnetism/spin based devices include non-volatility and the ultra low power consumption. The first generation Magnetic Random Access Memory (MRAM) is known to be “Rad Hard” and considered to be critical components for space and military systems, for which it maintains functionality in the harsh radiation environments[9]. Enabling the proper “scaling” of MRAM, the Spin Torque Transfer -Magnetic Tunnel Junction (STT-MTJ) has been the key focus for the next generation MRAM, and new magnetic materials are being developed to improve the performance of STT-MTJ. Therefore, advancements in the new

materials for the scalability of MRAM and for other potential applications require a careful examination for their performances under irradiation.

Since Seitz's "assertion" in 1952[1], scientists seem to adopt a habit of ignoring the effects of disorders on the spin and the magnetism. For nearly 60 years, the understanding of what irradiation does to matter has advanced very little.

The goal of this dissertation is to understand the potential impact of radiation on the magneto-transport, particularly on the spin torque transfer (STT) phenomenon in magnetic nanostructures including magnetic tunnel junctions (MTJs) and the magnetism of novel ferromagnetic materials respectively. Such very basic understanding will have a broad impact on advancing the science for novel radiation effects in spin-related electronics materials, as well as the potential implementation of spintronic devices in harsh environments like the outerspace.

1.2 Objectives

The overall goal is to investigate effects of irradiations including displacement damage and ionization damage on magnetic and structural properties and to understand what factors control the radiation hardness of magnetic thin films and multilayers in nanoscale spin-based devices. Several perpendicular magnetic anisotropy material systems are identified for potential spintronic applications namely crystalline $L1_0$ MnAl, amorphous rare earth-iron-cobalt (RE-Fe-Co), and interfacial anisotropy CoFeB/MgO and Co/Pd multilayers. The large difference in their microstructures and the origins of their magnetic anisotropies offers a wide range of magnetic properties and microstructures for comparison. The outcome of this project will not only establish the scientific principles for improving the radiation hardness of magnetic nanostructures and

perpendicular magnetic thin films, but also identify the strategies to mitigate the radiation damage to spin based devices.

Specific goals include:

1. To evaluate radiation hardness of perpendicular STT-MTJ devices.
2. To establish an understanding of irradiation effects on perpendicular magnetic materials.
3. To determine if irradiation could be utilized as an investigation tool/ modification tool in magnetic materials.

1.3 Dissertation Outline

This dissertation is devoted to the study of radiation effects on STT-MTJ devices and novel magnetic materials with perpendicular magnetic anisotropy. Both the displacement and ionization damages have been examined.

Chapter 2 provides a brief introduction of spintronics and MRAM followed by the introduction of PMA materials. It also introduces the basics of radiation damages and surveys prior studies on MTJ and magnetic materials.

Chapter 3 describes the experimental techniques including thin film fabrication, processing and characterization methods used in this work.

Chapter 4 focuses on the “Rad Hard” evaluation of STT-MTJ devices. A keys magnetic elements as well as the MTJ stack were characterized. The STT-MTJ devices are exposed to multi-specie ion irradiation including x-ray, heavy ions, and proton.

Chapter 5 describes proton irradiation effect on $L1_0$ MnAl with initially high chemical ordering. The proton irradiation is applied to study the displacement damage on the microstructures and the magnetic properties of MnAl with high chemical orderings.

The effect of thermal annealing associated with the irradiation process will be discussed as the side effect for the partial recovery of the chemical ordering which is reduced as the result of 2 MeV proton irradiation.

Chapter 6 discusses the proton irradiation effects on TbFeCo thin films with amorphous structure. The as-deposited TbFeCo thin films are amorphous ferrimagnets with a very strong magnetic anisotropy. The evolution of the magnetic properties reveals the change in the microstructure of the amorphous films caused by the 2 MeV protons.

Chapter 7 summarizes major results and discoveries, and suggests strategies and future directions.

CHAPTER 2. Background

2.1 Spintronics and MRAM

The term “spintronics” refers to multidisciplinary fields of physics that involve the manipulation, storage, and transfer of information by means of electron spins in addition to or in place of the electron charge as in conventional electronics[5]. With the end of the CMOS era in sight, spintronics has become a promising candidate due to its low power dissipation, non-volatility, and the possibility of integrating memory and logic into a single device.

2.1.1 Discovery of giant magnetoresistance (GMR)

The major advances in spintronic devices started in the late 1970s to 1980 following the discovery of large low temperature magnetoresistance in metallic superlattices[10,11]. In 1988, the discovery of giant magnetoresistance (GMR) at room temperature marked the breakthrough [10]. The resistance in these structures is lowest when the magnetic moments of the alternating ferromagnetic layers are parallel and highest when they are antiparallel.

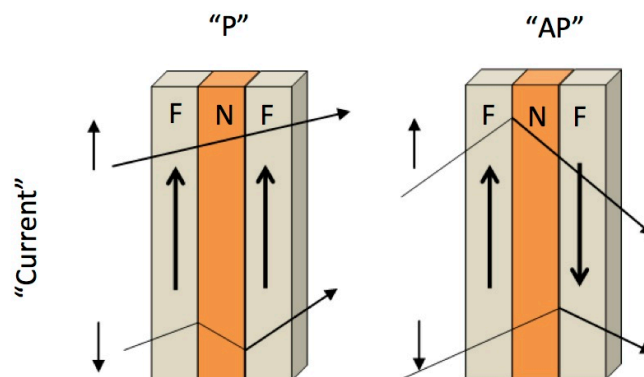


Figure 2.1 Schematic of spin dependent transports through different configurations, parallel(P) and antiparallel(AP) of “spin valve” structure

The spin dependent transport in ferromagnets was first explained by Mott in 1936[12]. He realized that at sufficiently low temperatures, where magnon scattering becomes negligible, electrons of majority and minority spins, with magnetic moment parallel and antiparallel to the magnetization of a ferromagnet, respectively, do not contribute to the scattering processes. The resistivity then is the sum of two unequal parts for two different spins—the current in ferromagnets is spin polarized. Now with regard to the GMR structure as shown in **Figure 2.1**, the resistance of the structure for a parallel and an antiparallel magnetic moment configuration is low and high, respectively. The magnetoresistive ratio (MR) can be defined as the ratio of the change in resistivity to the resistivity in the parallel orientation.

$$MR = \frac{R_{AP}-R_P}{R_P} \quad 2-1$$

The two spin channels of the electric current (spin up and spin down electrons) have different scattering probabilities depending on a layer-dependent and its relative strength as well as orientation to those of transported spins. The total resistance is the result of the electron scattering from inhomogeneous magnetic media which can be approximated by Fermi's golden rule[13]

In the case of ferromagnets, the resistance induced by *s* band to *d* band scattering is dominant compared to the resistance induced by *s* band to *s* band, provided the DOS of *3d* band dominates the DOS of *4s* band at the Fermi level. Additionally, the shift within the *3d* bands leads to an imbalance of the DOS at the Fermi level between the spin-up band and the spin-down band. According to the Fermi's golden rule, electrons experience a much stronger scattering from the spin-down band (minority) than that from the spin-up

band (majority) as in the case shown in **Figure 2.2a**. Consequently, the electric current is spin-polarized after passing through the ferromagnetic material as shown in **Figure 2.2b**.

The spin polarization of materials is then defined as

$$P = \frac{N_{\uparrow} - N_{\downarrow}}{N_{\uparrow} + N_{\downarrow}} \quad 2-2$$

where $N_{\uparrow,\downarrow}$ is DOS of electron spin up and spin down at Fermi level.

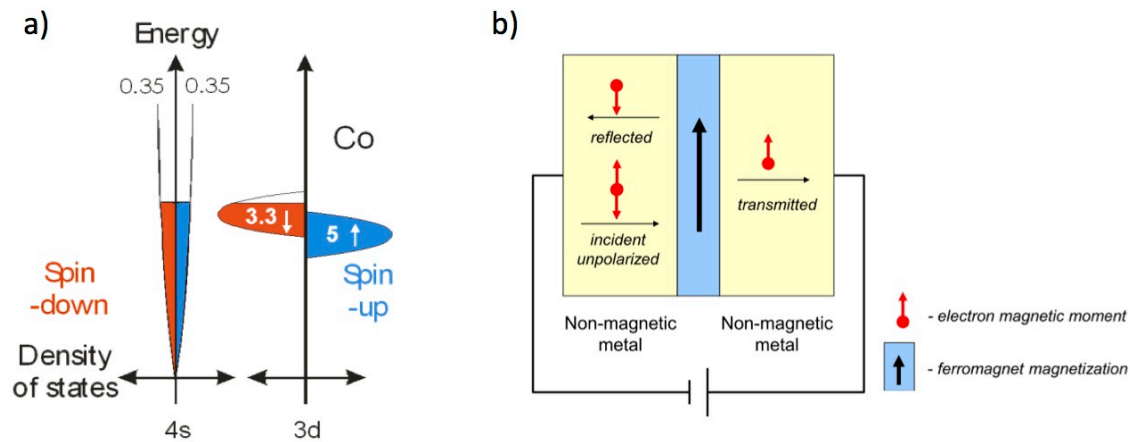


Figure 2.2 (a) Schematic density of state (DOS) of ferromagnet Co filled with spin-up and spin-down electron at Fermi level. The numbers indicate magnetic moment of each band (adapted from lecture note “Spin Transport, Dynamics and Quantum information” Prof. Stu Wolf, UVA 2013) **(b)** spin polarized current after passing ferromagnetic material (adapted from W. Chen, PhD dissertation, UVA 2010)

With better understanding of the GMR mechanism, researches quickly shifted toward applications such as magnetic sensors[14]. Spin valves exhibit significant changes in resistivity when subjected to relatively small external magnetic fields that makes them suitable for magnetic field sensors as in the read head in the Hard Disk Drive (HDD). The use and development of GMR structures for the read head was responsible for the very rapid growth in magnetic storage densities. The GMR of the spin valve structure remains below $\sim 20\%$ at room temperature even with the current-perpendicular-

to-plane (CPP) configuration[15], which limited its applicability for the memory application.

2.1.2 Magnetic tunnel junction (MTJ)

Spin dependent tunneling was first discovered by Tedrow and Meservey in a series of experiments in ferromagnet/insulator/superconductor (F/I/S) junctions[16,17]. These experiments showed that conduction electrons in ferromagnetic materials are spin-polarized and the total spin is conserved during the tunneling process. In 1975, Julliere studied the tunneling conductance of a ferromagnet/insulator/ferromagnet (F/I/F) where the insulator was an amorphous Ge layer[18]. **Figure 2.3** shows the spin-dependent tunneling electron model through magnetic tunnel junction (MTJ) with different magnetization configurations i.e. parallel (P) and antiparallel (AP) states. During the tunneling process, spin is conserved and tunneling probability is higher with P states, where electrons find more free states to tunnel to, compared to AP state. The current I_P and I_{AP} in P and AP states can be expressed as follows:

$$I_P = N_{\uparrow}^1 N_{\uparrow}^2 + N_{\downarrow}^1 N_{\downarrow}^2 \quad 2-3$$

$$I_{AP} = N_{\uparrow}^1 N_{\downarrow}^2 + N_{\downarrow}^1 N_{\uparrow}^2 \quad 2-4$$

where the superscript 1,2 correspond to ferromagnetic layers. The corresponding tunneling magnetoresistance (TMR) in an F/I/F type structure, called magnetic tunnel junction (MTJ), can also be express in the form of spin polarization as

$$TMR = \frac{R_{AP}-R_P}{R_P} = \frac{2P_1P_2}{1-P_1P_2} \quad 2-5$$

where the resistances R are labeled by the relative orientation P or AP of the magnetizations and P_1, P_2 are spin polarizations of ferromagnets F1, F2 respectively .

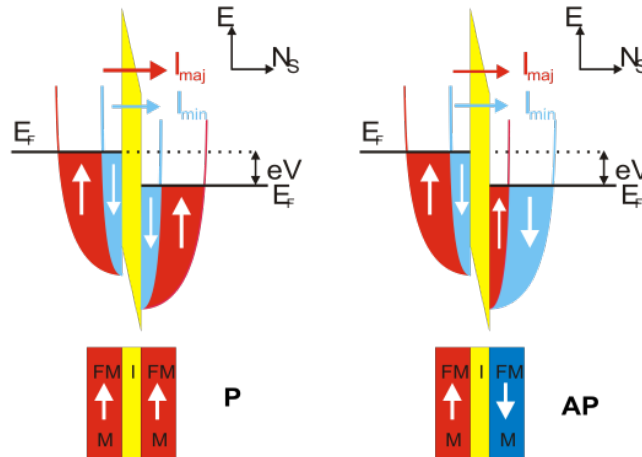


Figure 2.3 Schematic of electron tunneling in MTJ with different magnetic configurations (adapted from lecture note “Spin Transport, Dynamics and Quantum information” Prof.Stu Wolf, UVa 2013)

The demonstration of the room temperature TMR in 1995 attracted a great deal of interest [19,20]. In Julliere’s model, TMR is only determined by the spin polarizations of the ferromagnetic electrodes regardless of the barrier layer. However a discrepancy was noticed between the theoretical and experimental estimations for the MR ratios in MTJs with amorphous Al-O tunnel barriers[21]. The room-temperature TMR ratio hit a limit ~70% with an Al-O barrier[22] and didn’t show any increase with electrodes of higher spin polarizations[23].

In 2001, Butler et.al. predicted a coherent spin-dependent tunneling in MTJ with a crystalline tunnel barrier MgO(001) that could provide an additional spin filtering and enhance the MR to over 1,000 %[24]. This prediction was soon confirmed experimentally by two different groups independently[25,26]. In MgO-based tunnel junctions, the coherent tunneling process is expected to be the majority of electron tunneling process due to the high crystallinity of the MTJ structure. Evanescent states with three kinds of symmetries, Δ_1 , Δ_5 and Δ_2 , exist in the band gap along MgO (001). Given that the state

symmetries are conserved during tunneling, the Bloch states couple to the evanescent states through their corresponding symmetries and tunnel through the barrier with different tunneling probabilities. The Δ_1 state has the slowest decay along MgO (001) direction and the electron tunneling with Δ_1 symmetry becomes dominant with a large positive spin polarization. Other states with a negative spin polarization, Δ_5 and Δ_2 , decay much faster, hence the lower tunneling probability, therefore, the spin polarization after averaging is higher than the case of an amorphous barrier where the tunneling probability of evanescent state is comparable such that averaging does not raise the net spin polarization[24,27].

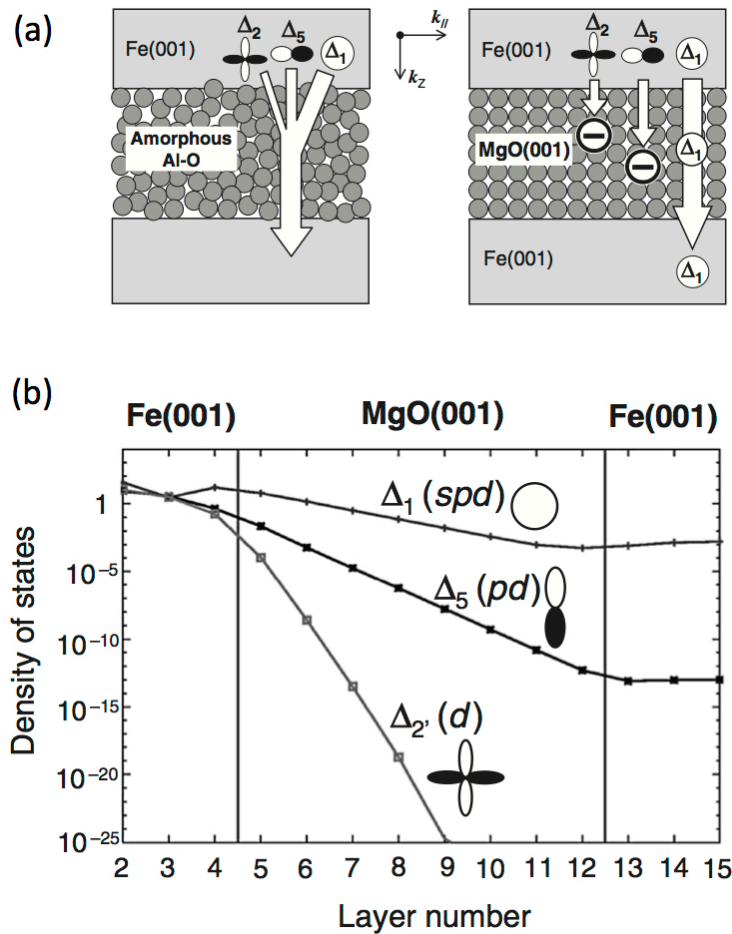


Figure 2.4 (a) comparison of tunneling process in amorphous Al-O based and crystalline MgO-based MTJ (adapted from[21]) **(b)**Tunneling DOS of majority-spin states in Fe/MgO (8ML)/Fe with parallel magnetic state(adapted from ref [24])

As a result, the MTJ research and development shifted toward MgO-based MTJs for memory and other applications. By optimizing the composition of CoFeB, recently TMR ratios of more than 700% have been achieved at room temperature (RT) in CoFeB/MgO/CoFeB MTJs[28].

2.1.3 Magnetic random access memory (MRAM)

Magneto-resistive random access memory (MRAM) is based on the concept of using the relative direction of magnetization states (“AP” and “P” may be assigned to “1” and “0”) to store information, and magneto-resistance for readout i.e. high and low

resistance[6]. **Figure 2.5** illustrates a MRAM bit architecture enabling one MTJ element and one transistor bit cell (1T1MTJ) with large tunnel magnetoresistance (TMR) [25,26]. In the read mode, the transistor is switched “ON” allowing read current to pass through the MTJ and recognize the resistance state. In the program mode, the isolation transistor is in ‘OFF’ position. Currents are sent through the bit line and digit line, which are orthogonal to each other, generating external magnetic fields to manipulate the magnetization direction of the free layer.

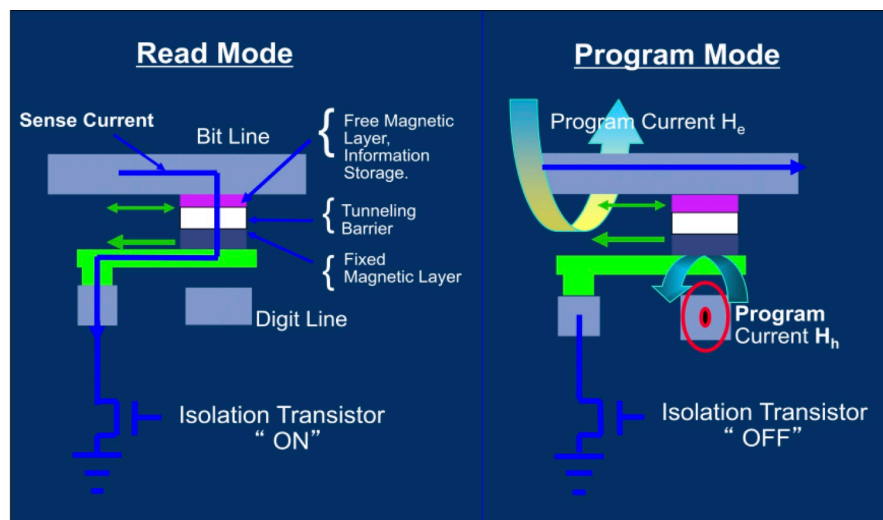


Figure 2.5 1T-1MTJ architecture of 1 bit MRAM with read and program modes (adapted from lecture note “Spin Transport, Dynamics and Quantum information” Prof.Stu Wolf, UVA 2013)

The MRAM chip product prototype with the toggle magnetic field switching scheme was announced in 2003 and the first ever MRAM commercial products started to ship in 2006[29]. The manufacturability of MTJ devices as memory bits was proven in these nonvolatile MRAM products, having high read and write speeds (10’s of ns) and

nearly unlimited endurance. With fast growing technology, high packing density that translates into smaller bit of MRAM is required. A major problem arises, as the conventional MRAM is not scalable to the memory bit size below 65 nm. The retention time, which is the vital factor of magnetic memory, requires ~ 10 years of lifetime. For magnetic recording, the retention time is defined by thermal stability

$$\Delta = \frac{K_U V}{k_B T} \quad 2-6$$

where K_U is magnetic anisotropy of the FL, V is FL's volume and k_B Boltzmann constant and T temperature. It becomes obvious that magnetic anisotropy needs to be increased significantly for the FL when the bit size is reduced. However, the increase in the magnetic anisotropy also requires a large magnetic field to switch it. This translates to larger CMOS devices to provide higher current in the bit and write lines to generate the required magnetic field for the bit switching. The two requirements contradict with each other and one can't scale the MTJs and CMOS devices for MRAM simultaneously[13].

2.1.3 Spin torque transfer

Thanks to spin torque transfer (STT) that utilizes a torque carried by spin polarized current to directly switch the magnetization of a nanomagnet, the scalability problem for MRAM can be resolved. STT was first predicted in 1996 by Slonczewski [30], and based on a generally accepted argument: for a system consisting of itinerant electrons and local moments, the total angular momentum is conserved even when the system is out of equilibrium[30,31]. The STT mechanism is illustrated in **Figure 2.6** within a MTJ structure frame[13]. The ferromagnetic RL serves as spin-polarizer, aligning the spin of the current towards its magnetization. As the polarized spins tunnel through the insulator and reach the FL, the s - d exchange interaction again quickly aligns

the spins towards the local magnetization of the FL[32]. On the other hand, the transverse magnetic moments carried by the electrons are transferred to the FL, this torque provided by conservation of angular momentum, tilts the magnetization of the FL towards that of the RL, and eventually cause the magnetization reversal in FL.

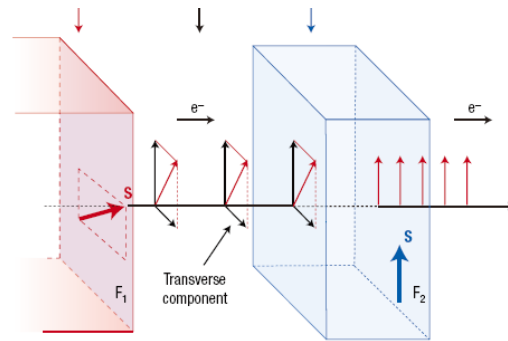


Figure 2.6 Spin torque transfer in F/I/F structures. The red layer is the fixed layer while the blue layer represents the free layer (adapted from ref [13])

The theoretical expression of this critical current density J_{c0} required to switch the magnetization of a ferromagnet is given by equation [33-35]

$$J_{c0} = \frac{2e\alpha M_s t_f H_{eff}}{h\eta} \quad 2-7$$

where e is the electron charge, α is Gilbert damping parameter, M_s is the saturation magnetization, t_f is the thickness of the free layer, H_{eff} is the effective uniaxial anisotropy field of the FL, η the spin transfer efficiency and h is Planck's constant.

Compared to toggle magnetic field switch MRAM, it is the current density rather than the absolute current that is important in STT scheme. Thus, both CMOS and MTJ scales down with the junction size. In addition, STT-MRAMs have a much simpler architecture without the digit lines and claddings that are utilized in conventional MRAMs.

To realize the STT writing in memory cells with high scalability and reliability, it is imperative to minimize the write current density to $\sim 5 \times 10^5$ A/cm² in order to scale with the CMOS technology [36]. For a one transistor-one MTJ (1T-1MTJ) architecture, a large write current prevents the transistor from scaling down with the MTJ because the maximum current delivered by a transistor is proportional to its size (typically aMOSFET can supply a current of 100 μ A per 100nm gate width). Consequently, recent researches on MRAM are focused toward reducing the critical switching current. Materials with perpendicular magnetic anisotropy (PMA) demonstrate advantages over in-plane materials. The effective uniaxial anisotropy of in-plane and PMA materials H_{eff} is expressed as follows:

$$H_{eff} = H_{K\perp} - 4\pi M_S \text{ (PMA materials)} \quad 2-8$$

$$H_{eff} = H_{K\parallel} + 2\pi M_S \text{ (in-plane materials)} \quad 2-9$$

where $H_{K\perp}$ and $H_{K\parallel}$ are the uniaxial anisotropy field of perpendicular and in-plane materials respectively. The second term is a demagnetization field that originates from the shape anisotropy contribution[34,35]. The H_{eff} of the in-plane material has to overcome an additional demagnetization field which leads to higher switching current. In addition, the perpendicular materials typically have high uniaxial anisotropy and do not required elongated shape for the memory bit. Thus, a circular bit can be utilized to simplify the fabrication process. In fact, a 20 nm STT-MTJ with perpendicular magnetic anisotropy was recently achieved[37]. The main challenges of making PMTJ work for STT-RAM are to integrate these materials with the MgO tunnel barrier, maintaining the high TMR ratio and spin transfer efficiency, in order to reduce the critical switching currents.

2.2 Perpendicular material candidates for irradiation study

We have identified several PMA material systems which differ on structural basis and magnetic anisotropy origins namely crystalline $L1_0$ MnAl , amorphous rare earth-iron-cobalt (RE-Fe-Co), and interfacial anisotropy CoFeB/MgO and Co/Pd multilayer. These material systems offer a wide range of magnetic properties and microstructures for comparison.

2.2.1 Crystalline $L1_0$ MnAl

The ferromagnetic τ phase of the MnAl binary alloy was first discovered by Kono in 1958[38] . The τ phase of MnAl with 50 a.t. % Mn content is a metastable phase. It possesses excellent hard magnetic properties even without traditional ferromagnetic elements like Co, Fe and Ni. The ferromagnetic τ -MnAl has remarkable magnetic properties such as a high magnetic anisotropy energy (K_U) about 10^7 ergs/cm³ and a saturation magnetization around 490 emu/cm³[39], which are desirable factors for improving the properties of the spin torque transfer (STT) switching behavior of magnetic tunnel junctions (MTJs) for next generation STT-RAM applications.

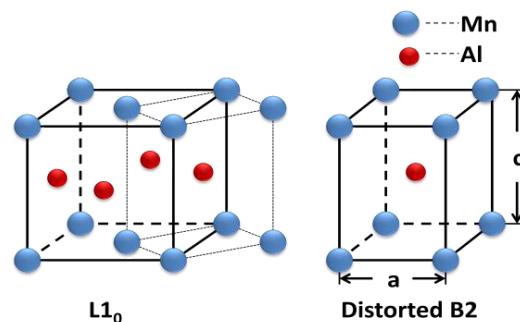


Figure 2.7 Reduced $L1_0$ structure to distorted B2 structure (Courtesy to Yishen Cui)

Ferromagnetic τ -MnAl has an $L1_0$ structure can be reduced to a tetragonally distorted B2 ordered structure with a lattice parameter $c \sim 3.57 \text{ \AA}$ [39,40] as shown in **Figure 2.7**. Within the B2 unit cell, Mn atoms are located at the corner sites while Al atoms occupy the center sites. Thus the whole crystal is equivalent to alternating Al and Mn planes along the tetragonal c -axis. The ferromagnetism originates from the distorted distance between neighboring Mn atom pairs with a value of 2.79 \AA . This value is larger than the interatomic distance of 2.57 \AA in bulk Mn. As a result the exchange coupling between spins of adjacent Mn atoms transitions from antiferromagnetic to ferromagnetic coupling based on the Bethe-Slater curve[38].

The chemical ordering in this system can be parameterized by the ordering parameter, S ($0 \leq S \leq 1$).[41] A high value of the S parameter is required for PMA in τ -phase MnAl.[42]. Various thin film deposition techniques were utilized for the synthesis of ferromagnetic τ -MnAl, including magnetron sputtering[39,43], molecular beam epitaxy (MBE)[41] and pulsed laser deposition (PLD)[44], but the PMA behavior of τ -MnAl was only obtained by MBE and the proper choice of substrate template, while most films made by sputtering were polycrystalline and lacked the right orientation.

2.2.2 Amorphous TbFeCo

Amorphous Rare earth-Transition alloys (RE-TM) were studied in extensively for various memory industries because of their high uniaxial perpendicular magnetic anisotropy[45-48]. The RE elements include Tb, Gd, and Dy and TM elements are Co and Fe. The origin of the perpendicular anisotropy remains elusive. Studies have correlated the magnetic anisotropy of RE-TM magnetic films with various structural characteristics ranging from columnar textures[49] to microcrystallinity [50] to local

magnetic or/and local structural/bonding anisotropy[51-53]. Harris *et al.*[53] showed that PMA energy in amorphous TbFe films increased exponentially with pair-order anisotropy, i.e. the difference in the number of Fe-Fe pairs between the in-plane and out-of-plane directions. Besides the composition investigation, studies on different seed and cap layers of these materials have been carried out[54-56]. Some results indicated that a thick Ta seed layer affects the PMA behavior because of the surface roughness that affects the magnetic pinning sites and the oxidation of the films[57].

RE-TM exhibits ferrimagnetic ordering, consisting of two collinear magnetic sublattices (A and B in **Figure 2.8a**). The term "sublattice" has no crystallographic meaning, but only refers to the spin configuration for RE and TM elements respectively. In each sublattice, the magnetic moments are coupled ferromagnetically, but are antiferromagnetically coupled with the other sublattice. Typically, the temperature dependencies of magnetization for each sublattice are different. It resulted in a complicated temperature dependence of the total magnetic moment of ferrimagnetic materials, and often a compensation temperature (T_{comp}) can be obtained as shown in **Figure 2.8b**). At T_{comp} , the two sublattice magnetizations are equal; therefore, the total magnetization is zero. The occurrence of two critical temperatures, compensation temperature and Curie temperature, are common in ferrimagnetic materials.

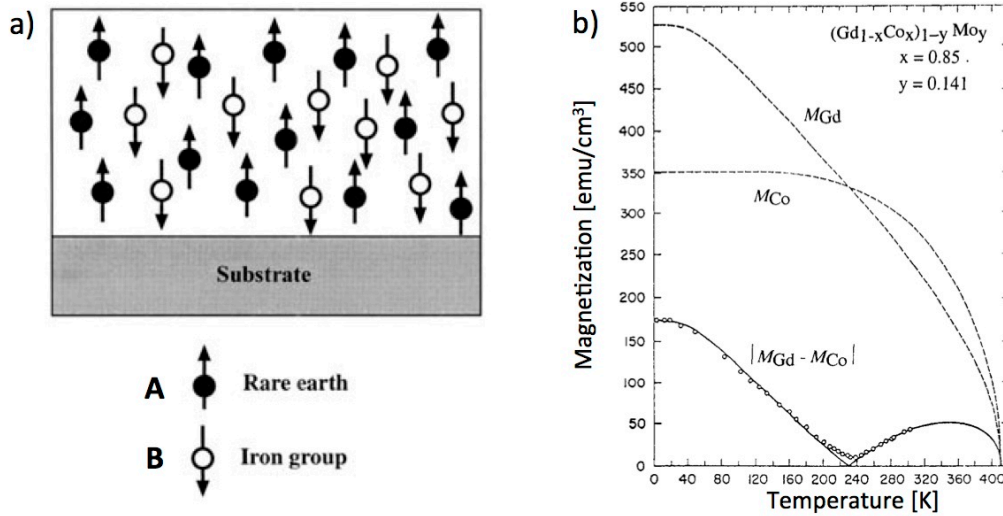


Figure 2.8 (a) Schematic of ferrimagnetism, rare-earth and iron group couple antiferromagnetically (adapted from ref [58]) (b) temperature dependence of sublattices' magnetization. The moment of ferrimagnetic materials is the net moment of each sublattice. Two critical temperatures occurred where the magnetic moment disappear including compensation temperature (T_{Comp}) and Curie temperature (T_C) (adapt from ref [59])

TM ions have a small magnetic anisotropy and RE ions have large anisotropy. The large TM-TM ferromagnetic interaction essentially align the TM moments, while the large RE anisotropy fan the RE moments out over the opposite hemisphere [51]. This results a low magnetization for the alloy, as observed. This model of an amorphous ferrimagnet is validated in amorphous $DyCo_3$ and other amorphous RE-TM alloys that contain non s state RE ions. With the magnetic properties dependent upon the contribution of each sublattice, amorphous RE-TM provide a very attractive feature for materials development in that the magnetization can easily be tuned by composition.

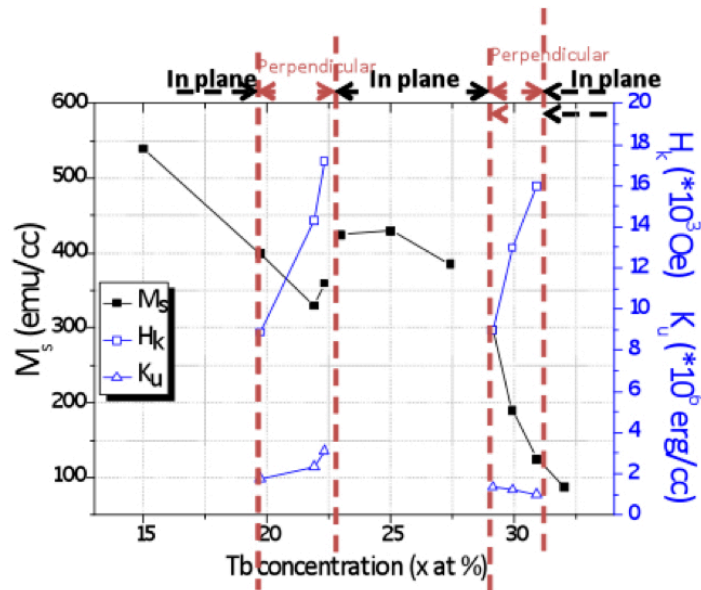


Figure 2.9 Composition dependence of magnetic properties of TbFeCo with Tb content from 15 - 35 at. %

Figure 2.9 shows magnetic properties vs. Tb content for TbFeCo. Very low M_s can be obtained, which is desirable for low power spintronic devices. In addition, the uniaxial magnetic anisotropy can be either in-plane or perpendicular depending on Tb composition. TbCoFe films with high Tb contents (~ 30 at. %) show a strong PMA with a high coercive field, which lead to high thermal stability, making the materials suitable for device application.

Besides the tunable magnetic properties by varying composition, thanks to high magnetostriction, ones can further utilize mechanical stress/strain to modify PMA behavior. Several articles show the effects of stress and strain that modify the PMA behavior of amorphous RE-TM system [60-62]. The induced uniaxial magnetic anisotropy ΔK_U is expressed as

$$\Delta K_U = 3\sigma\lambda_s/2 \quad 2-10$$

where λ_s and σ are magnetostriction and mechanical stress of the film respectively. The

contribution of the sublattices governing the overall the magnetic behavior, the intrinsic magnetostriction can be tuned by doping with negative magnetostriction element such as Sm.

Recently, RE-TM alloys have been investigated for applications in perpendicular magnetic random access memory (p-MRAM). It has been reported that amorphous TbFeCo was used to form perpendicular magnetic tunnel junctions (p-MTJ) for p-MRAM application[46,47]. MTJs based on TbFeCo free and pinned layer have shown excellent spin transfer switching[46]. Even though the large coercivity and high damping seem to limit the application of TbFeCo in STT-RAM, the tunable magnetic properties of RE-TM alloys still show comparative advantages over crystalline materials which usually limit by the epitaxial growth conditions that are vulnerable to disorder-induced defects.

The magneto-transport behavior in RE-TM alloy particularly TbFeCo has not yet been systematically explored up to date. Therefore, radiation damages studies of disorder in RE-TM system is compelling in the sense that it allows one to learn about the effects of defects that are introduced to the system. The further exploration of the modification of the magnetic properties by radiation could be scrutinized systematically by employing control parameters such as radiation doses, radiation beam angles, alloy compositions, etc.

2.2.3 Interfacial anisotropy of multilayer structures

Since the discovery of perpendicular magnetic anisotropy (PMA) in magnetic multilayers[63], this phenomenon has been a subject of interest regarding its microscopic origin. Strong PMA appears for only a limited combination of magnetic and nonmagnetic metals and along particular crystalline orientations, such as Co/Pd(111) and Co/Pt(111)

[63,64]. The role of nonmagnetic metals and the band structure appears to be important factors for such magnetic anisotropy. First-principles calculations predicted a Co monolayer possesses in-plane magnetic anisotropy, whereas they predicted PMA in Fe and V monolayers and some multilayers[65,66]. Previous experiments have been reported that the interfacial hybridization between magnetic and nonmagnetic metals induce PMA in ultrathin Co films[67,68]. The orbital moment (m_{orb}) that contributed to magnetism in $3d$ transition metals was expected to play an important role in PMA since it was believed that magnetic anisotropy often originated from the spin-orbit (SO) coupling. A tight-binding calculation reveals a close connection between magnetic anisotropy and orbital moment [69].

X-ray magnetic circular dichroism (XMCD), which allowed an element-specific and separate determination of the orbital and spin moment in multicomponent systems, was used to study multilayer systems. It was found that the orbital moment of Co and Fe was strongly enhanced in Co/Pd, Co/Pt, and Fe/Pt multilayers[66,70]. From these results, the origin of PMA in alternating magnetic and nonmagnetic ML points to the $3d$ - $5d$ hybridization. A later study reveals the hybridization as well as enhanced orbital moment strongly localize near the Co/Pt interface[71]. Due to the lack of thermal stability and compatibility with MgO barriers, these interfacial PMA materials are not suitable for the free layer/reference layer of MTJs. However, the application of a ML structure can be used toward the MTJ application as a synthetic antiferromagnetic layer (SAF).

Based on the hybridization guideline, metal/oxide interfaces are also explored. Earlier experimental studies also indicate the presence of PMA at the interface in Pt/Co/MO_x (M = Al, Mg, Ta and Ru) trilayer structures[72,73] and in

MgO/CoFeB/Pt[74] . These structures contain a Pt layer in direct contact with ferromagnetic transition metals to stabilize the perpendicular anisotropy. The interfacial magnetic anisotropy between oxide and ferromagnetic metal (Fe/MgO) has been explained by first-principles calculation and attributed to hybridization of Fe $3d$ and O $2p$ orbitals[75]. The breakthrough of material choice with MgO barrier came in 2010 when Ikeda et al[76] demonstrated perpendicular CoFeB-MgO MTJ with high TMR $\sim 120\%$ and high thermal stability as device size reduced to ~ 40 nm. A cross over from in-plane to out-of-plane of CoFeB thickness is typically ~ 1.5 nm.

The radiation effects study of multilayer materials is particularly appealing and necessary in some aspects. The displacement damage could rearrange chemical elements via intermixing or interface roughness, which directly effects the hybridization.

2.3 Radiation damages in magnetic materials and structures

2.3.1 Radiation damages

“Radiation damage” refers to detrimental consequences of radiation in matter. In order to understand the effects of radiation, one needs to be familiar with radiations and their interaction mechanisms.

General types of radiation effects can be categorized as follows:

(i) **Atomic displacement:** Displacement of atoms occurs through kinetic energy transfer from the energetic particles when entering the materials, by the conversion of radiation-induced excitation into atom motion (i.e., recoil). As a charged particle passes through matter, the particle energy dissipates by exciting orbital electrons and by elastic collisions with the material nuclei. An elastic collision can eject an atom from its normal lattice position. The ejected atom is known as a primary knock-on atom (PKA), which

might cause a cascade of atomic displacements before eventually coming to stop. The displaced atom becomes an *interstitial*, and the position the atom formerly occupied becomes a *vacancy*. Together the interstitial and vacancy are referred to as a *Frenkel's pair*. Some displaced atoms can lead to secondary displacements. For relatively small particle fluences (Φ) the induced defect concentration, c , can be written as[77]

$$c = \Phi A(NIEL) \quad 2-11$$

where *NIEL* is the nonionizing energy loss (the density-normalized rate at which an incident particle loses energy to displacements)[78], and the parameter A depends in part on the fraction of atoms that do not recombine immediately following irradiation. The units of c are typically “displacements per target-material atom,” or *dpa*. Because the value of A is generally unknown, one frequently defines the displacement damage dose D as $D = \Phi \cdot NIEL$ and uses it as a parameter known to be directly proportional to c .

(ii) **Ionization:** The process of removing or adding an electron to a neutral atom, thereby creating an ion. A closely related process is excitation, in which the energy level of an electron is raised; however, excitation occurs at an energy less than that required for ionization. The charged particles such as protons, electrons directly ionize materials via Coulomb interaction while neutral charges such as a neutron, energetic photon (i.e. x-ray, gamma ray) indirectly ionize matter via the photoelectric effect, Compton scattering as well as pair production depend on photon energy[79]. The resulting ionization damages may introduce localized electric fields, shift threshold voltages, and increases noise in electronic devices.

(iii) **Impurity production:** In this context, impurity production refers to radiation-induced impurities. One might consider that these radiations can indirectly

cause impurity production through breaking chemical bonds. Charged particles such as protons or alpha particles will eventually slow down and capture the necessary electrons to render them neutral. More important to impurity production are the aftereffects. The protons will become hydrogen and alpha particles will become helium. In both cases, the neutral atoms are gaseous at room temperature, so they exert pressure on neighboring atoms causing swelling or even crack materials.

(iv) **Energy releases/deposition:** All radiations cause energy (and charge) deposition within the absorbing material through the ionization process. In metals, almost all of the absorbed energy from ionization appears as heat, which is generally a manifestation of the kinetic energy deposition. The corresponding temperature rise can change material properties. In the simple form, energy deposition rate per unit volume is the product of absorbed dose rate and material density.

Table 2.1 Radiation damages on materials (adapted from ref [80])

Radiation Source	Charge	Displacement damage	Ionization damage	Impurity production	Energy Release
Protons	Positive	Yes	Yes,direct	H build up	Yes, short range
Alpha	Negative	Yes	Yes,direct	He build up	Yes, very short range
x-ray, γ -ray	Neutral	Rare (via Compton effect)	Yes,indirect	N/A	Yes (gamma heating over large range)
Heavy ions	Neutral	Yes	Small (kinetic	Become	Very small

(Neon, Ar)			energy goes to NIEL)	impurities by themselves	& very short range
------------	--	--	-------------------------	-----------------------------	-----------------------

2.3.2 Effects of radiation on magnetic materials

Early experiments on amorphous, crystalline, MTJ materials have revealed effects ranging from defect formation, structural disorder, structural relaxation, crystallization, and phase separation. The effects on magnetic properties apparently are found to depend on the type of radiation, particle energy and fluence, alloy composition and structure, and degree of inherent structural order and disorder, as well as material system size.

Crystalline materials: In crystalline system, the magnetic properties usually depend on the structure of materials with the easy-axis direction governed by magnetocrystalline anisotropy. Most of the studies then focus on the effect on magnetic properties related to structural deformation caused by the irradiation. The responses of materials to high-energy particles and gamma irradiations were varied depending on many factors, but mostly the structural stability during the irradiation. For example, amorphization resistance and radiation tolerance to the neutron and heavy-ion irradiation was found in complex oxides that have the tendency to accommodate lattice disorder, e.g. oxides with structures related to the fluorite crystal structure[81].

In some cases, high-energy heavy-ion irradiation can result in lattice expansion as well as diffusion-enhanced phase separation. For example, a change in the Curie temperatures has been observed in Fe–Ni, Fe–Pd and Fe–Pt invar alloys irradiated by 200 MeV Xe-ions to a fluence of 10^{14} ions/cm². It was attributed to the lattice expansion and the compositional change due to phase separation[82,83]

The Curie temperature could act as a key factor in determining the material's resistance to radiation, regardless of the source. For examples, SmCo-based magnets ($T_C \sim 750-900\text{ }^\circ\text{C}$) do not show any noticeable changes in magnetic properties while Nd-Fe-B based magnet samples ($T_C \sim 300\text{ }^\circ\text{C}$) lost almost 100% of its magnetic flux with a neutron fluence $\sim 10^{16}\text{ /cm}^2$ [84]. The induced-heat related irradiation in some cases could beneficially affect the magnetic properties. It has been reported that the thermal spike from He ion irradiation improved the crystallization and the magnetic properties of partially ordered FePt[85].

Amorphous materials: The magnetic properties of amorphous magnets do not depend on the atomic structure, but rather on short range orderings or local magnetic environments. A neutron irradiation study on an Fe-B amorphous ribbon showed that the irradiation leads to a decrease of the exchange constant (A_{ex}), implying atomic rearrangement[86]. Deterioration of the soft magnetic properties due to neutron irradiation occurs predominantly in the higher fluence range ($10^{18}-10^{19}$ neutrons/cm²). Opposing effects on the magnetic permeability of magnetic metglass and Mumetal occur at different stages. Irradiation with protons and electrons enhanced the Curie temperature for as-quenched Fe-Ni-P-B melt spun ribbon by introducing the structural relaxation via the transient localized heating [87]. Though in some cases, the structural deformation can indirectly change intrinsic magnetic properties via the modification of internal stress. For a proton irradiation study on an Fe-B-Si-C amorphous alloy, it was found that the magnetic susceptibility decreased with proton doses, while the relaxation frequency increased. The Frenkel defects were responsible for inducing internal stress that modified the relaxation frequency and susceptibility of this material[88]. Point defects can also serve as pinning

sites during magnetization reversal. For example, in magnetic steel[89] and metglass[90], the coercive fields increased after neutron irradiation at 10^{16} n/cm². Defect clusters produced in the collision cascades in the heat spike regime acted as the added pinning sites for the magnetic domain walls. A recent study of heavy ion irradiation on amorphous Ge reveals ions showing core-shell structures with different densities [91]. The ion tracks could be applied to investigate the origins of uniaxial magnetic anisotropy in amorphous materials by which short-range ordering is difficult to examine.

2.3.3 Effects of radiation on magnetic tunnel junctions

Earlier studies of radiation effects on magnetic MTJ devices focus on Al-O based junction. TMR, the critical performance factor of the MTJ, was used as the performance metric for evaluating the “Radiation Hardness”. The change of TMR in post-irradiation MTJs usually associated with displacement damages that varied greatly with radiation species/energy/dosage.

Moodera *et al.*[92] used Si and Ag ions to irradiate undoped Al-O and Ge-doped MTJ. After irradiation, the TMR of the undoped junctions showed a relatively small change (from ~20 % to ~18%), while doped junction showed a very large change, from ~18 % to ~ 0.3 %. After the 200 MeV Ag ion irradiation with fluence of 1×10^{11} ions/cm², the TMRs became negligible. SRIM simulation showed severe displacement damages in the junction and Co layer caused by 200 MeV Ag ions.

Sacher *et al.* investigated the effect of different ion species with much lower energy on Al-O barrier in MTJs[93]. He⁺ and Ar⁺ (with energies ranging from 15 to 105 eV) irradiation took place *in situ* after oxidation of the 1.4-nm-thick Al layer. For both ion species, the area resistance (R_A) of the junctions increases significantly with ion

energy, whereas the TMR is reduced. There was a discrepancy in the TMR as a function of the ion energy for He^+ and Ar^+ . The different ions penetration depths that vary in accordance with the different masses of the ions, different energy loss per unit depth, and different ion fluence were thought to be responsible for such discrepancy.

Recently irradiation effects on the spin torque transfer (STT) magnetic tunnel junctions, where MgO is used for the tunnel barrier layer and amorphous CoFeB is used as a reference and a free layer, have been examined in very recent years[94-96]. In 2012, H. Hughes *et al.*[95] investigated the performance of in plane MTJ devices with ~ 1 nm MgO barrier irradiated by 2-MeV and 200-MeV protons with fluences up to 1×10^{12} H^+/cm^2 . The switching behaviors and state retention of these STT-MTJs were identical before and after proton irradiation. Hughes also studied total ionizing dose (TID) effect by γ -rays irradiation up to 1Mrad, and did not observe any change in TMR, RA values as well as the spin torque switching behaviors. Later, Ren *et al.*[96] found similar results showing no significant change in TMR and coercivity from thermal neutron irradiation of fluence 2.9×10^{15} n/cm^2 and accumulated γ rays up to 10 Mrad. The influence of heavy ion irradiation on perpendicular CoFeB-MgO MTJ has been reported most recently by Kobayashi *et al.*[94]. It has been observed that the tested structure remains in the pre-set high resistance state with a very small degradation in resistance ($\sim 1\%$) after the 15-MeV Si ion irradiation.

CHAPTER 3. Experiments

This chapter describes the main techniques used for materials characterization before and after irradiation. High-resolution x-ray diffraction (HRXRD) is the main technique to study the crystal structure to determine the chemical ordering of $L1_0$ MnAl as well as to indicate whether or not crystallization exists in amorphous materials. The thickness of the film is determined by x-ray reflectivity (XRR). The fast Fourier transform (FFT) and x-ray diffuse scattering (XDS) techniques are employed to characterize interfaces in multilayer structures. Atomic Force Microscopy (AFM) and Magnetic Force Microscopy (MFM) are utilized for determining surface morphology and magnetic domain imaging respectively. The Vibrating Sample Magnetometry (VSM) and Magneto-Optic Kerr effect (MOKE) are used for magnetic properties characterization. Hall bars were fabricated via photolithography techniques to study the transport properties of thin films while pulse-switching measurements was used to characterize transport properties of STT-MTJ.

3.1 Structural characterizations

3.1.1 X-ray diffraction (XRD)

X-ray diffraction (XRD) is used to characterize the crystal structure and the phase of materials because the wavelength of the x-ray is comparable to the atomic spacing in crystals. Cu $K\alpha$ radiation used in XRD has a wavelength of $\sim 1.54 \text{ \AA}$. A Ge monochromator is used for high resolution XRD. The structure characterizations of this work are performed by a Rigaku Smart lab.

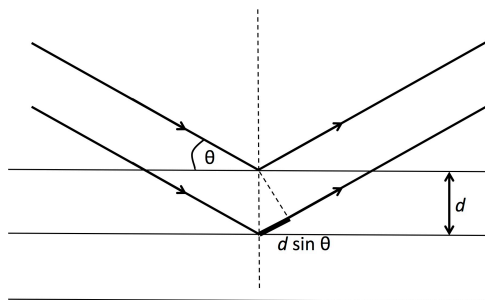


Figure 3.1 Schematic of basic XRD geometry on material with lattice spacing d

According to Bragg's law [97], one can determine crystal structure and lattice parameters from the positions of diffraction peaks. The law that describes the constructive interference pattern is

$$2d \sin \theta = n\lambda \quad 3-1$$

where n is an integer number describing the order of the reflection, λ is the wavelength of the x-ray (1.54 Å), d is the atomic spacing between the lattice planes, and θ is the Bragg angle at which a maximum diffraction intensity occurs. **Figure 3.2** shows a schematic of the basic XRD geometry.

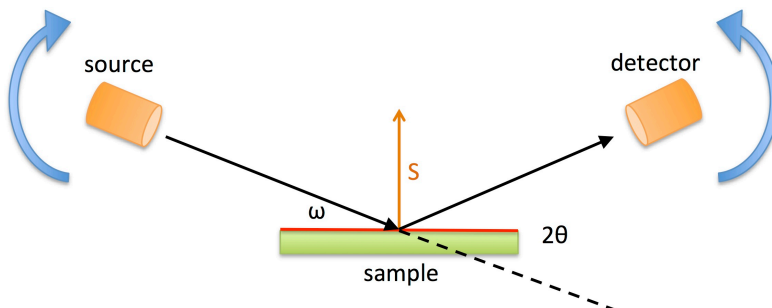


Figure 3.2 Schematic of $2\theta/\omega$ scan in Rigaku SmartLab XRD tool (adapted from ref[98])

$2\theta/\omega$ scan is typically used to determine the positions of Bragg peaks. For a $2\theta/\omega$ scan, the source moves with respect to the sample at an angle ω and the detector moves simultaneously by an angle 2θ , as shown in **Figure 3.2**. The $2\theta/\omega$ scan is used to determine the phase composition in thin film samples and the lattice spacing can be extracted from the 2θ value via Bragg's law. In addition, one can also determine the chemical ordering based on the diffraction patterns, which is important for ordering alloys such as MnAl.

The structure factor F_K describes how the interference of the waves scattered from identical ions affects the intensity of the Bragg peaks in X-ray diffraction[99]. According to the lattice symmetry, F_K associated with certain reciprocal lattice vectors K could be canceled out and the corresponding Bragg diffraction peak is forbidden. By definition, the structure factor F_K for diffraction of the lattice plane (khl) in the case of MnAl lattice which has a B2 structure indicates that both (002) and (001) peaks are allowed. The chemical ordering parameter, S , is defined as[100]

$$S = \frac{(\sqrt{I_{(001)}/I_{(002)}})_{Exp}}{(\sqrt{I_{(001)}/I_{(002)}})_{Cal}} \quad 3-2$$

The numerator is the square root of the peak intensities $I_{(001)}/I_{(002)}$ obtained experimentally, whereas, the denominator is the calculated value of the ideal B2 structure, which can be estimated from[101,102]

$$\left(\frac{I_{001}}{I_{002}}\right)_{Cal} = \frac{F_{(001)}^2(LPe^{-2M})_{001}}{F_{(002)}^2(LPe^{-2M})_{002}} \quad 3-3$$

where L is the Lorenz factor given by $1/(\cos \theta \sin \theta)$ in epitaxial films, P is the

polarization factor related to the diffraction angle and XRD set-up, and M is the Debye-Waller factor determined by the displacement amplitude and the scattering vector.

3.1.2 X-ray reflectivity (XRR)

The film thickness is characterized by x-ray reflectivity (XRR). X-ray scattering at very small diffraction angles can characterize the electron density profile of a thin film. Through modeling/fitting of the reflectivity pattern, one can obtain information about film thickness, interface roughness, and film density. The fundamental equation that determines multilayer film thicknesses is [103]:

$$r = \sum_{j=0}^N r_{j,j+1}^* e^{(i\beta t_j)} \quad 3-4$$

where $r_{j,j+1}$ are the Fresnel reflectivity coefficients of j and $j+1$ layers interface, β is the vertical component of the transmitted portion of the incident beam, and t_j is the j layer film thickness. This equation could be reduced to a simple form if there is only one layer of the film on a substrate.

Another popular method to analyze the reflectivity pattern is the Fourier transform method, which directly measures the structure factor of the interface pattern[99]. The Fourier method was first applied to x-ray diffraction curves by directly taking the Fourier transform of the experimental curve. Consequently, the Fourier transform yields peaks at the depth values corresponding to every interface of the film layers, due to the abrupt change of electron density at each interface. The period of the oscillation of the interference fringes is related to the film thickness and the amplitude is related to the surface or interface roughness. **Figure 3.3** shows a typical XRR pattern of a ~20 nm indium tin oxide (ITO) film grown on the quartz substrate and the corresponding

FFT pattern. The FFT result suggests that there are two layers with the thicknesses of ~ 4.2 nm and ~ 14.9 nm in the 20 nm ITO films with slightly different densities.

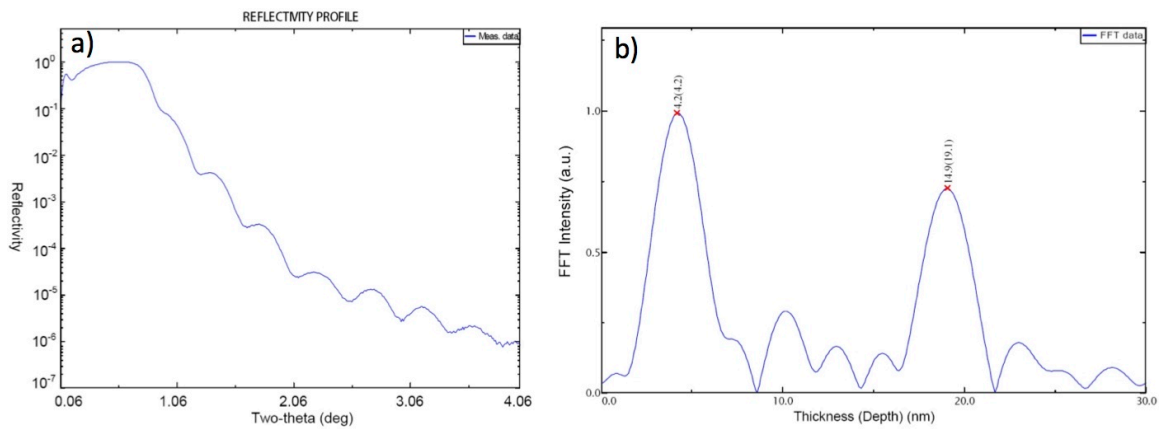


Figure 3.3 (a) XRR profile of ITO film on glass substrate **(b)** FFT of the XRR. The numbers on top of the peaks show the calculated layer thicknesses. The numbers in the parentheses show the depth from the surface

3.1.3 X-ray diffuse scattering

While XRR give the information about the variation in scattering density normal to the film surface, x-ray diffuse scattering (XDS) provides the information about the density and morphology homogeneity along the lateral directions. The advantage of this method is that it reduces bulk scattering from the substrate because of the limited penetration depth of the incoming beam near the critical angle of the substrate ($< 5^\circ$). X-ray diffuse scattering measurement is done by keeping the scattering angle 2θ fixed and varying the angle of incidence ω from 0 to 2θ as shown in **Figure 3.4**.

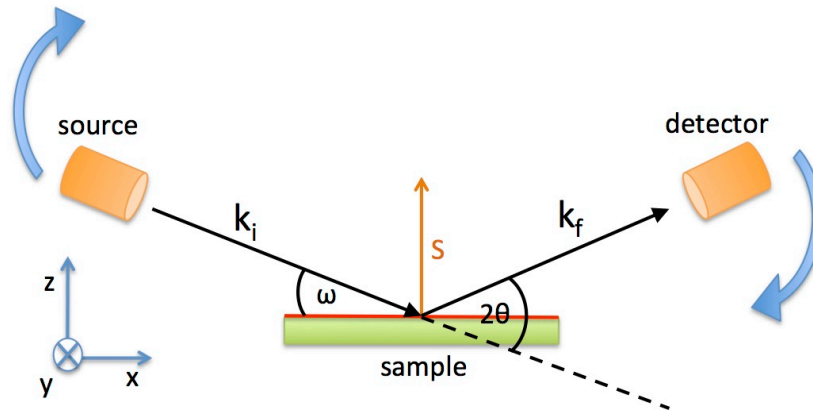


Figure 3.4 Schematic of rocking x-ray diffraction scattering measurement. The 2θ angle is fixed while angle of incidence ω vary from 0 to 2θ .

A monochromatic x-ray beam with the wave vector k_i is directed to a surface with a very small incident angle ω . The Cartesian z-axis is the normal to the surface plane, whereas the x-axis is the direction along the surface parallel to the beam, and the y-axis perpendicular to it. The x-rays are scattered along k_f . The measured scattering normalized wave vector q_x is defined by[104]

$$q_x = \frac{2\pi}{\lambda} [\sin(\omega)/\sin(\theta)] \quad 3-5$$

The result of the rocking curve gives three principal features: the specular reflection, the first and second Yoneda wings. The central peak corresponds to the specular reflection, where the angle between the x-ray beam and the sample's surface (θ_1) is equal to the angle between the detector and the sample's surface (θ_2). While the Yoneda wings appear when θ_1 (first Yoneda wing), and θ_2 (second Yoneda wing) equal the critical angle.

3.2 Atomic force microscopy

3.2.1 Surface morphology

Atomic Force Microscopy (AFM) is used to characterize the surface roughness of all thin films. AC air mode (tapping mode) is used for the surface morphology in a scanning probe microscope (Asylum Research Cypher). A schematic of the basic components of an AFM is shown in **Figure 3.8**. When the cantilever is brought close to the sample surface, forces between the cantilever tip and sample cause the cantilever to bend, and the deflection is detected by an array of position sensitive photodiodes via a laser spot reflected from the top surface of the cantilever. In tapping mode, a piezoelectric actuator forces the cantilever to oscillate near its resonance frequency, hence tapping. As the tip comes close the sample surface (the distance between the cantilever and sample surface can be set via actuator set point voltage), the amplitude of this oscillation decreases due to the forces between the sample and tip. Once the amplitude of this oscillation is adjusted to suit desired scanning parameters, the sample is then ready to be scanned using piezoelectric scanners. The height of the cantilever is adjusted according to the fixed oscillation amplitude throughout the scanning area. As a result, an image of the surface profile is produced from the deflections detected by the photodiode.

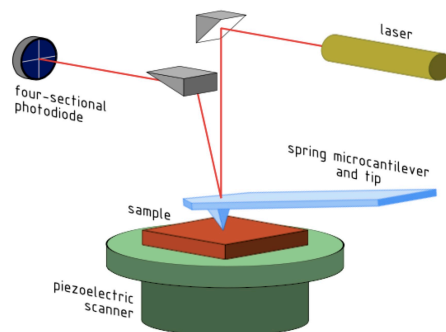


Figure 3.5 Schematic of the basic AFM mechanism (adapted from [Http://Commons.Wikimedia.org/Wiki/File:AFM_Schematic_\(en\).Svg](http://commons.wikimedia.org/wiki/File:AFM_Schematic_(en).Svg) (n.d.).)

3.2.2 Magnetic domain imaging

Magnetic Force Microscopy (MFM) was used to characterize the magnetic domain structure of thin films. The mechanism is similar to AFM except that the cantilever tips are coated with magnetic material, and during the scan, the cantilever is lifted above the surface to sense the magnetic force between the cantilever tip and the sample surface. MFM operates in the nap mode, which collects both surface topography and magnetic information. The surface morphology is collected first by a fast AFM scan in the same way as done in the ac air mode (tapping mode), then the cantilever is elevated to a preferred “delta height” above the surface to perform magnetic imaging over the same area. The “delta height” is adjusted so that the AFM and MFM signal are distinguishable. The benefit of the nap mode is that both surface morphology and magnetic image of the same area are collected and can be analyzed together. This is very useful for correlating magnetic properties to morphological structures. Before starting a scan in the nap mode, it is recommended to test the magnetic tip using regular ac air mode to prevent any fault engage caused by a defective tip.

3.3 Magnetic property characterization

3.3.1 Vibrating Sample Magnetometer (VSM)

Magnetic property measurements include magnetic moment as a function of applied magnetic field (M vs. H) for a fixed temperature, and magnetic saturation as a function of temperature (M_s vs. T). Magnetic anisotropy is calculated based on the in-plane and out-of-plane magnetic hysteresis loops. The details are discussed in later

chapters. The magnetic measurements are performed using the VSM option in a Physical Properties Measurement System (PPMS) model 6000 (Quantum Design) and Versalab (Quantum Design). Both systems are equipped with a superconducting magnet providing a maximum magnetic field up to 7 Telsa for PPMS and 3 Tesla for Versalab. The temperature dependent measurement can be performed from below 2 K in the PPMS and 50 K in the Versalab up to 400 K. The sample is mounted to a quartz rod sample holder that is fastened to the sample rod. The sample is placed into the center cavity of the pick-up coil probe. Sample centering is done with an automated sequence through the Multiview software prior to measurement. In this system a linear motor drive head is used to oscillate the sample. During the measurement, the sample is vibrated sinusoidally in the magnetizing field to induce a voltage in the pick up coil that is proportional to the sample's magnetic moment. By detecting this induced voltage, magnetic moment of the sample can be determined.

The total magnetic moment (m_{total}) measured on magnetometers can be written as $m_{\text{tot}} = m + m_{\text{sub}} + m_{\text{holder}}$ where m is the magnetic moment of the thin film, m_{sub} is the magnetic moment of the Si substrate, and m_{holder} is the magnetic moment of the sample holder. In order to deduce the magnetic moment of thin film, the background contributions from sample holder and from Si substrate must be subtracted. Firstly, the total magnetic moment m_{total} is measured. Then the sample is taken off and the sample holder is installed again into the magnetometer to measure m_{holder} under the same condition. The substrate moment can be calculated. The sample is weighed to find the mass D of substrate (the mass of film is very small in comparison with the mass of substrate and can be neglected, so the mass of the sample can be considered as the mass

of substrate). In case of Si substrate, the density at room temperature is $D_0 = 2.336$ g/cm³. The induced magnetic moment of Si substrate m_{sub} can be calculated by $m_{\text{sub}} = \chi_{\text{Si}} \mu_0 H \cdot D / D_0$ where H is the applied field, μ_0 is the permeability of vacuum, and $\chi_{\text{Si}} = -1.4 \times 10^{-7}$ is the magnetic susceptibility of Si.

3.3.2 Magneto optical Kerr effect

The magneto-optic Kerr effect (MOKE) is a useful tool to characterize the magnetic anisotropy of ultrathin and multilayer films. The MOKE relies on the change of the polarization direction of light when reflected by a magnetic material. Consequently, linearly polarized light experiences a rotation of the polarization plane can be shown as complex Kerr angle ϕ_K that can be expressed by Kerr ellipticity, ϵ_K , which is a phase difference between electric field components of incident light. Because of the different magnetization directions relative to the plane of the incident light there are three different configurations for MOKE as depicted in **Figure 3.6**[105].

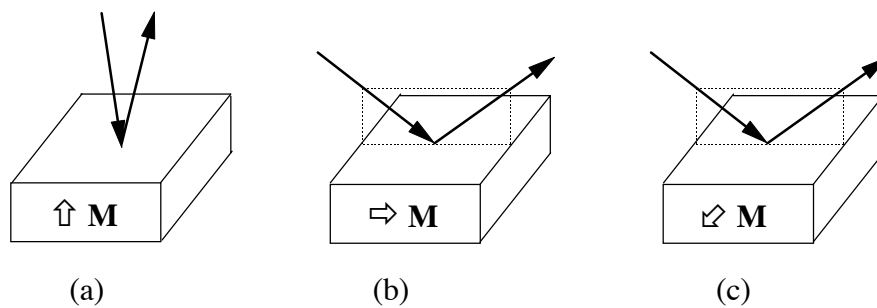


Figure 3.6 Schematic of 3 basics configurations of Kerr effect: (a) polar Kerr; (b) longitudinal Kerr; (c) transverse Kerr (adapted from ref[105])

In Polar Kerr effect configuration, the magnetization \mathbf{M} lies perpendicular to the sample surfaces. For longitudinal Kerr effect, \mathbf{M} lies parallel to the sample surfaces and in the plane of incidence. For Transverse configuration, \mathbf{M} lies parallel to the sample surfaces and perpendicular to the plane of incidence.

In Polar Kerr configuration, the polarization has turned by an angle typically less than a degree. Reversing the magnetization leads to the opposite rotation. It occurs only if the magnetization is forced to be perpendicular to the surface, under the effect either of a sufficiently strong applied field, or of a perpendicular anisotropy material. For symmetry reason, the rotation does not depend on the in-plane component of magnetization. Thus the polar Kerr effect is suitable for studying perpendicular magnetic anisotropy materials. The polar MOKE was used in this thesis in conjunction with VSM to accurately acquire magnetic moment and perpendicular anisotropy.

3.4 Transport Characterization

3.4.1 Hall bar device fabrication

The transport characterizations are performed on thin film devices that are fabricated into a Hall bar structure. These Hall bar devices are fabricated via standard 2-step photolithography including Hall bar patterning followed by electrode contact deposition. The first step is patterning the etch mask and etching either a wet etch using diluted hydrochloric acid or a dry etch using a reactive ion etching (RIE) and inductively coupled plasma (ICP) techniques. Upon the completion of Hall bar patterning, the similar photolithography is employed for the contact patterning. This process requires accurate alignment to eliminate a shorted circuit. Once the contacted mask is prepared, the sample is transferred to the electron beam evaporator for Ohmic contact deposition. A thin layer

of Ti (~5 nm) followed by a thick layer of Au (100 – 200 nm) deposition is typical for the top contacts in this thesis. After electrode deposition, the contact mask is removed by submerging the sample in acetone for a lift-off process. The detailed step-by-step procedure for Hall bar patterning can be found in the reference[98].

3.4.2 Resistivity measurement

The electrical resistivity measurement is done by both Versalab system and PPMS system. The Hall bar sample is wire-bonded from the resistivity puck to the contacts of the device as shown in **Figure 3.7b**. After loading the puck in the system, the resistance of Hall bar is measured with the electric the excitation current used ranging between 0.1 to 5 mA depending on the resistance of the material. The excitation current is adjusted to minimize the measurement noise and Joule's heating to the materials. The measurements are made in "AC" mode as the system generates a DC excitation and reads the potential drop across the sample. Next, a DC excitation in the opposite direction is generated and the potential drop is read again. The read-out is an average of the absolute value of the resistance measured by both positive and negative voltages; therefore, the errors from DC offset voltages are eliminated. The DC resistivity or conductivity is then calculated according to the device geometry and the thickness of the film.

3.4.3 Magnetoresistance and Hall measurement

Magneto-transport properties of samples have been investigated by means of magnetoresistance and Hall effect. The measurements are performed in the same way as electrical resistance measurement; however, they also incorporate an external magnetic field (H) applied perpendicular to the Hall bar device.

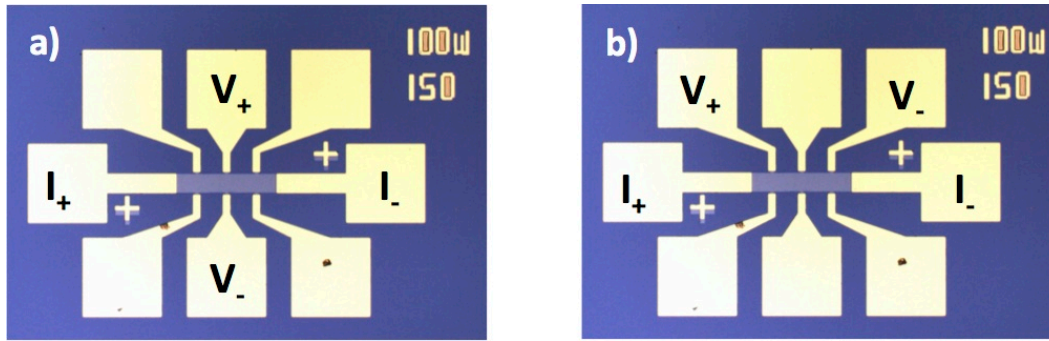


Figure 3.7 A Hall bar device with (a) Hall measurement configuration (b) magnetoresistance configuration

The Hall effect is measured in the direction perpendicular to the current as shown in **Figure 3.7a** in which the Hall resistance can be derived from

$$R_{Hall} = V_{Hall}/I \quad 3-6$$

The Hall effect consists of a sum of two terms[106]. The first term is proportional to the magnetizing field and has been called the ordinary Hall effect (OHE). Its order of magnitude and sensitivity variations in temperature and in composition are comparable with the Hall effect in non-ferromagnetic metals. The second term is proportional to magnetization and has been called the anomalous Hall effect (AHE). The Hall resistivity of a metallic magnet can be expressed as

$$\rho_H = R_0\mu_0H + R_S\mu_0M \quad 3-7$$

where H , M , R_0 and R_S are the applied field, the magnetization of the sample, the ordinary Hall coefficient, and the anomalous Hall coefficients, respectively. In term of magnitude, the anomalous coefficient R_S usually dominates the ordinary coefficient R_0 (proportional to $1/nq$). In case of metallic magnetic compound, which differ from the case of semiconductor, the density of conduction electrons n is very large such that R_0 becomes

negligible.

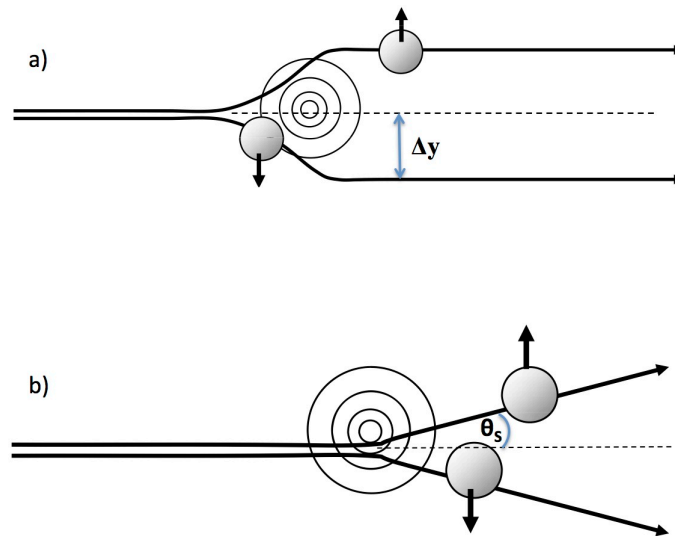


Figure 3.8 Comparison of side jump mechanism **(a)** characterized by displacement Δy of carrier trajectory **(b)** skew scattering characterized by Hall angle θ_s (adapt from ref[107])

Two different types of scattering events have been postulated as the microscopic origins of AHE[106]. The semi-classical AHE theories by Smit and Berger focused on the influence of disorder scattering in imperfect crystals. Smit argued that the main source of the AHE currents are asymmetric (skew) scattering from impurities caused by the spin-orbit interaction [108,109]. Skew scattering is characterized by a constant spontaneous angle θ_s in which the scattered spins are deflected from their original trajectories as shown in **Figure 3.8b**. The skew-scattering contribution to the AHE is simply the contribution in which proportional to the Bloch state transport lifetime. Although in semiclassical Boltzmann transport theory states that the transition probability $W_{n \rightarrow m}$ from n to m is identical to the transition probability in the opposite direction ($W_{m \rightarrow n}$),

with the presence of spin orbit coupling, the asymmetric appears by which a right-handed transition with respect to the magnetization direction has a different transition probability than the corresponding left-handed transition. This asymmetric scattering leads to a current proportional to the longitudinal current driven by electric field and perpendicular to both electric field and magnetization. When this mechanism dominates, both the Hall conductivity and electrical conductivity are proportional to the transport lifetime of the carriers and the skew scattering Hall resistivity and the longitudinal resistivity (ρ_{xx}) can be expressed as[108]

$$\rho_H^{skew} = a\rho_{xx} \quad 3-8$$

Berger argued that the main source of the AHE current was the “side jump” experienced by quasiparticles upon scattering from spin-orbit coupled impurities and results in a constant lateral displacement Δy of the charge’s trajectory at the point of scattering as shown in **Figure 3.8a**. This side-jump contribution to the Hall conductivity is independent of transport lifetime τ and therefore contributes to the AHE in an expansion in powers of scattering rate. The basic semiclassical theory for a side-jump contribution can be stated that when considering the scattering of a Gaussian wave packet from a spherical impurity with SOI [$H_{SO} = (\frac{1}{2m^2c^2})(r^{-1} \partial V/\partial r) S_z L_z$], a wave packet with incident wave vector \mathbf{k} will experience a displacement transverse to \mathbf{k} equal to $\frac{1}{6}k\hbar^2/m^2c^2$. This kind of mechanism cannot be described by traditional Boltzmann transport theory in which only consider the probabilities of transitions between Bloch states and not microscopic details of the scattering processes. The side jump AHE current was viewed as the product of the side jump per scattering event and the scattering

rate[110]. However, one puzzling aspect of this semiclassical approach was that all dependence on the impurity density and strength seemingly dropped out. Therefore, the side-jump mechanism yielded a contribution to the Hall conductivity, which was seemingly independent of the density or strength of scatterers. The predicted correlation between the side jump scattering Hall resistivity and the longitudinal resistivity (ρ_{xx}) is

$$\rho_H^{side\ Jump} = b\rho_{xx}^2 \quad 3-9$$

The AHE is usually attributed to the skew scattering when ρ is small (low temperatures and/or pure metals) and to the side-jump when ρ is large (high temperatures, metallic alloys, and disordered system)[106]. Thus, one can express AHE scaling relationship between the Hall resistivity and its longitudinal counterpart as

$$\rho_H = \sum a_i \rho_{xx}^n = a\rho_{xx} + b\rho_{xx}^2 \quad 3-10$$

where $n = 1$ correspond to skew scattering, $n=2$ for side jump. Though, the intermediate power $n = 1.5$ was also observed in the case of Ni ($n = 1.5$) that both skew scattering and side-jump are present[111]. By plotting ρ_H/ρ_{xx} vs. ρ_{xx} , and fitting the linear relation to the data, one can infer the coefficients a and b .

Magnetoresistance is measured in the wiring configuration as shown **Figure 3.7b** such that the voltage leads become parallel to the current leads. Conducting materials show a resistance change from electron-electron scattering in magnetic fields due to the Lorentz force. This resistance change is very small for metals unless the field is very high. This force is perpendicular to the direction of the motion and therefore causes an elongation of the path an electron takes through a material. This means that the scattering

probability rises with the magnetic field and therefore also the resistance. The resistance is proportional to the square of the magnetic field perpendicular to the plane[112]. The additional contributions to MR could arise from electron scattering of magnetic domain walls during magnetization reversal[113] as well as weak localization from disorder lattices[114].

3.5 Pulse switching measurement

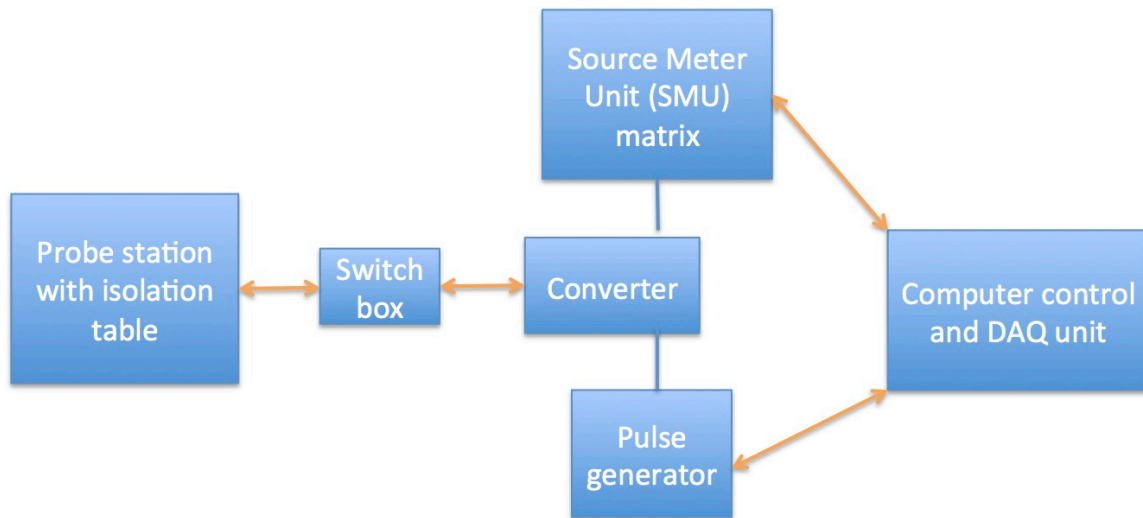


Figure 3.9 Schematic of pulse switching measurement set up

Basic components of the pulse switching measurement are shown in **Figure 3.9**. All units are placed on top of electrostatic mat that is connected to ground. The computer control is connected to source meter unit (SMU) matrix and a pulse generator. Mechanical relay switches, enabling the unit to measure many devices at the same time, control the SMU matrix. Here, the measurement is done on one device at a time. SMU and pulse generator units are then connected to the converter giving two outputs (high and low). The outputs are connected to the probes via switch box that is used additionally to prevent electrostatic discharge from engaging and retracting the probes. The vibration-

isolation table is installed to minimized noises caused by the environment. The system is used to measure two functions of STT-MTJ device, the switching behavior and the state retention test.

For the switching operation the computer control unit sends a voltage pulse (write voltage), set manually, to the device to set the states (high or low current) of the devices. Following the voltage pulse, the SMU applied a small DC bias voltage (read voltage) to read the current and therefore determined the resistance state of the device. The switching of the resistance state is then performed by applying another write voltage pulse with the opposite polarity to complete 1 cycle. The functionality of the devices is performed for 100 cycles. The magnitude of the write and read voltage are optimized to ensure switching, minimize noise and eliminate the read-disturb, which is when the read DC-bias voltage can cause the unintended switching. The state retention test done by measuring 100 repeated reads using only the SMU.

CHAPTER 4. Irradiation of perpendicular magnetic tunnel junctions

4.1 Introduction

Recently the use of perpendicular magnetic tunnel junctions (PMTJ) has been proposed for STT-RAM to reduce the critical current, which improves the performance significantly[115,116]. A magnetic multilayer with perpendicular magnetic anisotropy resulting from the interface is currently used in the PMTJ due to the compatibility with the current processing of STT-RAM.

This chapter focuses on the effects of proton irradiation on microstructure and properties of PMTJ devices. To elucidate the damage mechanisms, the individual magnetic layer stacks as well as the entire PMTJ structure are characterized. The spin torque switching of PMTJ devices was also studied. Critical metrics for the device performance such as TMR, device retention, and switching currents are measured. Additionally preliminary studies using radiation sources, including heavy ions, and x-rays are performed to identify plausible failure mechanisms in MTJ devices associated with the irradiation species.

4.2 PMTJ films stacks

Samples were deposited on 6" silicon wafers by a commercial ultra-high vacuum sputtering system (TIMARIS, Singulus Technologies) at Grandis Inc. A schematic of the PMTJ film stack is illustrated in **Figure 4.1**. The substrate is (100) silicon substrate covered with a ~100 nm thermal SiO₂. Ruthenium is sputter-deposited on the top of the oxide layer followed by tantalum as the seeding layer. The synthetic antiferromagnet (SAF) as the pinning layer is composed of multilayers Co/Pd, Ru spacer, and a second

magnetic layer of CoFeB. The CoFeB and CoPd couple antiferromagnetically through the Ru spacer so that their magnetizations are antiparallel. Each layer is, by design, of equal magnetic moment and the antiparallel arrangement produces zero stray magnetic field and reduce magnetic coupling to the free layer. The combination of Co/Pd multilayers is pinned via exchange-bias to form a magnetic reference layer that is called the “reference layer”. The “free layer” is a ferromagnetic CoFeB layer, which usually possesses lower coercivity than reference layer. The free layer and the reference layer are separated by a MgO tunnel barrier. The capping layers of Ta and Ru are used to prevent oxidation and achieve good conductivity. This perpendicular magnetic tunnel junction relies on an interfacial anisotropy magnetization of Co/Pd superlattice and CoFeB/MgO layers.

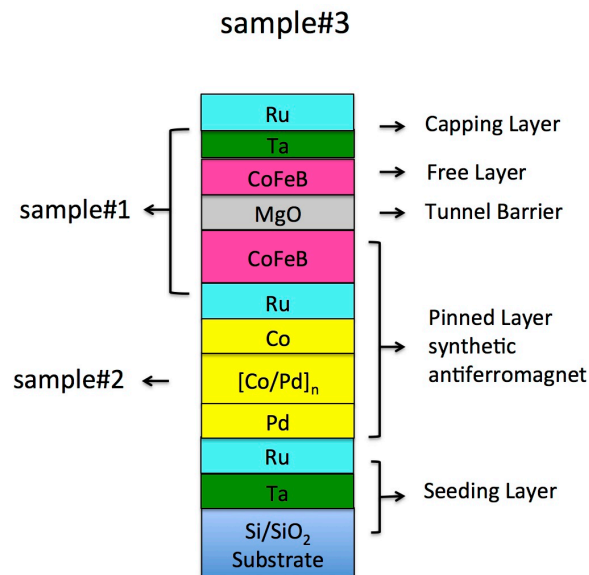


Figure 4.1 Schematic of the complete pMTJ structure. Two ferromagnetic structures consist of CoFeB/MgO (free layer: sample#1) and CoPd superlattice (SAF layer: sample#2) are investigated individually.

Two key magnetic layers of interest are a very thin CoFeB/MgO and a Co/Pd

superlattice. The “half structures” are deposited that only consisted with these two separate magnetic layers in addition to the full structure of PMTJ. A 2 MeV-energy proton is chosen so that particles can traverse the entire sample without a significant loss of energy, thereby creating a uniform profile of defects. An initial fluence (Φ) of 10^{14} H^+/cm^2 is employed to establish a baseline for the radiation response. The final fluence of 5×10^{15} H^+/cm^2 is used to establish the failure threshold for the PMTJ. The irradiation details and samples IDs are listed in **Table 4.1**.

Table 4.1 2MeV-energy Proton irradiation procedure and total fluence (TF)

Sample ID	1 st radiation TF [H^+/cm^2]	2 nd radiation TF [H^+/cm^2]
G1A (CoFeB/MgO)	1×10^{14}	-
G3A (Co/Pd)	1×10^{14}	-
PMTJ#1	1×10^{15}	5×10^{15}
PMTJ#2	1×10^{14}	1×10^{15}
Wafer#1	1×10^{14}	-
Wafer#2	1×10^{15}	-

4.2.1 CoFeB/MgO and Co/Pd superlattice

(i) Morphological and structural characterization

AFM is used to characterize the change in the surface morphology of the half structures before and after the proton irradiation. **Figure 4.2** shows AFM images of samples before and after the irradiation. The unirradiated G1A sample exhibits a smooth surface with a root-mean-square (RMS) roughness of ~ 0.23 nm and that of G3A is ~ 0.32 nm. After the proton irradiation, the surface roughness increases to ~ 3 nm for the G1A

film, and ~ 7 nm for G3A, respectively. AFM images reveal hillocking features with the heights of 18-60 nm that are responsible for the roughening of the surface. Similar features are also observed under the scanning electron microscope (SEM). The hillocking features are likely the result of H^+ implantation in the Si wafer. As the protons penetrate through Si, they become neutral and form hydrogen atoms by capturing electrons in Si substrate. The agglomeration of hydrogen atoms leads to the formation of H_2 gases that exert pressure to the neighboring atoms causing bubbles or swelling of materials as observed by AFM. It has been reported that a thermal treatment can induce the gas bubble to expand, and even causes the crack in materials[117,118]. The application of this technological procedure has been used mainly in the production of silicon-on-insulator (SOI) wafer substrate, which is called “Smart Cut”[119].

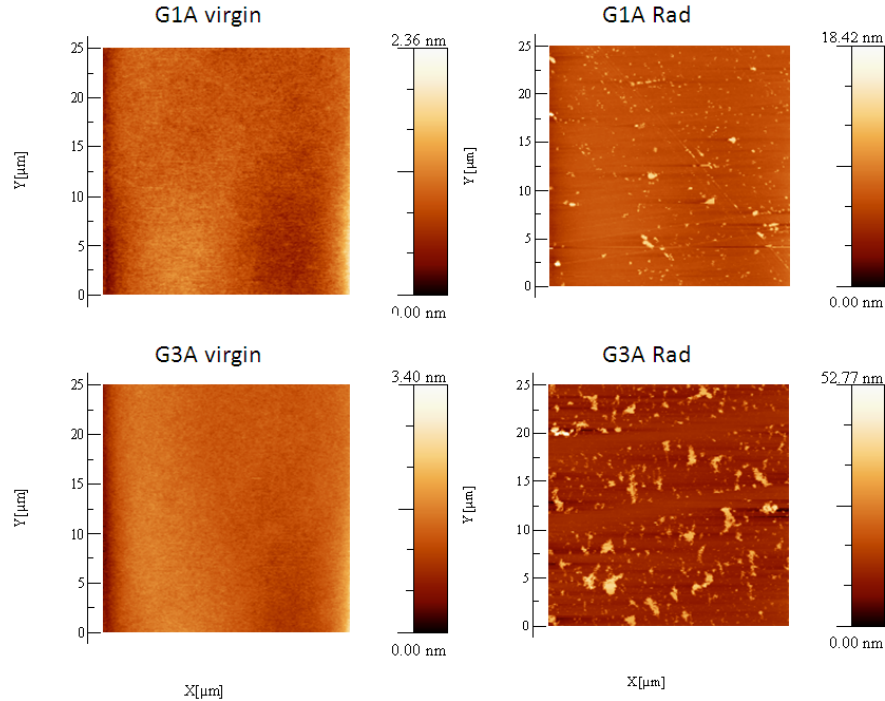


Figure 4.2 AFM images of unirradiated and samples irradiated with $1 \times 10^{14} H^+/cm^2$.
G1A: CoFeB/MgO; G3A: [Co/Pd] superlattice.

XRR results and its corresponding fast Fourier transforms (FFTs) are shown in **Figure 4.3**. The reflectivity profiles of CoFeB/Mgo and Co/Pd are demonstrated in **Figure 4.3a** and **Figure 4.3c**, respectively. One can extract the information on the density and the thickness, as well as the roughness of the surface and the interface from the oscillation of x-ray intensity in XRR profile via data fitting. The intermixing of individual layers can be quantified by the changes in the thickness, the density, and the roughness of each layer. The Fast Fourier Transform (FFT) of the x-ray reflectivity spectrum translates such oscillations into peaks that represent the positions/depths of buried interfaces. Both CoFeB/MgO and Co/Pd sample exhibit similar microstructures, but the x-ray intensity decreases after proton irradiation. The lower intensity is the direct result of the increasing surface roughness of the films.

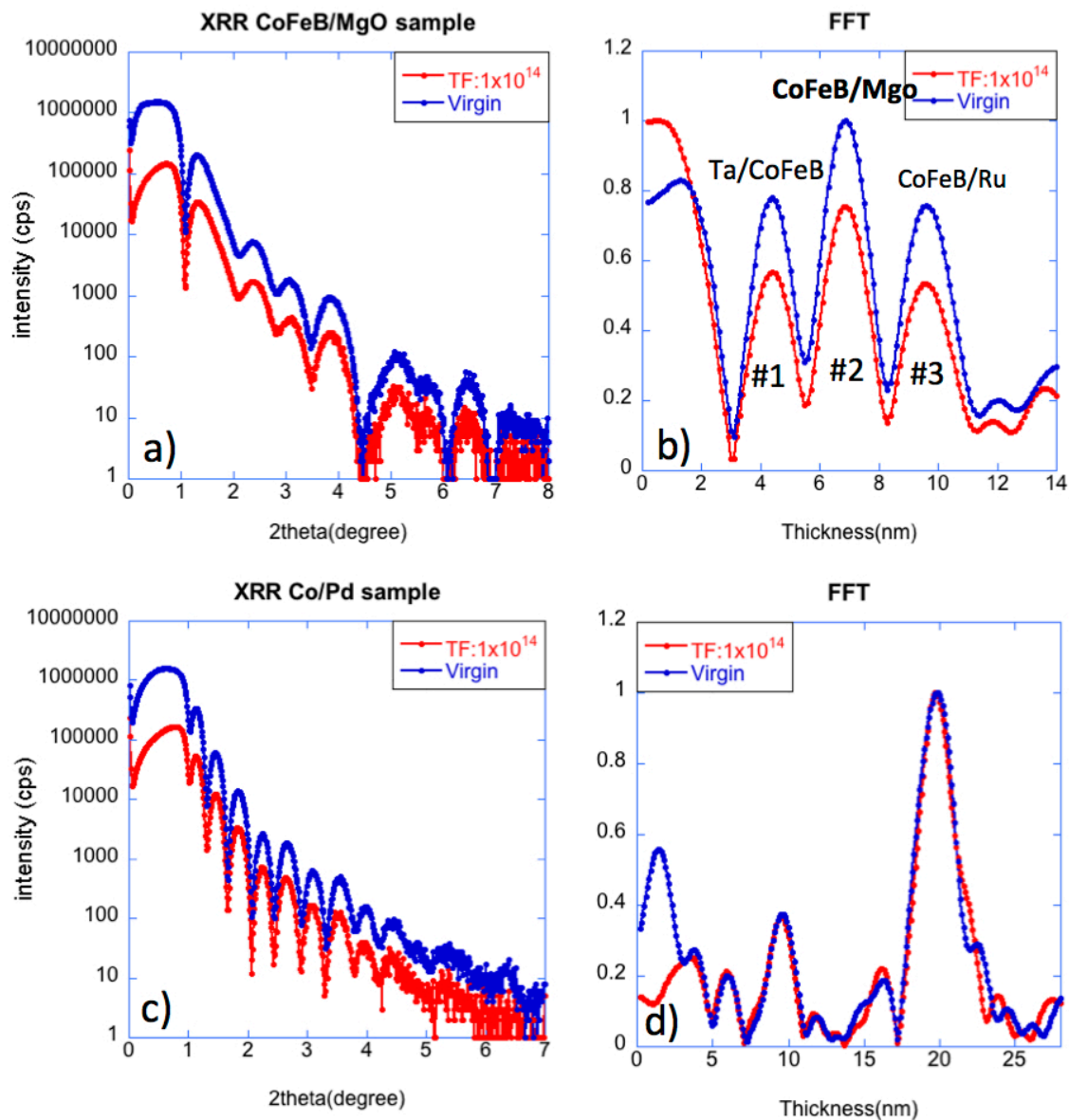


Figure 4.3 X-ray reflectivity spectra of (a) CoFeB/Mgo sample and (c) Co/Pd superlattice sample pre- and post- proton irradiation. The corresponding FFT of CoFeB/MgO and Co/Pd sample are also illustrated in (b) and (d) respectively.

As shown in **Figure 4.3b**, the FFT of CoFeB/MgO sample reveals 3 peaks; The Peaks #1 and #3 represent the interfaces of Ta capping and seeding layer respectively, while Peak#2 corresponds to the CoFeB/MgO interface. The Full Width Half Maximum

(FWHM) and position of peaks are summarized in **Table 4.2**. Peaks # 1 and #3 are broadened as indicated by the changes in FWHM. However, the FWHM of the #2 peak, which represent CoFb/MgO interface, is unchanged.

The broadening of the peaks in the FFT data suggests that some interfaces have become rougher after the irradiation. The change can also be attributed to the change in film density as the defects, such as clusters or voids, are introduced. These results imply that the changes in the microstructure caused by the irradiation mostly occurred at the capping and seeding layers of the multilayer structure. Another plausible mechanism for the peak broadening is the intermixing between CoFeB and MgO interfaces because the x-ray reflectivity cannot differentiate between the intermixing between the adjacent layers and the increase of interface roughness. Similarly, in Co/Pd superlattice sample, the FFT shows that the positions of interfaces except for the surface layer are mostly unaffected.

Table 4.2 Comparison of FFT Peaks before and after irradiation for CoFeB/MgO sample.

Peak#		Virgin	TF: $1 \times 10^{14} \text{ H}^+/\text{cm}^2$
1	FWHM	2.32	2.62
	Position	4.14	4.39
2	FWHM	2.39	2.38
	Position	6.43	6.87
3	FWHM	1.85	2.24
	Position	8.82	9.62

X-ray diffuse scattering (XDS) measurements are performed to investigate the displacement damages of interfaces. The 2θ angles are chosen from previous specular reflectivity ranging from 1 to 4°. Beyond a 4° angle, the background noise becomes so large that the diffused scattering spectra are not reproducible. **Figure4.4** shows the x-ray diffuse scattering (XDS) results from both the G1A and G3A samples before and after irradiation at the 2θ angle of 3°. The data have been corrected for the variation in the X-ray exposed volume of the sample with varying angle of incidence by multiplying with a factor $\sin(x)/\sin(\theta)$, which normalizes the data to sample volume[120]. XDS results show that the x-ray intensity is shifted from the central peak to the diffused background for both samples after irradiation. The similar shift of the diffuse scattering spectra is greater in the Co/Pd sample, indicating a larger increase in the surface roughness of the Co/Pd sample, which is in good agreements with the AFM results.

However, the profile of the XDS distributions remains relatively the same before and after the irradiation despite the changes in the intensities. The central peak of each rocking curve corresponds to the specular reflection, i.e., at this particular value of the ω -angle, the angle between the x-ray beam and the sample's surface (θ_1) is equal to the angle between the detector and the sample's surface (θ_2). The two other principal features in a typical rocking curve are known as Yoneda wings[104,115,116], which appear when the x-ray source or the detector forms an angle with the sample's surface equal to the critical angle. These results suggest that the lateral correlation lengths of the interfacial roughness for both samples are not modified by the displacement damage, which is also in agreement with the FFT of specular reflectivity. Similar results are also found for smaller fixed scattering angles.

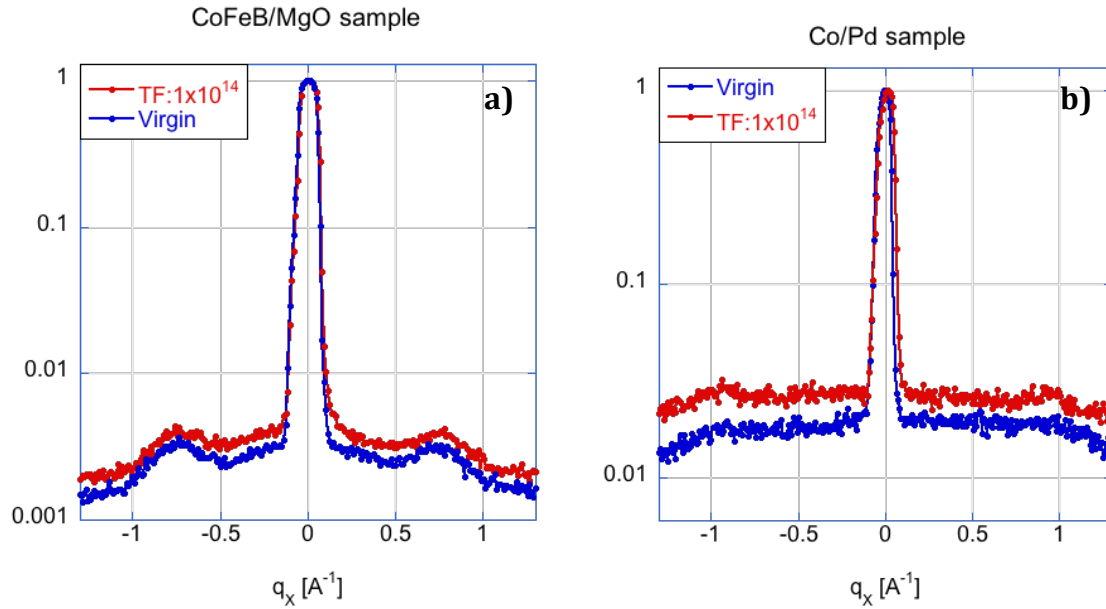


Figure 4.4 Semi-log plots of X-Ray diffraction scattering curve for 2θ fixed at 3° of CoFeB/MgO sample (a) and Co/Pd superlattice sample (b)

XRR and XDS results suggest that only small displacement damages occurred at the interfaces of magnetic layers despite of the significant roughening observed at the surface of the MTJ stacks. In addition to the possible formation of H_2 bubble that is likely to occur in Si substrate, there could be another mechanism that drives irradiation-induced defects away from the interfaces of magnetic layers i.e. to capping and seeding layer. The thick capping and seeding layers can act as defect sinks, and the point defects can diffuse toward these interfaces through the thermal diffusion[117,118,121-123]. However, the intermixing and the rough interfaces themselves are also difficult to discern from each other in the nm lengthscale. Another plausible reason is that the XDS measurements cannot resolve such the irradiation-induced changes that result from the intermixing and the interface roughness.

(ii) Magnetic properties

Figure 4.5 shows the magnetic properties of the half structures before and after proton irradiation. The in-plane VSM demonstrates that the magnetic moment of both G1A and G3A sample are virtually the same before and after irradiation. The CoFeB/MgO stack establishes soft magnetic properties as the magnetization become saturated ~ 0.5 T. The corresponding MOKE signal also suggests that the perpendicular anisotropy is unaffected by the irradiation as the out-of-plane magnetization loops remain unchanged. The coercive field persists the same value, $H_C \sim 0.015$ T, despite the increase of RMS roughness in which usually induces domain wall pinning mechanism. The result indicates that the magnetization reversal process in the CoFeB film is not affected after the proton irradiation. Similar results have been observed in Co/Pd superlattice samples.

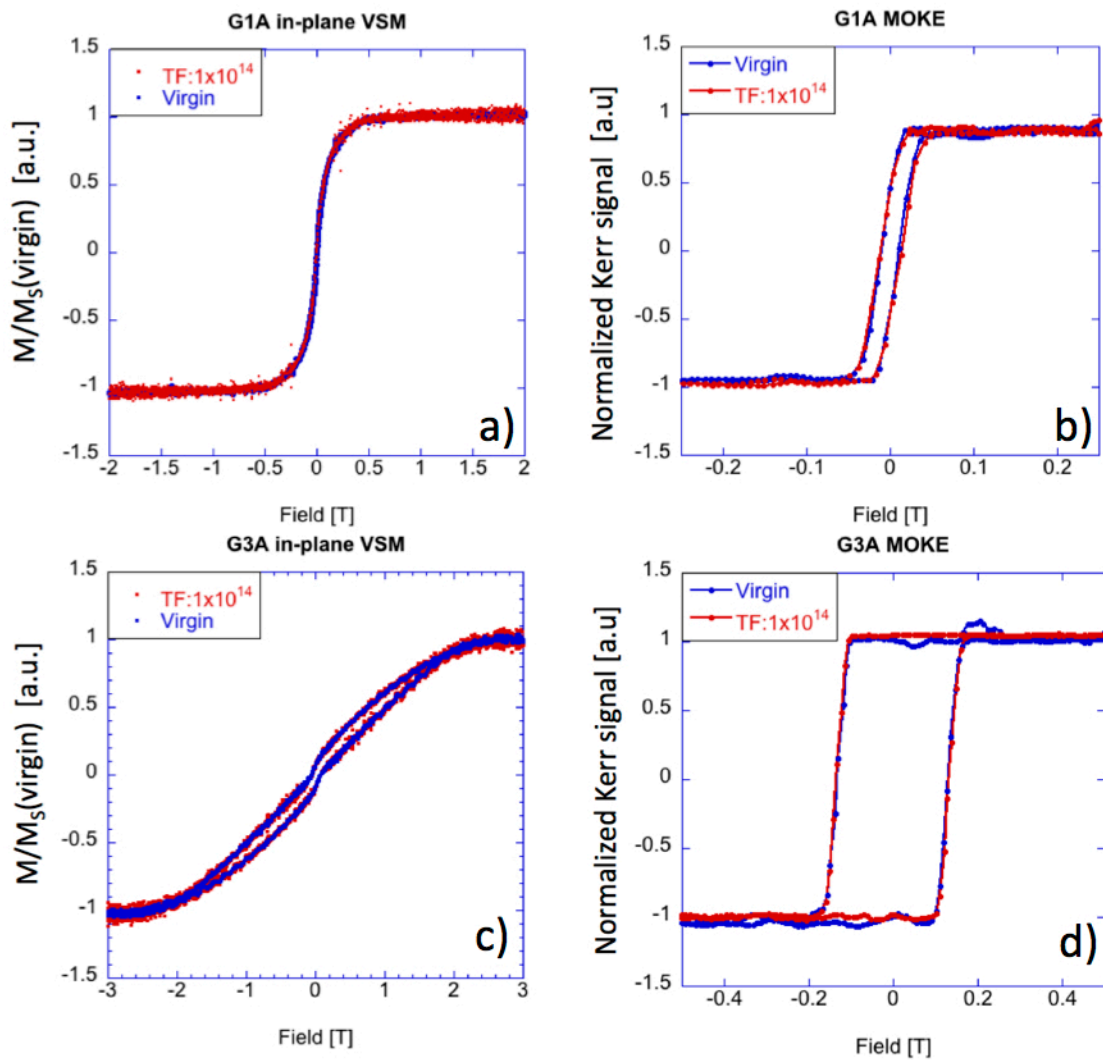


Figure 4.5 In-plane hysteresis loops of virgin and irradiation for G1A (a) and G3A (c) samples and MOKE measurement of G1A (b) and G3A (d)

The magnetic properties of CoFeB/MgO and Co/Pd materials strongly correlate with the interfaces of magnetic and non-magnetic layers. In both systems, the origin of PMA in was due to the broken symmetry at the interfaces [119,124] [120,125]. Consequently, any modifications of these interfaces will directly result in the changes in

the magnetic properties of materials, particularly the magnetic anisotropy. The modulation of M_S due to the intermixing of Co/Pd has been reported previously as the result of the ion irradiation [64,126]. Small changes of magnetic properties are observed in G1A and G3A after irradiation, suggesting the minimal change in the interfaces induced by the 2 MeV proton beam. This is consistent with the observation in previous section that the interfacial roughening is mainly from surface and/or seed layer interfaces.

4.2.2 PMTJ stack

Two PMTJ wafers with the identical structure provided by Grandis are examined. The wafers are diced into small samples for characterizations. The initial fluence of $1 \times 10^{14} \text{ H}^+/\text{cm}^2$ is used for both PMTJs #1 and #2 samples. PMTJ#2 sample is then re-irradiated to a total fluence of $1 \times 10^{15} \text{ H}^+/\text{cm}^2$ for comparison with multilayer stacks while PMTJ#1 is irradiated up to $5 \times 10^{15} \text{ H}^+/\text{cm}^2$ to evaluate the failure threshold. The same characterizations are performed for all the samples. In addition, the Resistance-Area product (RA) and TMR are determined via the in-plane transport measurement technique (CIPT) at Grandis Inc.

(i) Morphological and structural characterization

As shown in **Figure 4.6**, the as-received sample is very smooth with the RMS roughness of $\sim 0.2 \text{ nm}$. After irradiation, the similar features as seen in the half structure samples are formed at the surface of the films with the heights of 5~60 nm. Consequently, the surface roughness of the films increased to 3 nm for the total fluence $1 \times 10^{15} \text{ H}^+/\text{cm}^2$ as shown in **Figure 4.6b**, and to 2 nm for total fluence $5 \times 10^{15} \text{ H}^+/\text{cm}^2$ as shown in **Figure 4.6c**.

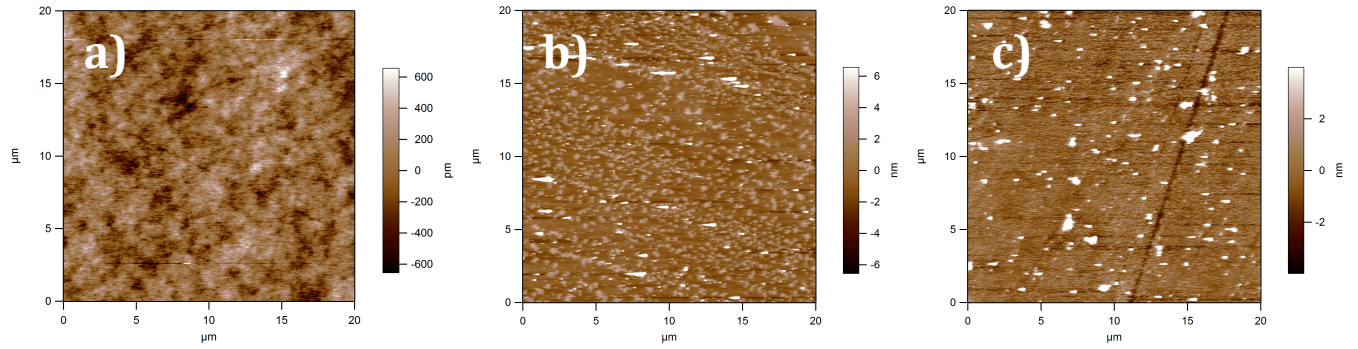


Figure 4.6 AFM images over 20 by 20 μm^2 of (a) as received, (b) total fluence of 1×10^{15} H^+/cm^2 and (c) total fluence of 5×10^{15} H^+/cm^2 respectively

Figure 4.7 shows the x-ray reflectivity spectra and their corresponding FFT data for PMTJs #1 and #2 samples. The reflectivity spectrum is normalized for a simple comparison. The x-ray intensity decreases after irradiation due to the increase in the surface roughness. The results have shown very little changes due to the irradiation. The corresponding FFT curves once again show that only on capping layer and seeding layer of the PMTJ structure seem to be affected by irradiation. The dash lines are added to guide the eyes representing the interfaces of Ta capping layer/CoFeB and Co/Ta seeding layer.

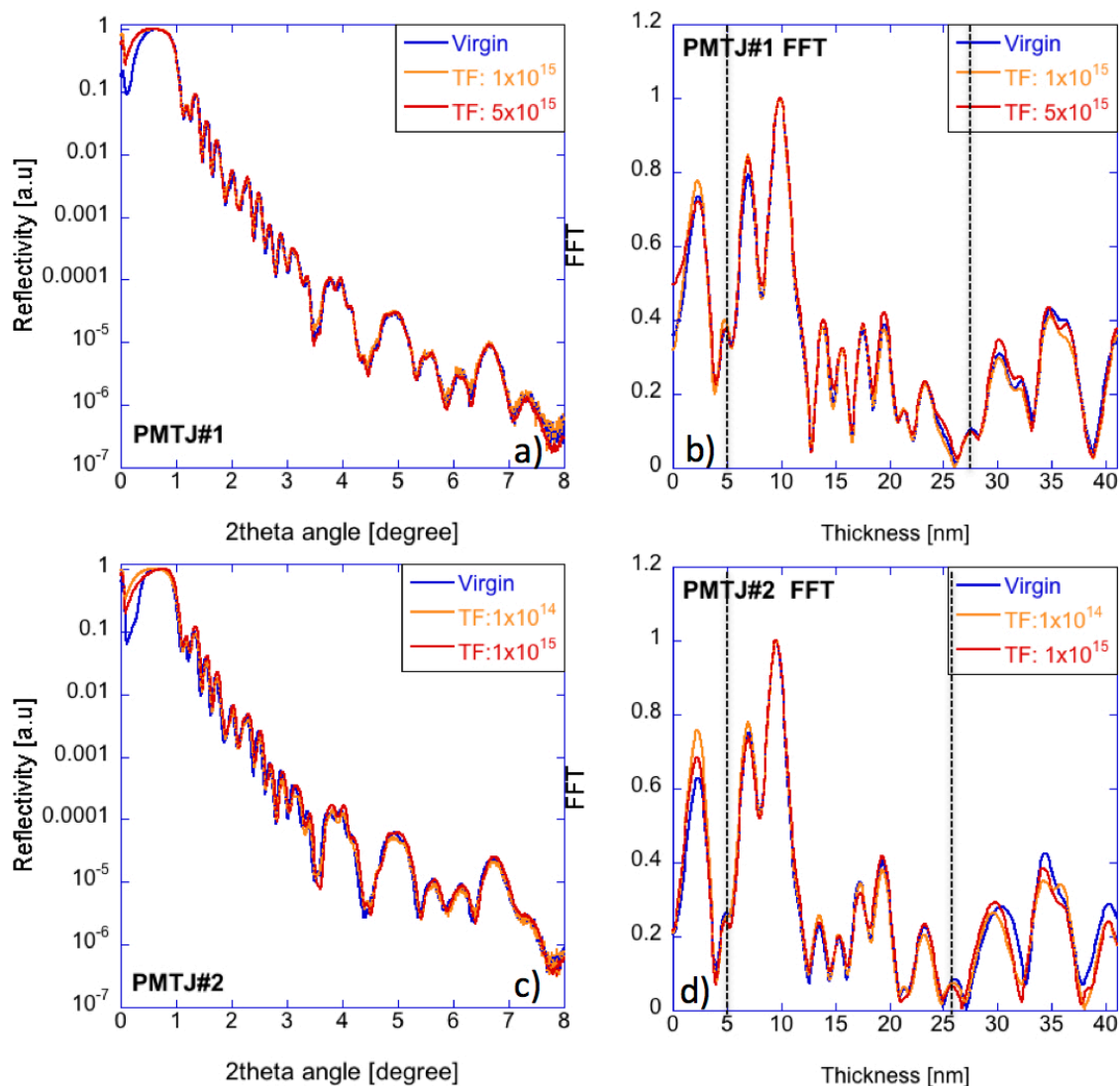


Figure 4.7 Pre-rad and post-rad x-ray reflectivity comparison of PMTJ#1 is shown in (a) and PMTJ#2 in (c) The corresponding FFT of PMTJ#1 and PMTJ#2 samples are demonstrated in (b) and (d) respectively. The dash lines represent capping layer interface and seeding layer interface.

XDS is also performed on PMTJ #1 at fixed 2θ from 1.29° to 4° and the results are shown in **Figure 4.8**. Very similar to the results observed in G1A and G3A samples, the intensity of diffused background slightly increased. The normalized XDS plots indicate that there is a very small change in lateral correlation length after final irradiation

with total fluence of $5 \times 10^{15} \text{ H}^+/\text{cm}^2$. Similar results are also observed in PMTJ#2 samples. Despite the increase of surface roughness, XDS results indicate that there is no observable change on the interface of the PMTJ structure. Thus we conclude that the PMTJ structures are robust to the 2 MeV proton beam with the fluence up to $5 \times 10^{15} \text{ H}^+/\text{cm}^2$, except for the surface and seeding layers.

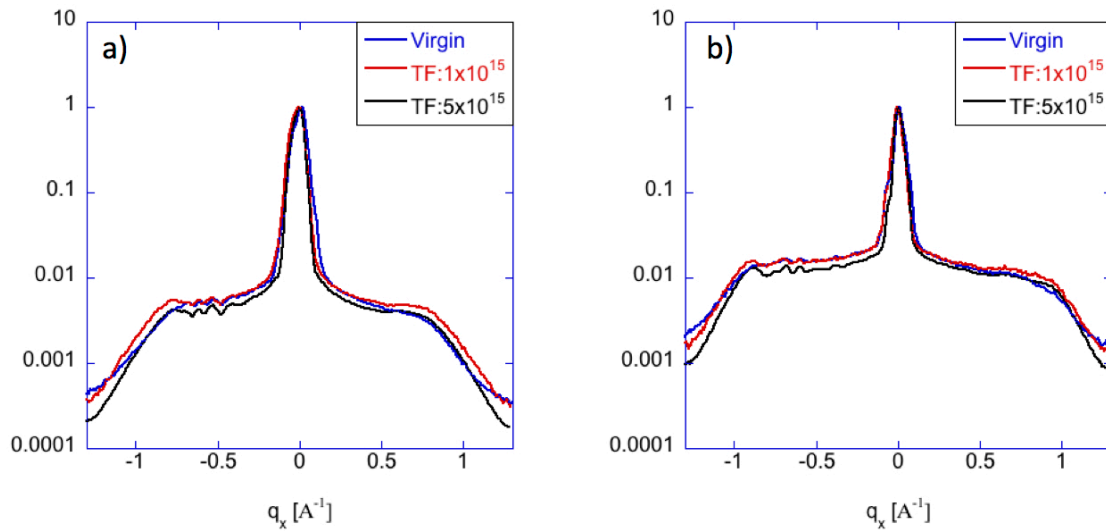


Figure 4.8 XDS curves of PMTJ#1 at fixed $2\theta = 2.01^\circ$ (a) and 2.89° (b)

(ii) Magnetic properties

MOKE is used in addition to investigating the magnetization reversal behavior of the PMTJ#1 stack as shown in **Figure 4.9**. Similar M-H loops are observed except for the rapid magnetization switching around 0 field. This is due to the lower sensitivity of the MOKE as compared to the VSM. It appears that the magnetization reversal of the PMTJ is unaffected by proton beam up to $5 \times 10^{15} \text{ H}^+/\text{cm}^2$. Out-of-plane hysteresis loops for the virgin and irradiated samples are studied by VSM. The magnetization loop is a

combination of free layer and SAF pinned layer switching in responses to an applied magnetic field. The rapid change of the moment around 0 field is observed, indicating the free layer switching. The pinned layer also shows an exchange bias that shifts hysteresis away from 0 field symmetrically for a negative and a positive field. The magnetization loops before and after irradiations appear to be identical (no measureable differences).

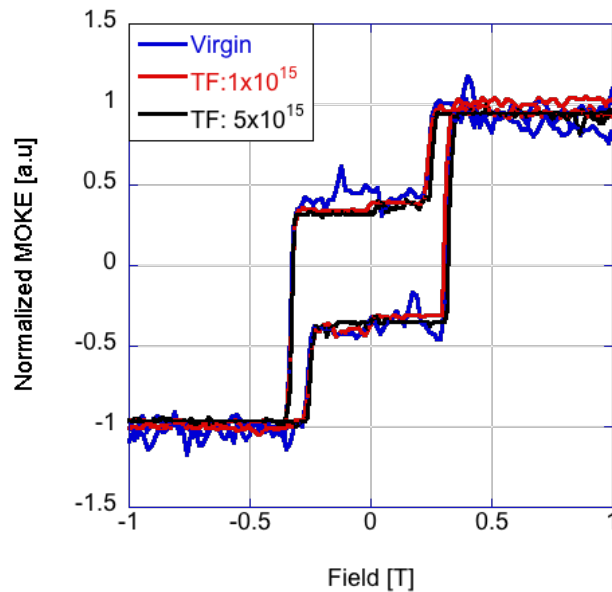


Figure 4.9 MOKE measurement of PMTJ as a function of proton total fluence. MOKE loops demonstrate that PMA of PMTJ is unaffected by irradiation up to $5 \times 10^{15} \text{ H}^+/\text{cm}^2$.

(iii) Transport measurement

Tunneling magnetoresistance (TMR) and RA product are measured before and after irradiation. The results are summarized in **Table 4.3**. TMR and RA values are almost the same (within measurement error of 5% by CIPT measurement standard) throughout each irradiation step. The results suggest that there is no significant change to MgO tunnel barrier as well as the free and fix layers. The transport results

confirm the observed change in the microstructures and the interfaces of the PMTJ wafer.

Table 4.3 CIPT measurement of PMTJ stack

Sample ID	TF [H^+/cm^2]	RA [$\Omega \cdot \mu\text{m}^2$]	TMR[%]
Wafer#1	0	6.9	98
	1×10^{14}	7	93
Wafer#2	0	8.97	99.6
	1×10^{15}	8.9	100.1

4.3 Effects of irradiations on PMTJ devices

4.3.1 Pre-irradiation characterization of PMTJ devices

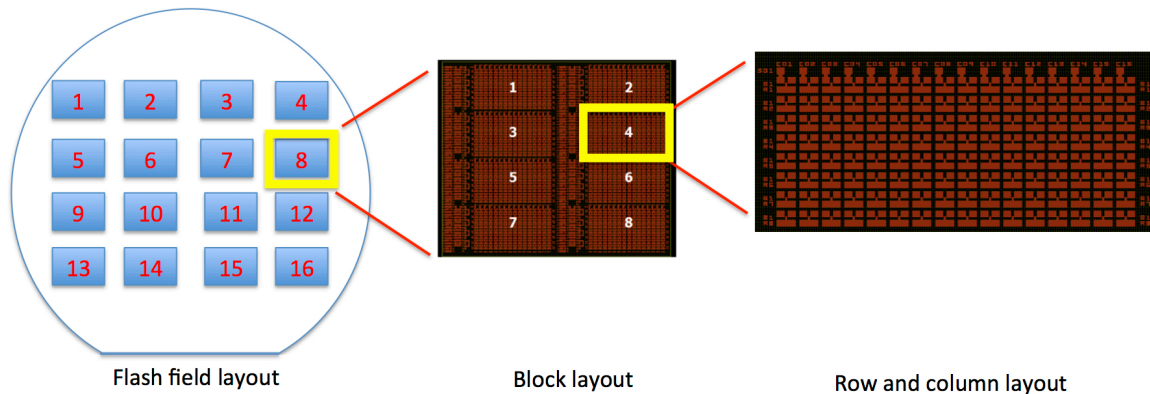


Figure 4.10 Devices layout with diameter ranging from 20 – 500 nm. Each devices are labeled according to their position including flash field(F), block(B) , column(C) and row(R).

PMTJ devices are fabricated on a 4" wafers using electron beam lithography at Grandis. The size of the device on the wafer varies from 20 – 500 nm in diameter. Each device is labeled according to its position containing flash field(F), block(B), column(C) and row(R). The 16 flash fields are shown in **Figure 4.10**. Each flash field consists of 8

test is performed by applying 100 repeated read voltage pulses.

I-V characterization is performed on ~100 devices across the wafer. Devices with the sizes below 50 nm tend to be either short or open, yielding ~ 25% of working devices while those with the sizes above 50 nm yield more than 80% of working devices.

Following I-V test, functionality and retention tests are performed on 60 – 500 nm devices. These results are included in pre-irradiated data (~63 devices). **Figure 4.12** illustrates a functionality test of a 150 nm device. Here only first 12 cycles of switching between high current (low resistance) state and low current (high resistance) state are shown.

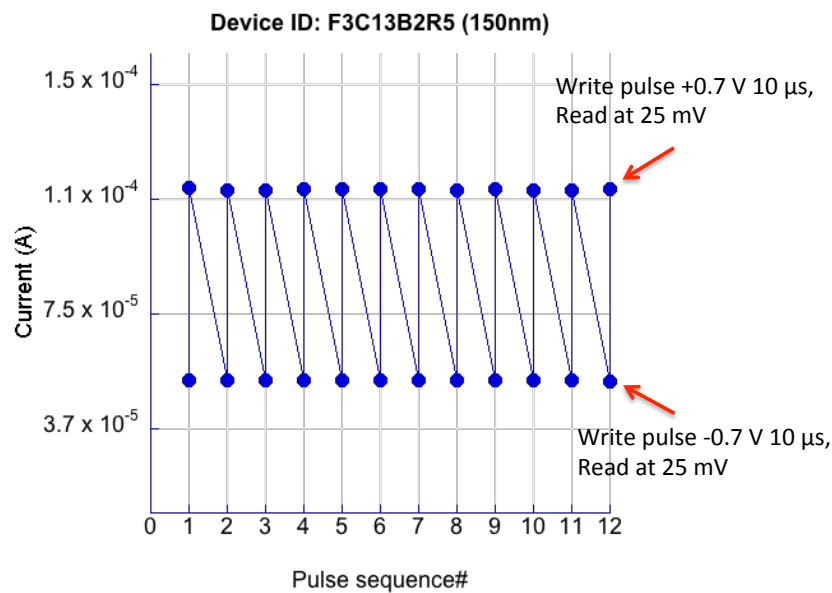


Figure 4.12 Functionality test result of a 150 nm pMTJ device represents switching characteristic. A sequence is defined as a negative voltage pulse and current measurement at 25 mV followed by a positive voltage pulse to change resistance state and same current measurement at 25 mV

Figure 4.13a shows the high and low resistance state of all pre-rad devices. In terms of the device-to-device variability, the smaller device's resistance states, particularly in the devices size below 90 nm, are more scattered as indicated by the standard deviation of the resistance states as summarized in **Table 4.4**. The lithographic process of MTJ is responsible for the inconsistency as it causes the deviation of the actual device size from the nominal device size. Such deviation is typically more severe in smaller devices.

Table 4.4 Pre-rad device-to-device variability of high and low resistance state of MTJ devices

Device diameter (nm)	Sampling size (number of devices)	R_{High} average (Ohms)	R_{High} Standard deviation (%)	R_{Low} average (Ohms)	R_{Low} Standard deviation (%)
60	10	12255	31.26	5514	32.26
70	9	13088	20.92	5805	19.12
80	9	13741	14.66	6181	15.84
90	6	5746	7.37	2667	4.55
150	9	2007	6.11	878	7.09
300	9	437	8.38	204	7.55
500	11	160	9.66	75	9.95

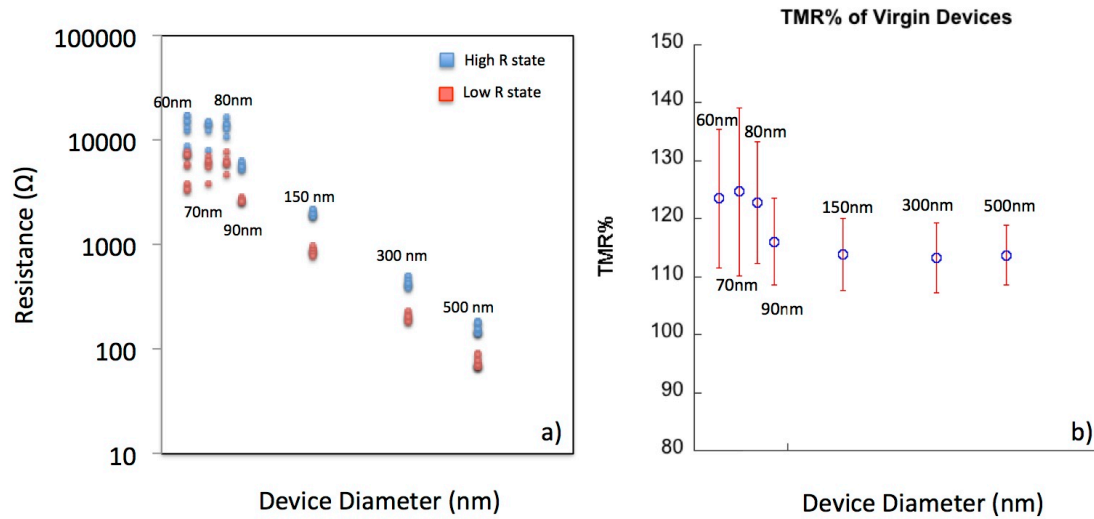


Figure 4.13 (a) R_{High} and R_{Low} of PMTJ devices as a function of the device size. The resistance data is from the conversion of current measurement from functionality test **(b)** Average TMR of PMTJ devices as a function of device size.

The TMR% is calculated for each pre-rad device by the relation

$$TMR\% = \frac{R_{high} - R_{low}}{R_{low}} \times 100 \quad 4-1$$

TMR% result is shown in **Figure 4.13b**. The average TMR% of device is more than 120% for device below 90 nm and decrease to $\sim 113\%$ as the size of devices increase. The standard deviation of TMR% for device size below 90 nm is more than 10 % and less than 8% for bigger device. TMR% is not dependent on the resistance but the resistance ratio of the two states, thus, the variation of size does not necessarily reflect in the dispersion of TMR%. The TMRs and its corresponding standard deviations for 150, 300 and 500 nm devices are almost identical indicating that PMTJ stack is very uniform. In contrary for sub-100 nm devices, TMR% shows larger fluctuations, which represented more significant device-to-device variability, suggesting that TMR behavior is influenced

by the localized structure/effects and that makes the characterization of small devices more suitable to probe single electron event (SEE) during the irradiation.

4.3.2 Radiation species and the total fluence

Different radiation species were employed to study the induced displacement and ionization damages. The energy and fluence of radiation sources are chosen in exceed of minimum requirements for radiation hardness assurance test standard of CMOS devices developed in the US and Europe such as *JEDEC Test standard 57* and *ESA/SCC25100*. A comprehensive review of radiation hardness assurance testing on CMOS devices can be found in Ref[127].

The radiation procedures are shown in **Table 4.5**. The irradiation is done on selected flash fields of the wafer using an aluminum mask as the shielding material. Before each irradiation, devices are shorted to eliminate the ESD effect during the irradiation. The resistance states of the devices are also set at specific states prior to the irradiation. After the irradiation, each device firstly undergoes the retention test to determine whether the pre-set state is changed after the irradiation. Then the functionality test is implemented to examine the characteristic of the spin torque switching.

Table 4.5 Various irradiation sources and their corresponding damages that performed on PMTJ devices

Radiation source	Charge	Dose	Displacement damage	Ionization damage
10 keV x-ray	Neutral	1Mrad (Si)	No	Yes
2 MeV Neon	Neutral	$1 \times 10^{11} / \text{cm}^2$	Yes (~1500X proton's)	Rare
2 MeV Proton	Positive	$1 \times 10^{12} / \text{cm}^2$	Yes	Yes
10 keV x-ray(1 st) + 2 MeV Neon	Neutral	1Mrad (Si) + $1 \times 10^{12} / \text{cm}^2$	Yes (from Ne)	Yes (from x-ray)

4.4.3 Post-irradiation characterization

(i) X-ray irradiation and the effect on localized annealing

The 10 keV energy x-ray is used to irradiate Flash fields F2, F3, F5 and F12 with the total number of 16 devices. Prior to the irradiation, half of the devices has been pre-set to the R_{low} state and the other half to the R_{High} state. The x-ray irradiates on the flash fields in an accumulated fashion with the flux of 1000 rad/s for 1000 seconds until the total dose is 1 Mrad of the equivalent absorption dose of the reference Si.

Figure 4.14a shows a subset of the switching characteristic of the virgin and post-irradiated devices. The x-ray exposure does not show an impact on the functionality of all the devices. The TMR is calculated from the average high and low current state from functionality test. The retention test of this device is shown in **Figure 4.14b**. The device state appears to survive the x-ray exposure as it retained the preset value. However, it is noticed that one device with a 150 nm diameter fails to retain the pre-set resistance state as it switched to a different resistance state after the x-ray irradiation. The device

retention and functionality tests are also performed on this particular device. The device appears to function normally as the other devices. It is unclear what causes the change of the pre-set state. It is unlikely that the radiation affects the coupling of ferromagnetic free and fix layer since this device showed the good stability during the retention test as well as a normal switching characteristic.

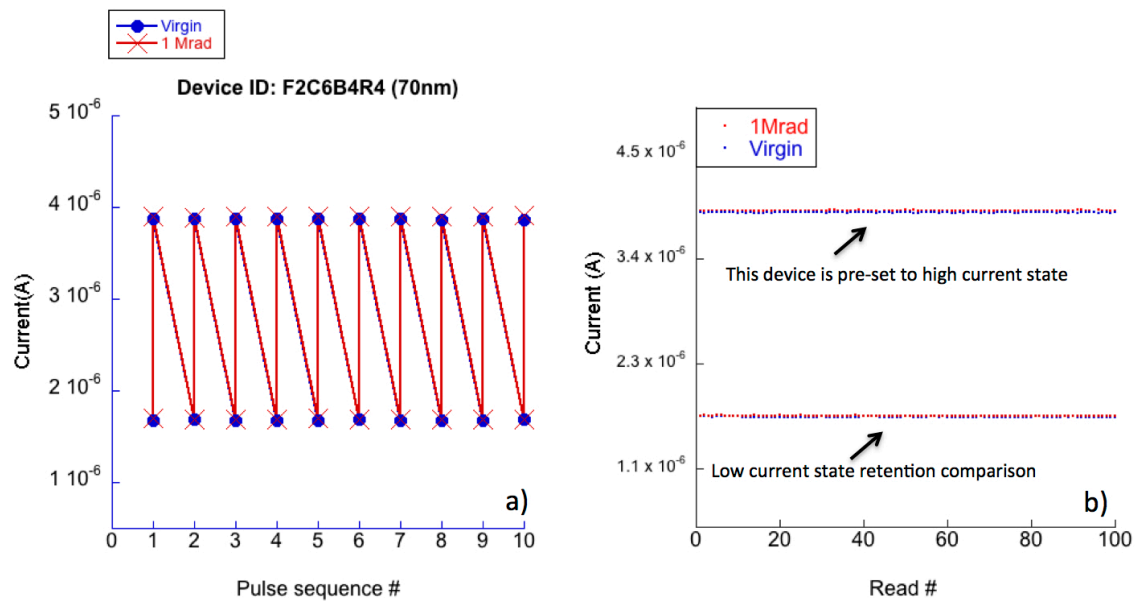


Figure 4.14 (a) Functionality test of a 70nm device pre-rad and post-rad (1Mrad) (b) retention tests on the same device pre-rad and post-rad comparison. The device was pre-set to high current state. Additional low current state retention was performed only for this device.

As shown in **Figure 4.15a**, TMR of the devices below 100 nm is unaffected while TMR of larger devices actually increases after x-ray irradiation. The TMR variation after the exposure is shown in **Figure 4.15b**. The small fluctuations of TMR (less than 2%) in sub-100 nm devices are likely from the measurement errors, as the probe tips have to be engaged manually for every measurement. The deviation of current measurement due to

the engaging and retracting of probe tips has been examined. With the sampling size engaged and retracted more than 50 times, the variation of current read is less than 1%. Therefore, the increase in the TMR is clearly the result of the x-ray irradiation. The improvement of TMR is likely due to the local annealing induced by the x-ray.

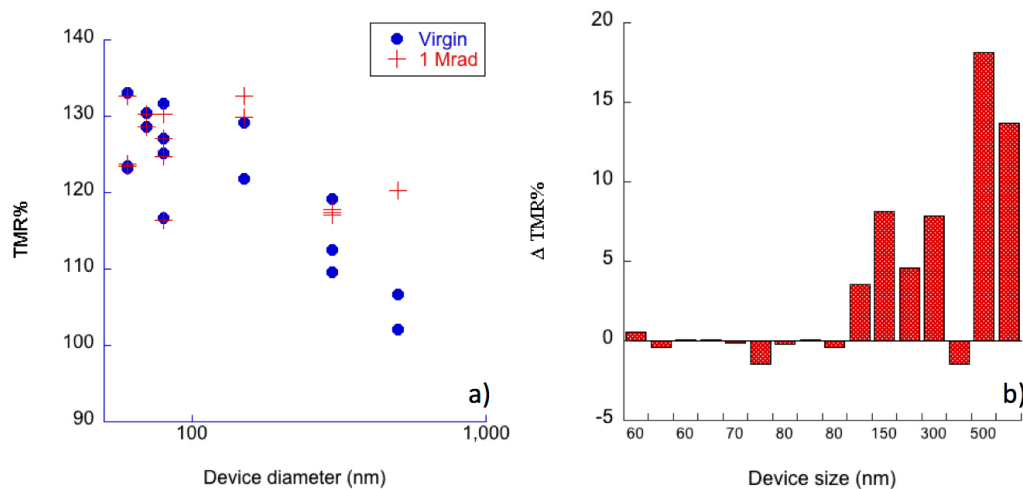


Figure 4.15 (a) A comparison of TMR (calculated from functionality data) plot as a function of device sizes **(b)** Change in TMR as a function of device sizes after the x-ray exposure

In contrary to the conventional annealing, x-ray ionization is capable of indirectly annealing the PMTJ via photoelectric effects that utilize adiabatic heating from the aftereffects of electronic excitations of elements—from elements to environment[128]. In a simple approximation, ones can assume that the total absorbed energy is converted into heat and increase sample temperature by

$$\Delta T_{sample} \propto N\sigma E \quad 4-2$$

where N is the number of x-ray photons (equivalent to dose), E is the photon energy and σ is the photoelectric cross section[129]. The induced heating is predominantly attributed

from high Z atoms, especially Fe and Co due to the high ionization energies and high photoelectric cross sections. **Table 4.6** lists the ionization energy, and the absorbed photoelectric cross section ratio of elements with Si as the reference at the photon energy of 10keV [129]. The dominant role of x-ray absorption in Co and Fe indicates that the CoFeB layers are responsible for generating most of the heat after electronics excitation that anneals MgO barrier.

Table 4.6 Comparison of ability to absorbed x-ray and first ionization energy of individual PMTJ materials

Element	Atomic number	σ/σ_{Si} at 10 keV photon	1 st ionization energy (eV)
B	5	0.045	8.298
Mg	12	5.5	7.6462
Fe	26	200	7.9024
Co	27	125	7.8810
Ru	44	45	7.3605
Pd	46	5	8.3369
Ta	73	7.5	7.5496

The TMR of MTJs strongly depends on the annealing conditions. Many annealing conditions have been studied. The optimized annealing conditions result in higher TMR values [76,130-132]. Wang et al[133] identified the evolution of TMR in 3 regions: rapid increase in TMR (usually more than 40%) is from rapid crystallization of CoFeB; follow by slowly enhance which due to the improvement of the MgO crystal structure; and the decrease of TMR from increased diffusion at prolonged annealing. In this case, the slightly increase of TMRs are likely from the improvement of CoFeB/MgO interface that enhances the spin filtering in the tunnel barrier.

(ii) Proton irradiation

2 MeV proton beam radiation has been performed on Flash fields 14 and 15. The same tests are done on 7 devices (60nm, 70 nm, 80 nm, 150 nm, 300 and 2 of 500 nm) after the exposure. The estimated numbers of particles hit as a function of device sizes are listed in **Table 4.7**

Table 4.7 Estimated total number of proton hits per device

Device diameter (nm)	Surface area (cm ²)	# of proton hits per device	Total fluence (H ⁺ /cm ²)
60	2.82 x10 ⁻¹¹	29	1x10 ¹²
70	3.85 x10 ⁻¹¹	39	1x10 ¹²
80	5.03 x10 ⁻¹¹	51	1x10 ¹²
150	1.77 x10 ⁻¹⁰	177	1x10 ¹²
300	7.07 x10 ⁻¹⁰	707	1x10 ¹²
500	1.96 x10 ⁻⁹	1960	1x10 ¹²

Three sub-100 nm devices fail to retain the pre-set state. One 60 nm device exhibits an unstable behavior as shown in **Figure 4.16**. The device randomly switches between two resistance states during the 100 repeated reads at only +25mV. The corresponding functionality test is shown in **Figure 4.17**. One failed switching is observed. Similar behaviors have been observed in a 80 nm device as the proton irradiation changes the pre-set state as well as causes the instability during the retention test. The irradiation also modifies functionality of the device in which skipping cycle is observed during the switching characterization. For the 70nm device, the pre-set state is also changed. However, both retention and functionality tests are normal—no skipping cycles and switching states during read. For devices larger than 100 nm, the proton irradiation has no observable effects on the performance of devices.

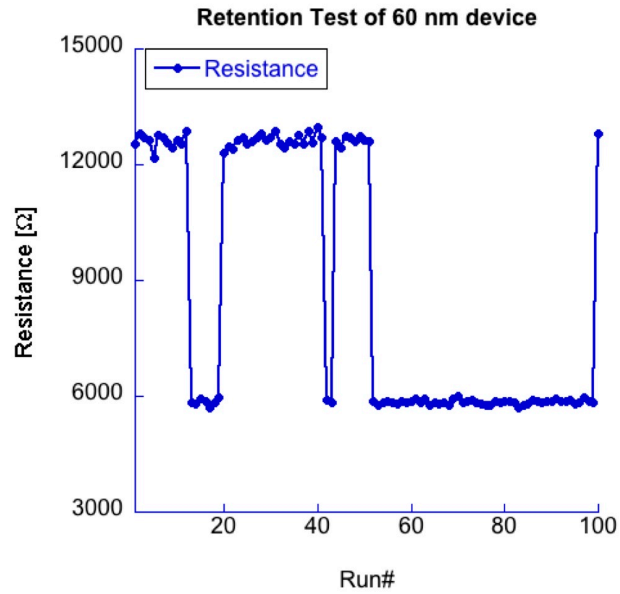


Figure 4.16 Retention test on 60 nm device after proton exposure. The device exhibits an unstable state that randomly switches between the high and low resistance states during repeated read.

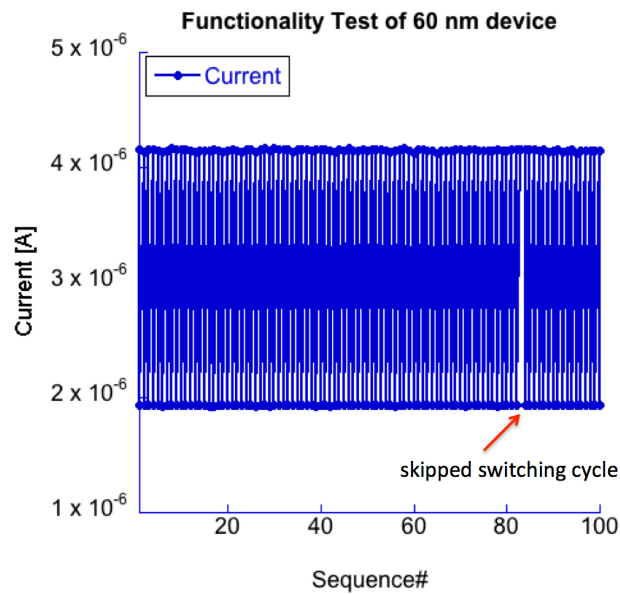


Figure 4.17 Functionality test of the same 60nm device shows that the device failed to switch after write voltage pulse was applied around the 83th cycle

The postmortem TMR as a function of the device sizes is shown in **Figure 4.18**. There are very small changes (less than 2%) after proton irradiation, which implies no changes in the microstructure of PMTJ as opposed to the x-ray irradiation. This is due to a much less heating effect of proton compared to the x-ray whose energy solely contributes to ionization damage.

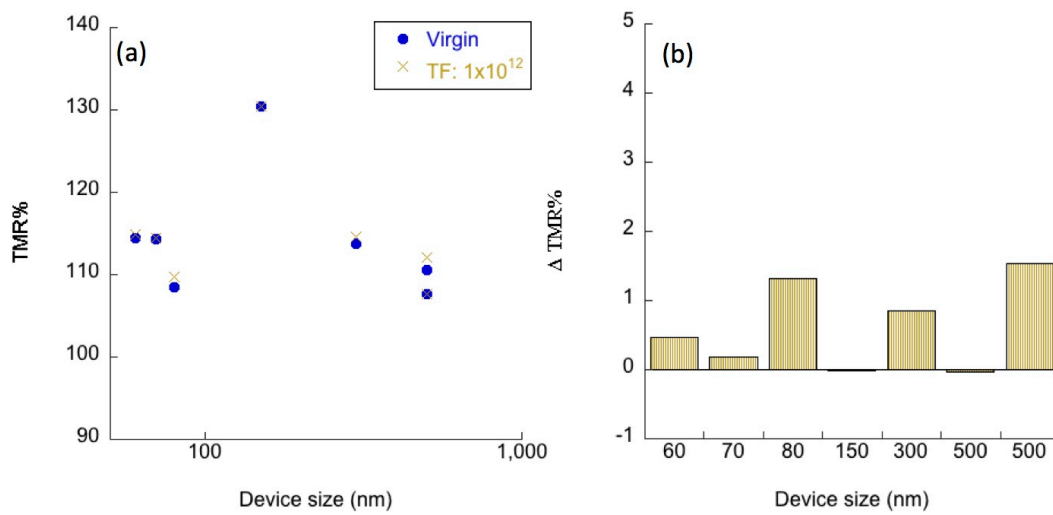


Figure 4.18 (a) TMR vs. Device sizes for before and after proton irradiation. The total fluence is $1 \times 10^{12} \text{ H}^+/\text{cm}^2$. **(b)** $\Delta \text{TMR}\%$ of devices after Neon exposure.

Hughes *et al.*[95] conduct similar proton irradiation on CoFeB/MgO based MTJ with the in-plane magnetization easy axis. No detectable changes have been observed, which concludes that the in-plane MTJ is “Rad Hard” for proton irradiation. However, for PMTJ the instability of resistance state during the retention test is observed. Two possible mechanisms can lead to the modification of interlayer coupling and the alteration of thermal.

Proton irradiation can modify the interface roughness via displacement damage that ultimately change the interlayer coupling. However, the XDS results of PMTJ wafer suggest that there is no significant change in the interface roughness. However, XDS gives the macroscopic information over a large area, which may differ from the individual device's that is usually driven by a single event effect (SEE) phenomenon that is significant in a microscopic scale. This assumption is later validated by heavy ions Neon in which generate ~ 1500 times of *dpa* than that of the proton beam.

The perpendicular magnetic anisotropy between oxide and ferromagnetic metal is attributed to the hybridization of the Fe *3d* and O *2p* orbitals[75] while the in-plane MTJ is usually dominated by shape anisotropy due to a demagnetization field[58]. In the previous report[75], the magnetocrystalline anisotropy of Fe can be modified by the electric field. Thus, the interfacial anisotropy between CoFeB and MgO is sensitive to the external electric field. For example, Maruyama and collaboration shows that a relatively small electric field (less than 100 mVnm^{-1}) can effectively change the magnetic anisotropy of Fe(001)/MgO(001) junction [134]. The effect of the local electric field on magnetization switching of perpendicular CoFeB-MgO junction has also been investigated by Kanai *et al.* stating that the applied static electric field temporal change easy axis of CoFeB to in-plane that trigger the magnetization precessional motion[135].

Protons can directly ionize atoms via the fundamental interaction through the Coulomb force to generate electron-hole pairs along its path. The electrons or holes that escape the recombination can be trapped at the interface or on oxide insulator that create non-transient localized electric field after the irradiation. This phenomenon is commonly observed in Si based MOS devices[136]. The induced electric field near the MgO/CoFeB

interface can change the magnetic anisotropy of the free layer and reduce its thermal stability, and result in the unintentional switching during the retention test.

(iii) Neon irradiation

The Neon beam with energy 2 MeV is used to irradiate F7 and F2 with the fluence of 1×10^{11} and 1×10^{12} /cm² respectively. Three virgin devices in F7 with diameter 60nm, 80nm and 150nm are used to study the effects of the Neon irradiation alone. Six devices in F2, which have already been exposed to total ionization dose of 1Mrad of x-ray beam, are irradiated with Neon with the fluence of 1×10^{12} /cm² to study the combined effects of x-ray/Neon irradiation.

On the switching characteristic, all devices perform normally as they complete 100 cycle tests without skipping. All devices retain their pre-set states that remain stable during the retention test. The TMR analysis of Neon only irradiation is shown in **Figure 4.19**. TMR values remain relatively unchanged (change less than 2% which is comparable to experimental error).

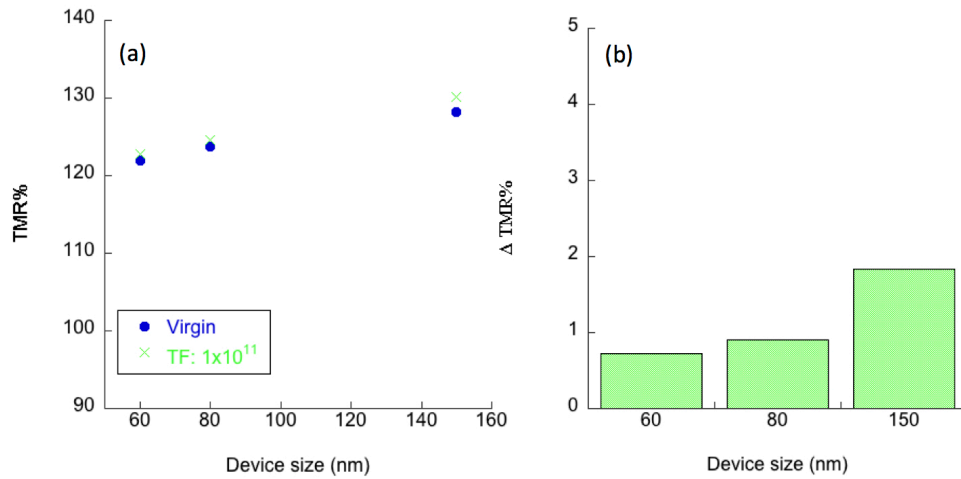


Figure 4.19 (a) Comparison pre-rad and post Neon exposure TMR value as a function of device size **(b)** TMR variation of devices after Neon fluence 1×10^{11} ions/cm²

TMR for F7 devices are shown in **Figure 4.20**. TMR is degraded for sub-100 nm devices. The deterioration of TMR is likely related to the induced disorder of the MgO barrier by the Neon beam. For one particular 60 nm device, the TMR decreases $\sim 8\%$ after the exposure. Noticing that this device possesses high original TMR ($\sim 133\%$) that translate to high quality of the crystal structure of MgO before Neon exposure, therefore, the displacement damages are more pronounced in this device.

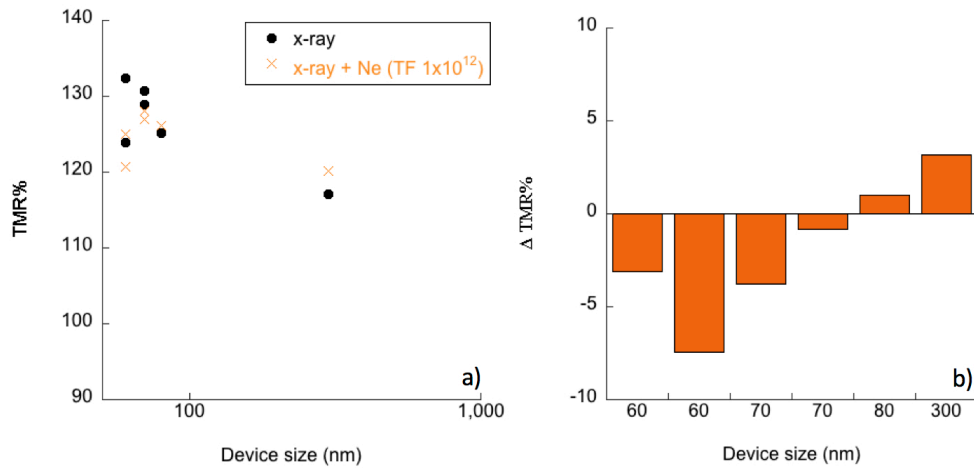


Figure 4.20 (a) TMR vs. device size before and after Neon fluence 1×10^{12} ions/cm² **(b)** Δ TMR of devices after Neon exposure

In the past, the performance of MTJ after the heavy ion irradiation has been described but mostly on MTJs with Al₂O₃ barriers [92,93,137-139]. The change in the TMR in post-irradiation MTJs varied greatly in accordance to the radiation species, their energy, and the total fluences.

A previous study [140] has reported that the heavy ion irradiation (15-MeV Si ions) causes a very small degradation (~1%) in resistance, but no significant changes in the retention state and time before and after irradiation. Katti *et al*[141] also performed heavy ion irradiation on 1Mbit MRAM and found that there is a negligible change in bit resistance after 940 MeV Bi ions bombardment with total fluence in excess of 9×10^9 ions/cm².

Sacher *et al*[93] investigated the effects of the damage to Al₂O₃ barrier layer using low energy He⁺ and Ar⁺ ions with energies from 15 to 105 eV. The degradation of TMR was more pronounced in Ar⁺ due to the more energy loss per unit depth that caused Ar⁺

ions stop in the barrier layers. The heavy ion irradiation effects on MTJ (both MgO-based and Al₂O₃) mostly focused on the effect on displacement damages on magnetic layers and tunnel barrier. Based upon the literatures and our comparison results of charged particles H⁺ and neutral Neon ions, it appears that the direct ionization from charged ions on MTJ has more impacts on the intrinsic properties of MTJ.

4.5 Summary

For the PMTJ multilayer structure, proton irradiation has no effect on large area films as characterized except for hillock features, which increase the overall RMS roughness of the film. In the PMTJ film stack, the radiation response to single events effect (SEE) is distinct from that due to the displacement damage, which increases surface/interface roughness. In single events, only transient phenomena related to the ionization are considered because the displacement damage along the particle path and the charging in that vicinity are too localized to produce significant effects that result in the overall irradiation response. Thus, the displacement damage is considered as the average effects, described by volumetric or areal defect concentration. However, in ultra-small devices, the effect of a single event can be enhanced since it may results by both the along-path displacement damage and the ionization damage. Indirectly the ionization enhances the TMR values due to the improvement of the MgO crystal structure. On the other hand, the ionization from charged protons is responsible for the deterioration of the MTJ performance. The Neon irradiation result also demonstrates that the PMTJ devices can tolerate significant displacement damages. The conclusion from the results of these experiments is that STT-MTJ with perpendicular magnetic anisotropy is a promising candidate for use in these environments as summarized in the **Table 4.8** below.

Table 4.8 Radiation Hardness evaluation of STT-MTJ with perpendicular magnetic anisotropy

Radiation source and energy	Total Fluence	Radiation effects on STT-MTJ performance		
		Switching behavior	State retention	TMR
10 keV x-ray	1Mrad (Si)	No effects	No effects	Increased TMR%.
2 MeV Neon	$1 \times 10^{12} / \text{cm}^2$	No effects	No effects	Reduced TMR in sub-100nm devices
2 MeV Proton	$1 \times 10^{12} / \text{cm}^2$	A 60nm device failed to switch once during 100 cycles test	Change of pre-set state and unstable behavior for 60 nm devices	No effects

CHAPTER 5. L1₀ MnAl system

5.1 Introduction

In recent years, the ion irradiation has been widely applied to modify magnetic properties in thin films or superlattices[85,142-145]. Particularly, it has been shown that the He ion irradiation can induce the chemical ordering of the L1₀ phase in FePt films[85,144], for which irradiation-induced ordering likely takes place in the vicinity of an ordered crystal structure. It has been suggest that the heating from the large beam current act as rapid thermal anneal to assist the crystallization of the partially ordered FePt with chemical ordering $S \sim 0.4$ [144], results in the improvement of the chemical ordering and the coercivity in L1₀ FePt films.

In this chapter, I examine the effect of 2 MeV proton (H⁺) beam on highly ordered L1₀ MnAl films ($S \sim 0.97$). MnAl films are deposited by a bias target ion beam deposition technique, and the high chemical ordering is obtained through the optimization of the post annealing conditions. The effects of thermal annealing and displacement damage induced by the protons are discussed. Magneto-transport techniques are also employed to study the change in the magnetic behaviors caused by proton irradiation.

5.2 Proton irradiation

Samples are irradiated with 2 MeV protons at the tandem Van de Graaf accelerator at Auburn University. The energy has been selected so that particles would traverse the entire sample without any significant losses of the kinetic energy, thereby creating a uniform profile of the defects that are mainly vacancies, interstitials and Frenkel pairs. An initial fluence (Φ) of 1×10^{14} H⁺/cm² is used. Details of the irradiation

process and the total fluences are listed in **Table 5.1**. The magnetic and transport properties are characterized as a function of the fluence.

Table 5.1 Irradiation procedures and the total fluence.

Irradiation*	Fluence (H^+/cm^2)	Total fluence (H^+/cm^2)
1	1×10^{14}	1×10^{14}
2	9×10^{14}	1×10^{15}
3	1×10^{15}	2×10^{15}

* The same set of samples was used for the characterization and the consecutive irradiation.

5.3 Structural Characterization

5.3.1 Recovery of Chemical Ordering

An important parameter extracted from the XRD scan is the chemical ordering parameter S , which describes the perfection of the alternating layers of Mn and Al layers in the $L1_0$ structure. The S value of 1 for perfect chemical ordering occurs when all the Mn atoms are in their own positions at the corners (0,0,0) of the tetragonal structure and all Al atoms are in the body center ($\frac{1}{2}, \frac{1}{2}, \frac{1}{2}$). The S value of 0 represents an entirely random distribution of Mn and Al atoms on the lattice sites. Experimentally, the values of S can be estimated by comparing the intensities of (001) and (002) diffraction peaks of $L1_0$ MnAl.

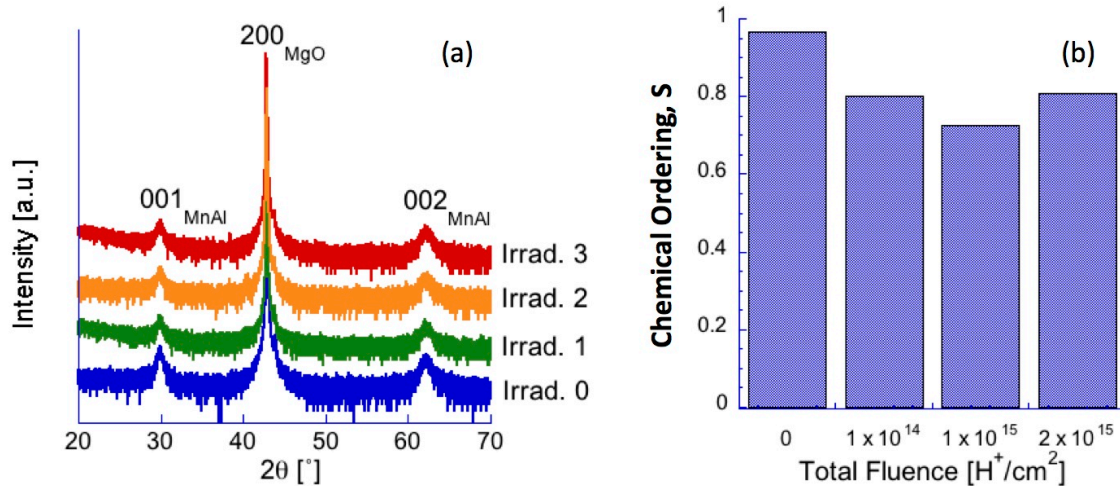


Figure 5.1 (a) XRD spectra of a 30 nm thick MnAl film for different irradiation fluences; (b) Chemical ordering as a function of total fluence (TF).

Figure 5.1a shows XRD spectra taken from the same sample throughout the irradiation process. The chemical ordering is extracted and plotted in Figure 5.1b. The S value of the pre-irradiation sample is ~ 0.97 , indicating a very high chemical ordering for MnAl films as the result of the post-deposition annealing. S is reduced to ~ 0.8 after the irradiation with a fluence of $1 \times 10^{14} H^+/cm^2$, and further down to ~ 0.72 when the fluence increased to $1 \times 10^{15} /cm^2$. After the third irradiation, the change in the chemical ordering reverses and S becomes ~ 0.81 . **Table 5.2** summarizes the peak position and the FWHM (full width half maximum) of the (001) and (002) peaks from the MnAl films in addition to the chemical ordering parameter, respectively. The positions of these two peaks do not show significant changes during the irradiation process. On the other hand, the FWHM increases and reaches a maximum after the second irradiation with the total fluence of $1 \times 10^{15} H^+/cm^2$. At the final fluence of $2 \times 10^{15} H^+/cm^2$, the FWHM is slightly reduced for both the (001) and (002) peaks.

Table 5.2 Chemical ordering (S) and peak parameters of (001) and (002) extracted from XRD spectra of MnAl thin films

Total fluence (H^+/cm^2)	S	(001)		(002)	
		2θ	FWHM	2θ	FWHM
0	0.97	$29.932 \pm 0.004^\circ$	$0.715 \pm 0.004^\circ$	$62.241 \pm 0.010^\circ$	$1.317 \pm 0.021^\circ$
1×10^{14}	0.80	$29.932 \pm 0.004^\circ$	$0.715 \pm 0.009^\circ$	$62.242 \pm 0.009^\circ$	$1.373 \pm 0.020^\circ$
1×10^{15}	0.73	$29.935 \pm 0.008^\circ$	$0.743 \pm 0.017^\circ$	$62.253 \pm 0.015^\circ$	$1.506 \pm 0.032^\circ$
2×10^{15}	0.81	$29.932 \pm 0.007^\circ$	$0.731 \pm 0.007^\circ$	$62.240 \pm 0.009^\circ$	$1.353 \pm 0.021^\circ$

Among other things, the proton irradiation can induce displacement damage, which causes atoms to be moved from their original positions. Protons with the energy used here primarily create small defects such as vacancies and interstitials, although a small proportion of defect clusters and cascades occur as well. In many cases the induced defect concentration, c is related to the particle fluence Φ by [146]

$$c = \Phi BA(NIEL) \quad 5-1$$

where, $NIEL$ is the nonionizing energy loss, the parameter B depends on the target material density and the displacement threshold energy of target atoms, and A represents the fraction of displaced atoms that do not recombine immediately following irradiation. The units of c are typically “displacements per target-material atom”, or dpa . As can be seen in Eq. 5-1, the increase of particles fluence results in increasing defect density.

The energetic particles introduce the disordering by forming defects to the crystalline system, which results a broadening of the x-ray diffraction peaks. In the present case the FWHM of the (001) MnAl peak is about 0.7° prior to irradiation. This is

larger than the $\sim 0.287^\circ$ expected for a perfect film,[147] due in part to the larger-scale defects such as the mosaicity, the microstrain and the crystallite size. Further broadening, as can be seen in **Table 5.2**, is caused by the introduction of crystal defects such as dislocations and grain boundaries, which can be associated with the displacement damage caused by the proton-induced cascade events.

At the total fluence of $2 \times 10^{15} \text{ H}^+/\text{cm}^2$, the effect of displacement damage appears to be overwhelmed by the ordering enhancement in $L1_0$ MnAl, which is observed in the changes of the S as well as the FWHM values. As a result, we observe the partial recovery of chemical ordering of MnAl at the highest proton fluence without any intentional heating of the sample. The initial decrease and subsequent increase in the chemical ordering must be a result of the competing effects of the radiation-induced disorder and the post-irradiation annealing. In other words, the accumulation of defects in MnAl films is more complicated than would be suggested by Eqn. 5-1 because the recombination factor A appears to be a function of fluence.

5.3.2 Displacement damage and inter-diffusion

For multilayer structures, the ion irradiation also causes the intermixing of adjacent layers, which results in an increase in the interface roughness.[148] Secondary ion mass spectroscopy (SIMS) is performed to investigate the effect of irradiation on the composition profiles in the samples. The measurements were stopped before reaching the MgO substrates. Based on the intensity of Ta ions, I have identified the interface between Ta (capping layer) and MnAl as illustrated in **Figure 5.2**. Even prior to the irradiation, there is a noticeable intermixing of the Ta layer and the MnAl layer, which is likely due to the interdiffusion during the post-deposition annealing. After the proton

exposure, the Mg content, which is from the MgO substrate in the MnAl, is significantly increased in comparison to that of Ta.

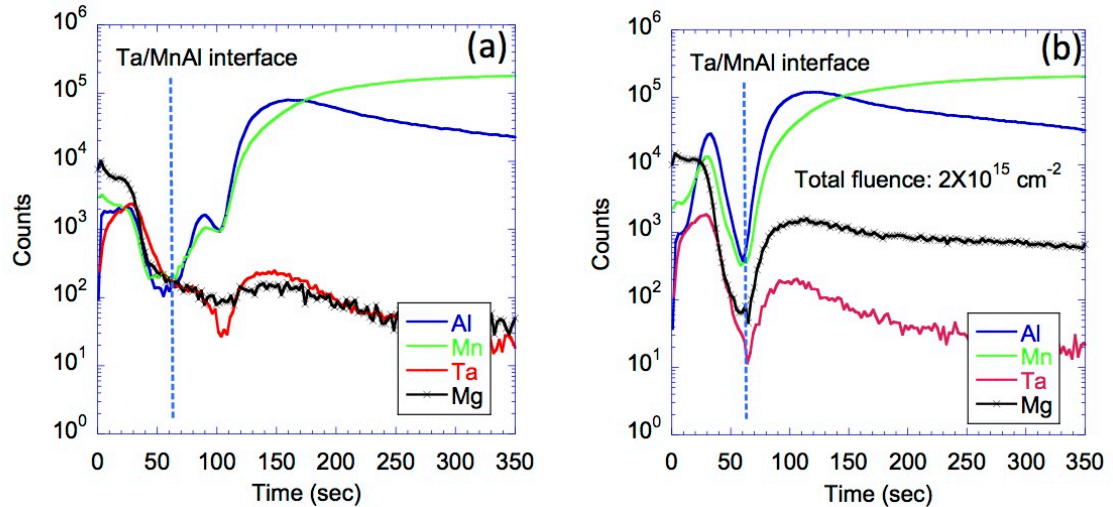


Figure 5.2 SIMS results of Ta (5 nm) /MnAl (30 nm) /MgO (substrate) **(a)** before the irradiation; **(b)** after the irradiation with 2 MeV proton with the total fluence of $2 \times 10^{15} \text{ cm}^{-2}$ (right). The dashed lines correspond to the approximation positions of the Ta/MnAl interface.

To elucidate the effect of the displacement damage on the compositional distribution of the film, the range of the protons in the test structures is simulated using the program Stopping and Range of Ions in Matter (SRIM). The blue line in **Figure 5.3a** represents the active region i.e. MnAl, the proton implantation peak is $28.5 \mu\text{m}$ deep into the MgO substrate. **Figure 5.3b** shows the profile of the induced defects versus the depth, and it reveals that the defects within the Ta/MnAl layers do not straggle far from the line of incidence. The rate of energy loss within the active region of the device is found to be nearly constant. Hence, the expected outcome of the irradiations is a nearly uniform dusting of small displacement defects throughout.

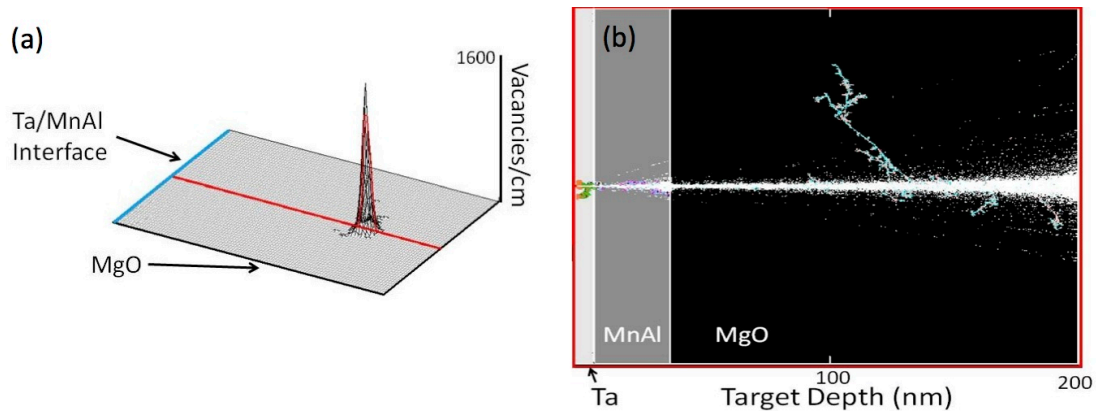


Figure 5.3 (a) 3-D simulation of 2 MeV proton range in Ta/MnAl/MgO test structure. The average range is 28.5 μm . (b) Depth profile of induced defects showing the Ta/MnAl and MnAl/MgO interface (Courtesy of B.Weaver)

A sample recoil spectrum of manganese and aluminum are also shown in **Figure 5.4**. The recoil distributions vs. Depths show how the target atoms are knocked out of their lattice sites creating displacement defects (interstitials and vacancies). The y-coordinate unit is $(\text{Atoms}/\text{cm}^3)/(\text{Atoms}/\text{cm}^2)$. If one multiplies the recoil distribution with the irradiation dose (ion/cm^2), the end result plot is defect concentration c , as in Eqn.5-1, vs Depths. Here with known target atom density (atoms/cm^3), dpa can also be determined.

The zoomed-in views in the inset shows that both recoiled Mn and Al intermix at the Ta/MnAl interface to a depth of about 3 nm. The simulation result suggests that the displacement damage from 2 MeV protons can cause the rougher interface by leaving stable defects at the interface. However, atoms can also move across the Ta/MnAl

interface by the thermally assisted diffusion as seen in virgin sample after RTA. Both effects can be responsible for the increase of interface roughness.

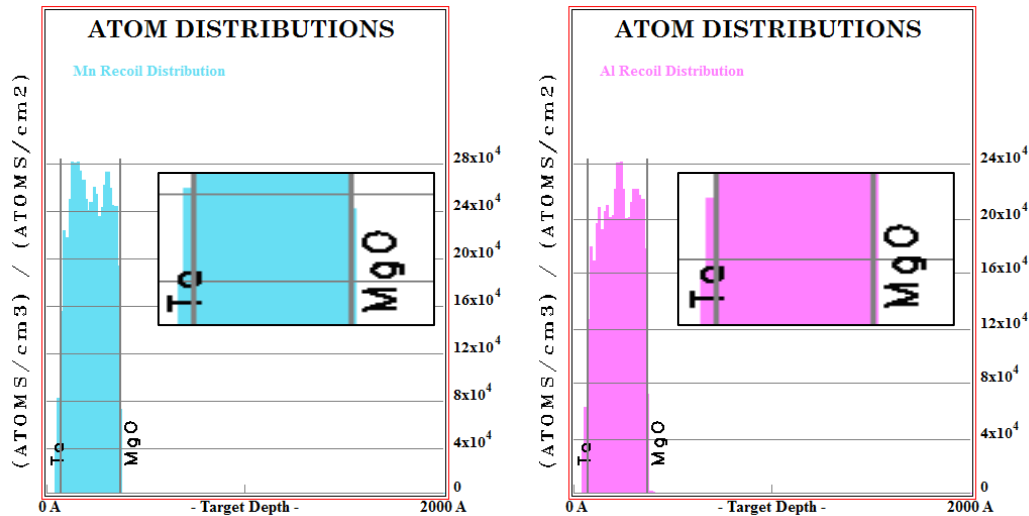


Figure 5.4 Recoil distributions of Mn and Al showing intermixing with the Ta and MgO layers (Courtesy of B.Weaver)

From the simulation, the majority of the dislocated atoms occur in the MgO substrate. While a significantly smaller amount of defects arise at the magnetically active layer, these displacement atoms do not appear to deviate from the proton beam. It indicates that the damages are likely localized that is difficult to be characterized. It is worth noting that SRIM simulation only considers the elastic collisions between atoms, the inelastic scattering in which attributed to ionization is neglected. Hence, the roles of substitution defects cannot be determined here.

5.4 Postmortem magnetic Properties

Figure 5.5a shows the normalized out-of-plane magnetization curves, by a polar Magneto-Optic Kerr Effect loop(MOKE), for the same sample for pre- and post-irradiation. The coercivity in the virgin sample is $\sim 0.08\text{T}$, and is increased to $\sim 0.11\text{T}$ in

the post-irradiated sample. **Figure 5.5b** shows the saturation moment (M_S) of a ~ 30 nm MnAl film as a function of proton fluence. The saturation moment M_S of MnAl prior to irradiation is ~ 300 emu/cm³. The value of M_S reaches a minimum at a fluence of 1×10^{14} H⁺/cm². The further H⁺ exposure results monotonous increase in M_S that reaches ~ 380 emu/cm³ at the total fluence of 2×10^{15} H⁺/cm². This represents a ~ 27 % increase in the total magnetic moment as the result of the ion irradiation.

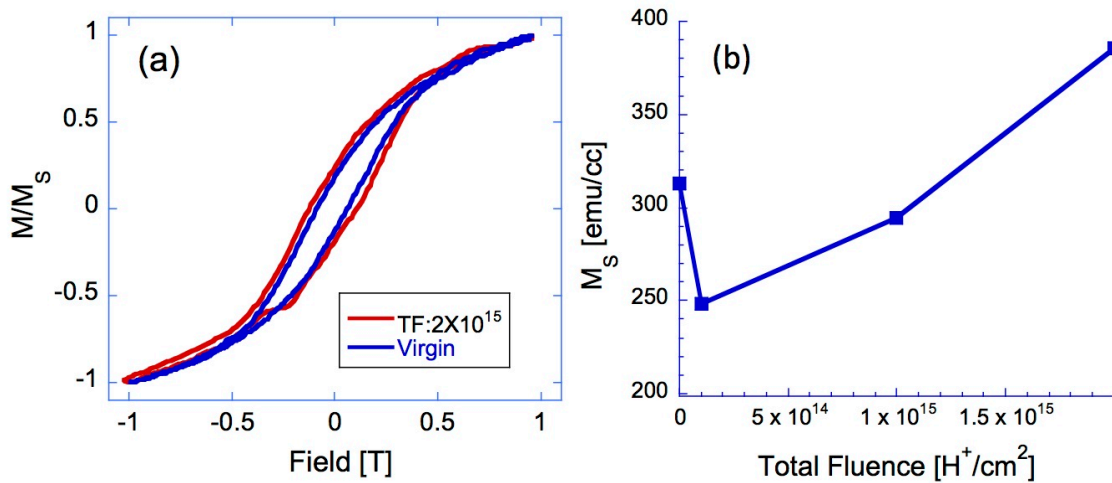


Figure 5.5 (a) Perpendicular normalized magnetization curves of the MnAl film for pre- and post-irradiation measured at room temperature by MOKE. **(b)** Saturation moment (M_S) as a function of total fluence (TF).

The MFM are performed on the unpattern samples after demagnetizing as shown in **Figure 5.6**. The bright and dark contrasts represent the opposite magnetizations i.e. up and down in this PMA material. The topographic difference based on the AFM images taken with MFM images (not shown here) is small, indicating no surface damage to the film after the final irradiation. The average domain size can be acquired simply by divided total area by the total number of domains. In the magnetic materials with Bloch domain wall, the size of the domain is determined by the competition of magnetoelastic energy and domain wall energy. In equilibrium state, the domain size is proportional to

$\sqrt{A/K_U}$ where A is exchange stiffness constant and K_U is perpendicular anisotropy respectively. The magnetic domain morphologies of virgin and irradiation sample are similar. The average domain size is $\sim 0.021 \mu\text{m}^2$ in the pre-rad sample and $\sim 0.018 \mu\text{m}^2$ after the proton exposure. It is clear that the magnetization reversal is governed by the domain wall process rather than the coherent rotation since the coercive field ($H_C \sim 0.1 \text{ T}$) is much smaller than anisotropy field H_K of $\sim 2 \text{ T}$.

The enhancement of coercivity (from 0.08 T to 0.11 T) is likely the attribution of domain wall pinning from defects induced by the irradiation. Despite the 27% change in saturation moment, the magnetization dynamic as well as domain structure remain relatively unchanged thanks to the high perpendicular anisotropy. However, the results may imply that the effect of the displacement damage occurs on the local atomic scale rather than the collective properties such as the coercivity and the domain structure.

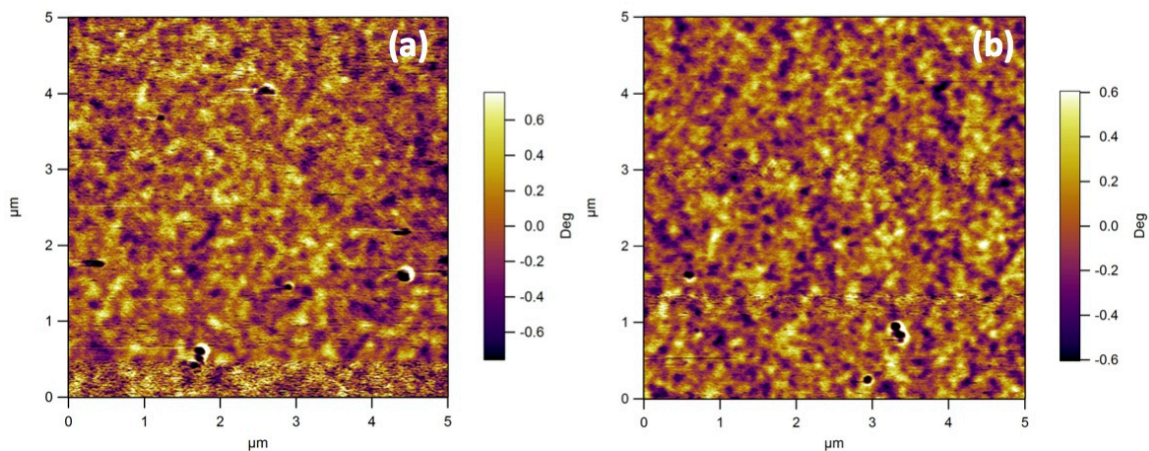


Figure 5.6 Magnetic force microscope images of (a) Virgin and (b) after the total fluence $2 \times 10^{15} \text{ H}^+/\text{cm}^2$

The correlation between the chemical ordering and the total magnetic moment can be explained by the coupling of Mn atoms at different lattice points in BCT structure. The

perfect chemical ordering ($S=I$) occurs where Mn and Al atoms sit in their own position layer by layer. When that the Mn atom switch to the positions originally occupied by Al, it will antiferromagnetically coupled with neighboring Mn atoms on their original positions.[39] Consequently, both the chemical ordering and magnetization are reduced.

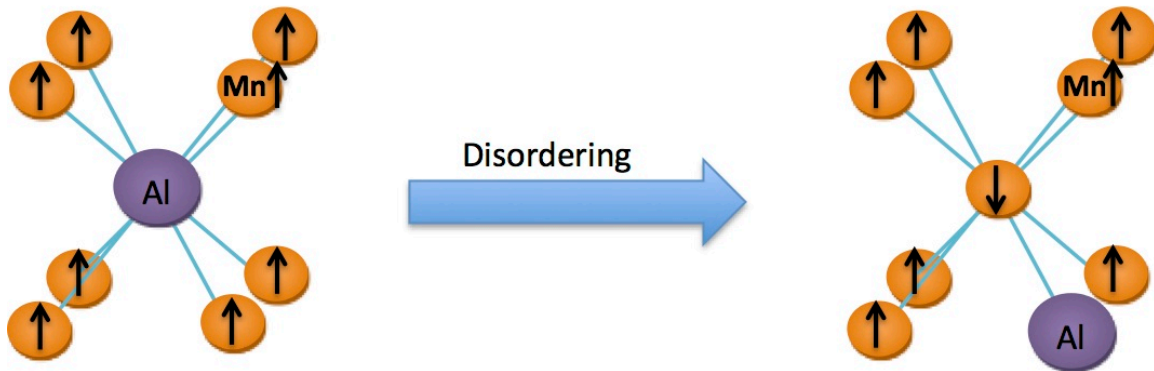


Figure 5.7 Illustration of the disordering process in the BCT structure

It is also necessary to point out that the saturation moment after the last irradiation becomes significantly larger than that of virgin sample, and the chemical ordering in the MnAl film is partially recovered. Thus, the increase in the magnetization cannot be explained by the recovery of the chemical ordering alone. It suggests that there are additional contributions to the magnetic moments as the results of the displacement damage and the thermal annealing in $L1_0$ MnAl. One can speculate that the defects introduced during the irradiation are ferromagnetic. A more reasonable explanation could be the relaxation of the epitaxial strain caused by the increase in the density of defects and grain boundaries. It has been shown that M_S in MnAl was strongly dependent on the in-plane strain, as predicted.[149,150] The irradiation process causes the peak broadening as aforementioned that may lead to the relaxation of in-plane strain due to the large lattice mismatch between MnAl and MgO ($\sim 6.7\%$). Thus the magnetic moment is

enhanced despite only a partial recovery of the chemical ordering. The change in the local magnetic properties also cannot be ruled out.

5.5 Transport properties

5.5.1 Anomalous Hall Resistance (R_{XY}) and Magnetoresistance (R_{XX})

The Hall effect in MnAl Hall bar devices is measured in ETO mode at 300K and 50K with a constant bias current of 2 mA along the length of the Hall bar device. The magnetic field H is applied perpendicular to device, and swept from -3 T to 3 T and back to -3 T while the Hall resistance (R_{xy}) is measured every 0.1 T step. The room temperature anomalous Hall resistances (R_{xy}) of the MnAl Hall bar devices are shown in **Figure 5.8**.

Figure 5.8.

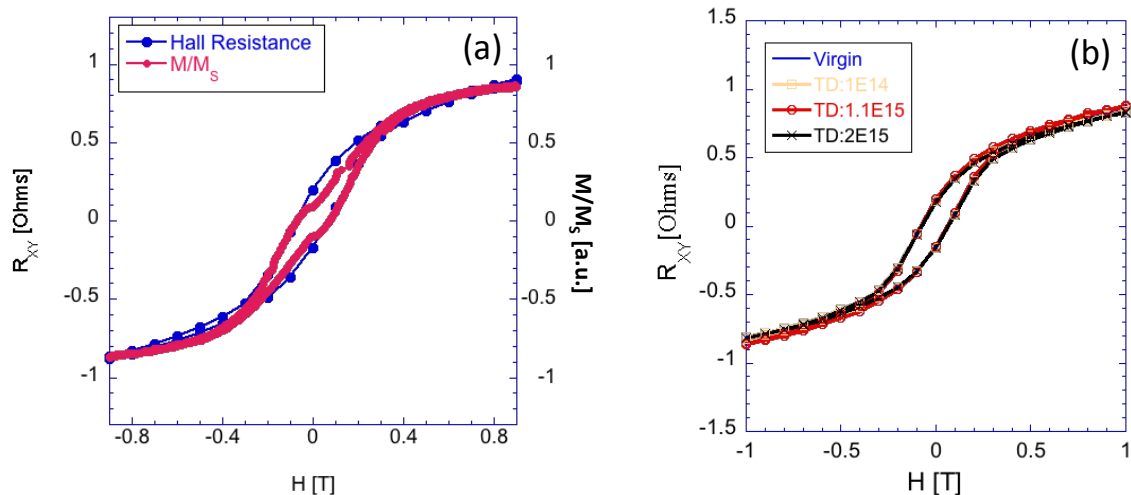


Figure 5.8 (a) Hall resistance (R_{xy}) mimics the out-of-plane magnetization loop nicely **(b)** Hall resistance vs. Magnetic field (H) measured as a function of total fluence at 300 K. The same Hall bar device was measured after each exposure to the proton beam.

Despite the appreciable changes in chemical ordering and magnetization, the irradiation process did not significantly modify R_{xy} . The coercivity (H_C) extracted from R_{xy} is ~ 0.05 kOe, which is also not affected by the increase in proton fluence. A small increase in R_{xy} for the total fluence of 1×10^{15} H^+/cm^2 is observed but may be caused by the artificial effect introduced during the wire bonding process required for measurement in the PPMS system.

The magneto-resistance (R_{xx}) is measured on the same Hall device through the irradiation procedures. Magneto-resistance as a function of total fluence of protons is shown in **Figure 5.9**. At room temperature, the resistance does not return to the same value at $-H_{\text{max}}$ in two sets of data that is likely caused by the thermal drift. The temperature of the sample rises slightly thanks to the Joule heating from the excitation current. At 50 K, the thermal drift is eliminated. The overall MR ratio is small for the MnAl Hall device, and remains unchanged as the total fluence is increased. The incremental fluence results in a very small increase in the resistance of the Hall devices (less than 0.005%) that can be attributed to the change in the defect concentration induced by the proton beams. It can be concluded that the magneto-resistance of the film is very resilient to proton irradiation despite the changes in the microstructure and the chemical ordering of MnAl.

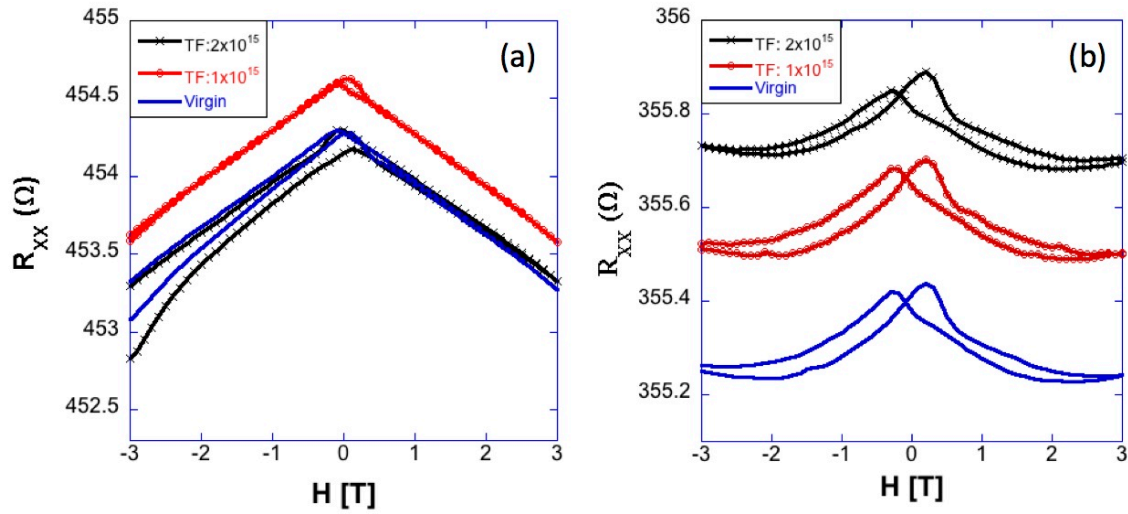


Figure 5.9 Magneto-resistance of Hall device: sample structure [Ta (5 nm) /MnAl (30 nm) /MgO(substrate)] as a function of total fluence(TF) of proton irradiation. **(a)** at 300K and **(b)** at 50K.

The Hall resistance (R_{xy}) can be defined using the formula:[106]

$$R_{xy} = R_0 H_z + R_s M_z \quad 5-2$$

Where $R_0 H_z$ is the term from ordinary Hall effect, and $R_s M_z$ (M_z : the magnetization along the magnetizing field) represents the resistance from the anomalous Hall effect (AHE) contribution due to the spin orbit coupling in ferromagnets. R_s is the anomalous Hall coefficient, which is dependent on the longitudinal resistivity (ρ_{xx}). As seen in **Figure 5.8a**, R_H clearly follows the magnetization loop indicating the domination of AHE over the ordinary Hall effect term. Therefore, the Hall resistivity can be determined simply by the relation [106,112]

$$\rho_H = -\rho_{xy} = R_{XY} \cdot t \quad 5-3$$

where t is the thickness of the film, ρ_{xy} is the transverse resistivity and ρ_H is the Hall

resistivity.

To gain insight contribution to the AHE, the scaling relationship, as shown in Eqn 5-4, is usually employed where the first and the second term are associated with skew scattering and the side-jump mechanism are associated respectively[106]. R_{XX} and R_{XY} were extracted from the range of magnetic field from 2 T to 3 T, where the magnetic moment become saturated, during sweep up process in order to minimize the effect of the heating from bias current (which appear in TF: 2×10^{15} sample during H field sweep down).

$$\rho_{xy} = a\rho_{xx} + b\rho_{xx}^2 \quad 5-4$$

The coefficient a and b can be extracted from plotting $\frac{\rho_{xy}}{\rho_{xx}}$ vs. ρ_{xx} followed by linear fitting the data as shown in **Figure 5.10a**. The skew scattering and the side jump coefficient parameters are shown as a function of total dose in **Figure 5.10b**. The skew scattering and the side jump coefficient behave in respond to increasing irradiation fluence as follows. The values of $|a|$ and $|b|$ reduce after the total fluence $1 \times 10^{15} \text{ H}^+/\text{cm}^2$ then recover after the final irradiation with total fluence of $2 \times 10^{15} \text{ H}^+/\text{cm}^2$. Even though the values of both $|a|$ and $|b|$ increase after the final irradiation, it is worth noting that $|b|$ exceeds its original value of the virgin sample.

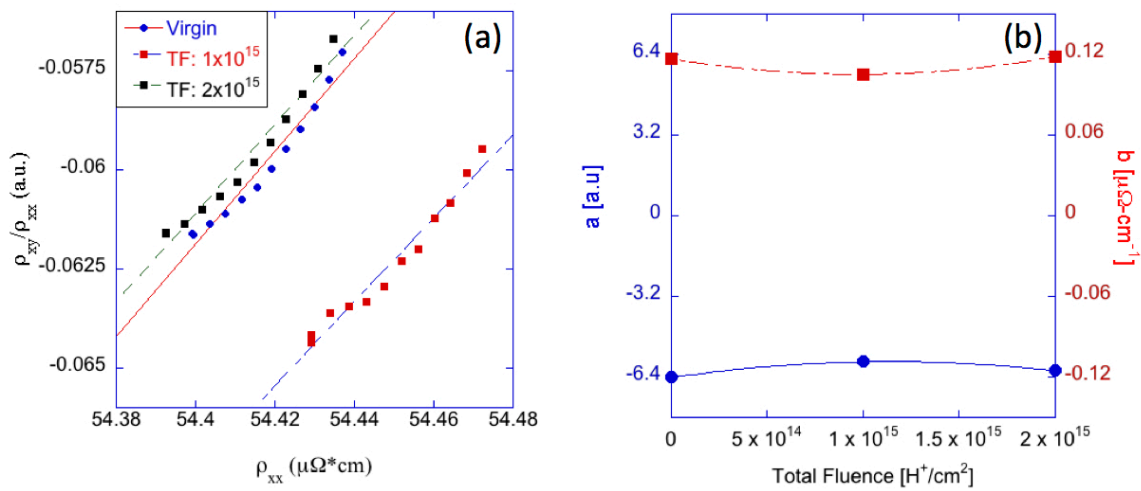


Figure 5.10 (a) $\frac{\rho_{xx}}{\rho_{xy}}$ vs ρ_{xx} plot of various total fluence show linear relationship following the scaling equation of AHE nicely. **(b)** The evolution of skew and side-jump scattering coefficient as a function of total fluence.

The increase in coefficient a and the decrease in coefficient b after the total fluence of $1 \times 10^{15} \text{ H}^+/\text{cm}^2$ imply the enhancement of skew scattering while the side jump is suppressed. The result resembles the occurrence observed in Ni films with the films thickness decreasing from 100nm to 10 nm[151] and Co/Pd multilayer [152] where it has been attributed to surface scattering. By considering skew scattering as the sole mechanism contributed to the AHE, Gerber[151]found that the skew scattering coefficient a increased with the film thickness decreased and even changed its sign in a very thin samples($\sim 10\text{nm}$). The phenomenon was attributed to the competition between the surface and the bulk scattering that possessed opposite polarities. The electrons scattering from defects near the surface were shown to induce spin flip and reduce spin polarization[153] in which could contribute to the change in the anomalous Hall effect. When the thickness is drastically reduced, the surface scattering becomes the major

contribution that overwhelms the bulk scattering so that one can observe the increase or even the sign reversal of the overall skew scattering coefficient or vice versa.

As discussed earlier, the 2 MeV proton beam rastering all over film surface would likely create uniform displacement defects throughout the depth of the magnetic active layer due to the large kinetic energy. With the film thickness of ~ 30 nm, the surface scattering should be relatively small. The change in the scattering coefficients should be attributed to the increase in defects and the modification of the magnetic properties of MnAl, which are observed in the changes in chemical ordering and magnetization as the result of the proton exposure. After the final proton exposure, the a and b coefficient values restore themselves close to those of the virgin sample in accordance with the recovery of the chemical ordering, implying the strong dependence of anomalous Hall effect with the film structure rather than the surface scattering contribution.

Even though the changes in the microstructure local magnetic properties are appreciable during the irradiation process, the AHE at room temperature is very robust that is not affected significantly by the total fluence of proton beam. The Hall resistivity is resilient providing change less than $0.15 \mu\Omega\text{-cm}$ upto total fluence of $2 \times 10^{15} \text{ H}^+/\text{cm}^2$, representing the variation of less than 0.12% of the Hall resistivity at 3 T. The unaffected coercivity in postmortem samples indicates that the proton beam, despite the introduction of the defects, does not modify the perpendicular magnetic anisotropy. It appears that the magneto-transport properties of $L1_0$ MnAl are very resilient to the displacement damage effects caused by 2 MeV proton irradiation. This is a highly desirable property for applications in harsh radiation environments.[6]

5.5.2 Electrical Resistivity

Figure 5.11 shows the temperature dependence of the resistivity of a ~ 30 nm MnAl film before and after the proton exposure. The resistivity of MnAl is $\sim 8.6 \times 10^{-5} \Omega \cdot \text{cm}$ at room temperature which is about an order of magnitude lower than that of other MnAl films having similar thickness.[154] At room temperature, the irradiation increases the resistivity only slightly, whereas at lower temperatures, the resistance ratio (RR) for the virgin and irradiated samples diverges. For the unirradiated MnAl Hall bar device, the resistance decreases with decreasing temperature and reaches its residual resistance below 20 K, as expected for a normal metal. For the irradiated sample, a resistance increase is observed at the temperature below $\sim 23\text{K}$ (estimated by dR/dT), signaling a metal-insulator transition.

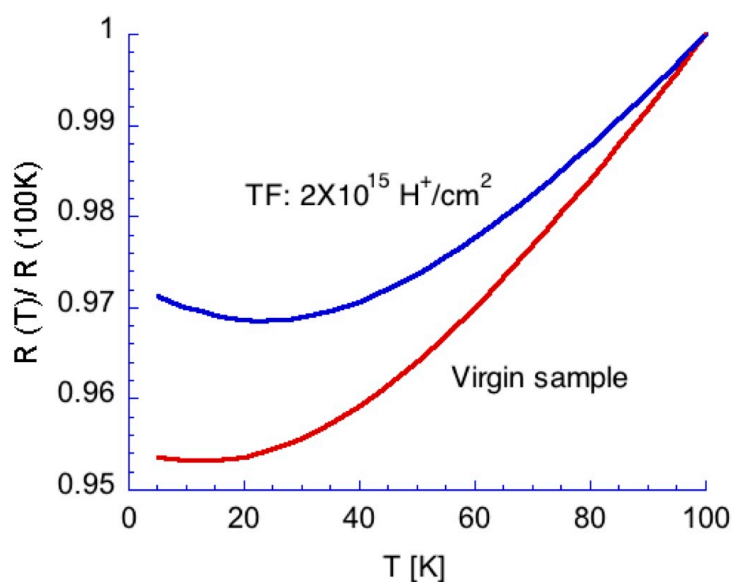


Figure 5.11 Temperature dependence of the normalized resistances for virgin and irradiated MnAl Hall bar device.

The increase of defects and intermixing results in the enhanced electron scattering, which lead to the slight increase in resistivity. The metal-insulator transition that occurs at low temperatures in the irradiated sample is likely due to the weak localization associated with the disorders.[114] The coherence length in MnAl is likely reduced due to the introduction of the disorder caused by the point defects and the rough interfaces, which resulted in the enhanced backscattering for electrons at low temperatures. To further investigate the origin of the upturn at ~ 23 K, MR measurement is also performed for high magnetic field (up to 7 T) sweeping at 2K as shown in **Figure 5.12**.

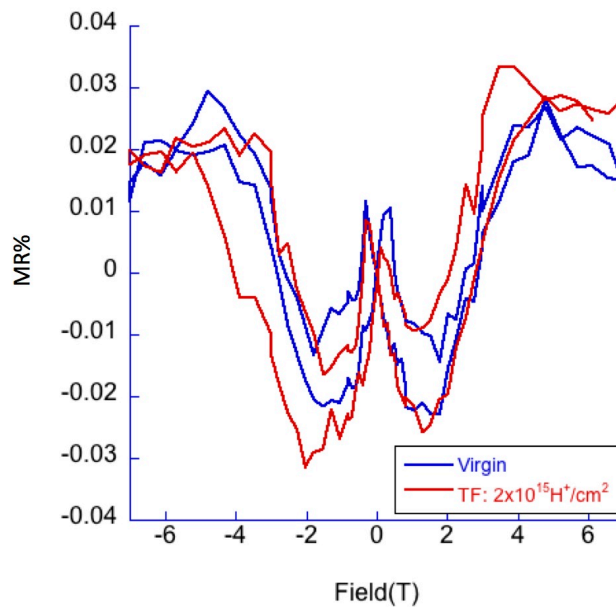


Figure 5.12 MR% of irradiated and virgin Hallbar measured at 2K.

The MRs of virgin and irradiated samples exhibits a very similar behavior. In the low-field regime ($H < 2$ T), the small negative MR is the characteristic features of the weak localization since the magnetic field suppresses the coherent interference for the

charge carriers[114]. The positive MR that occurred around H_C indicates the existence of an additional scattering mechanism related to the magnetic domain state, with the maximum scattering in the multidomain state at H_C . The maximal MR near H_C is the scattering of electrons by domain walls (DWs) as previously reported in the literatures[113,155]. The rapid increase of MR at high magnetic fields is due to the electron-electron scattering that overwhelms the effect of the weak localization at low magnetic fields.

5.6 Summary

In conclusion, we performed 2 MeV proton irradiation experiments on highly ordered $L1_0$ MnAl epitaxial films grown on (100) MgO substrates. The recovery of the chemical ordering at the final total fluence has been observed despite the displacement damage to the thin film. The transport and magneto-transport properties are not significantly affected by the high energy proton beam. This suggests that highly ordered $L1_0$ MnAl is intrinsically ‘radiation hard’ and is thus very promising for use in harsh radiation environments.

CHAPTER 6. Amorphous Rare earth—Transition alloys

6.1 Introduction

This chapter investigates the effect of the 2 MeV proton ions on magnetic and magneto-transport properties of amorphous ferrimagnets. Studies on the displacement damages in these systems are compelling since the amorphous systems themselves have only medium and short range orderings prior to the irradiation. Amorphous rare earth transition metal (*a*-RE-TM) films exhibit unusual magnetic anisotropy despite the absence of the crystalline anisotropy. Recent studies have discovered some unusual magnetic properties in *a*-RE-TM films: large perpendicular magnetic anisotropy (PMA) ($\sim 10^6$ erg/cm³)[156] in as-grown films which can be significantly enhanced in patterned strips[157], and an ultra-fast magnetization reversal (\sim picoseconds) induced by the photons[158,159]. The results could potentially enable spin logic devices with 1,000 GHz clock speed, several orders of magnitude faster than that of the devices based on spin wave logic concept. These functional amorphous films are appealing for practical applications and can be achieved without the need for epitaxial growth.

The 2 MeV proton ions are employed to investigate the mechanism of PMA. The proton irradiation, known for creating both displacement damages and ionization damages, can alter the microstructure. The structural anisotropy in thin films can be either enhanced or relaxed depending on factors such as variation of film composition[160], mechanical stress[157] and annealing conditions[161]. Magneto-transport properties are used extensively with the focus on the changes caused by the proton irradiation. The Stopping and Range of Ions in Matters (SRIM) simulation is used to predict microstructural change during proton irradiation.

6.2 Pre-rad characterization

6.2.1 Structural and compositional determination

Figure 6.1a shows a cross-sectional TEM image of a ~35 nm thick TbFeCo film. No evidence for the crystalline structure is observed in this bright field contrast image. **Figure 6.1b** shows a high-resolution TEM image in TbFeCo region that also reveals no nano-crystallites. Only a single ring pattern is presented in the fast Fourier transform (FFT) image due to the lack of long range ordering. In addition, XRD scans show that there are no diffraction peaks from TbFeCo films with different thickness (not shown here). Both TEM and XRD confirm the amorphous nature of the film deposited at the ambient temperature, which is consistent with the previous reports on RE-TM films[49,50].

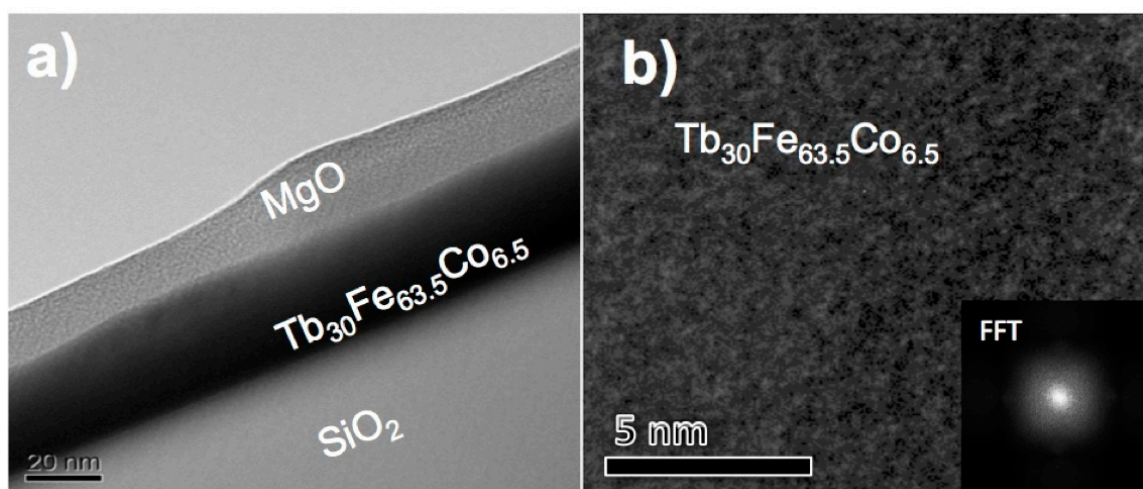


Figure 6.1 (a) Bright field TEM image of a 35 nm TbFeCo film deposited on SiO₂/Si. A 15 nm MgO layer was used to cap the film; **(b)** HRTEM image of the TbFeCo film. The inset is a FFT pattern of the image. (Courtesy of M. Ding).

6.2.2 Magnetic properties

Figure 6.2 shows the hysteresis loops of a 35 nm thick TbFeCo film. The saturation moment (M_s) is ~ 100 emu/cc. The small saturation moment is due to the ferrimagnetism of amorphous RE-TM alloys. The Co and Fe ions have a small single ion anisotropy and the Tb ions have large anisotropy. The large TM-TM ferromagnetic interaction aligns the magnetic moments from Fe and Co ions, while the large anisotropy of RE ions fans the magnetic moments of Tb ions out over the opposite hemisphere. As a result, the net moment is the difference of magnetic moment between Tb and Co/Fe. The magnetization loops show that the film exhibits the uniaxial anisotropy in which the easy axis is perpendicular to the film plane. The anisotropy energy K_U can be calculated by evaluating the area enclosed between the in-plane and perpendicular hysteresis loops [162,163]. In the cases where magnetic domains switch coherently with few pinning sites, K_U can be equivalently obtained as

$$K_U = \frac{H_K M_S}{2} \quad 6-1$$

where H_K is the saturation field. Due to the high PMA and squareness of magnetization loop, H_K is the same value of the out-of-plane coercive field (H_C). This proves to be effective method to study the radiation effect on the magnetic anisotropy via transport properties in which I will describe in detail in the next section.

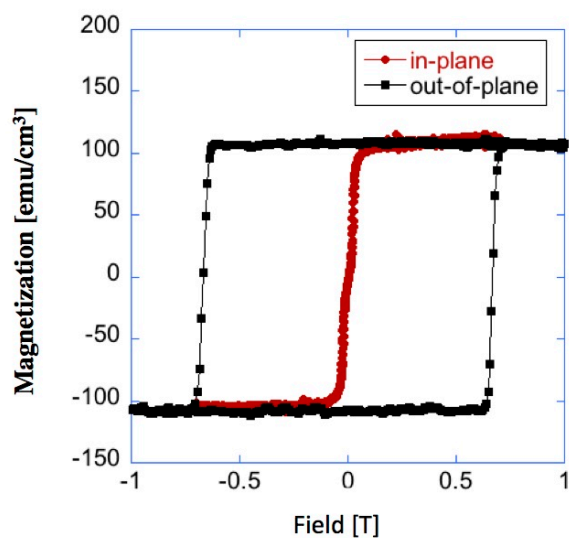


Figure 6.1 In-plane and out-of-plane hysteresis loops of virgin sample

6.2.3 Strain-induced enhancement of coercivity

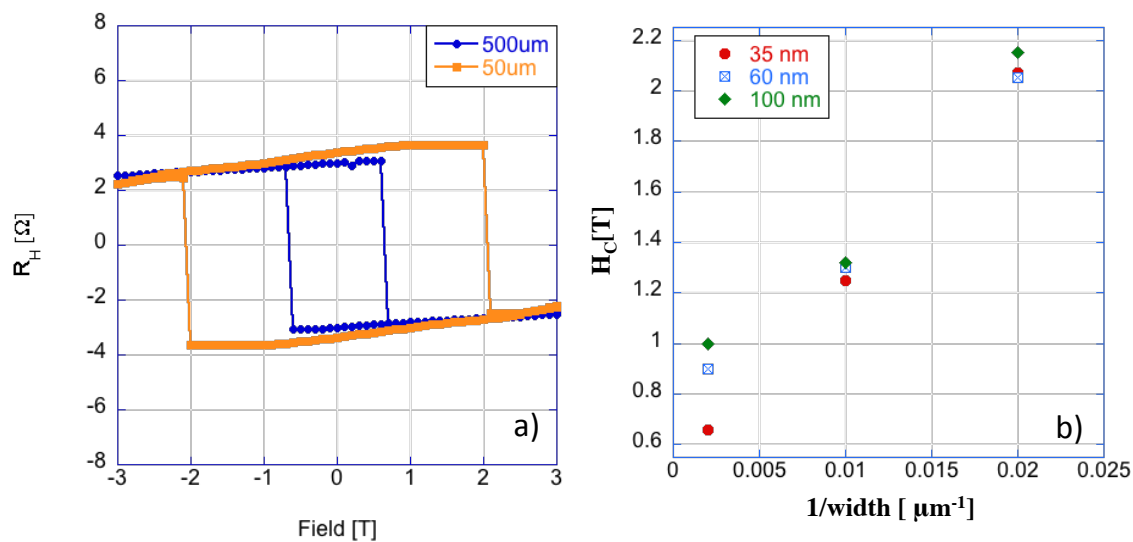


Figure 6.3 (a) Hall resistance vs. magnetic field for two Hall bar devices with the widths of 50 and 500 μm at room temperature **(b)** Coercive field vs. $1/\text{width}$ of Hall bar for TbFeCo films with various thicknesses measured at room temperature.

Hall bar devices are fabricated to characterize the magneto-transport behaviors. **Figure 6.3a** shows the Hall Resistance (R_H) as a function of an external magnetic field, which is applied perpendicularly to the film plane, for 50 and 500 μm wide Hall bars at room temperature. There is a significant difference in H_c for two different Hall bars measured via this method. The magnetic field dependence of Hall resistances for both Hall bars resembles the out-of-plane hysteresis of the sample, which is due to the dominance of the anomalous Hall resistance (R_{AHE}) over the ordinary Hall resistance (R_{OHE}). R_{AHE} is proportional to the magnetization (M) of the ferromagnet, thus it is strongly dependent to the magnetic field. Based on the relationship between R_{AHE} and M , the values of H_c are extracted as a function of the width of Hall bar. For the 500 μm wide Hall bar, H_c is 0.6 T that is consistent with the value (~ 0.66 T) measured on unpatterned film by VSM and MOKE. In contrast, H_c is increased to ~ 2.1 T when the width of the Hall bar was reduced to 50 μm , representing a three fold increase over H_c measured from both 500 μm wide Hall bar and the unpatterned film.

Figure 6.3b shows the dependence of the coercivity as a function of the reciprocal of the width of the TbCoFe Hall bar at room temperature. The linear relation deteriorates as the film thickness increases. This is due to the imperfection of fabrication known as “undercut” of the film. This effect causes the patterned features become smaller than its lithography masks. The effects is greater emphasized for the thicker films due to the non-uniform etching nature of the wet-etched process.

Coercivity enhancements in Hall bar devices have been reported with various origins such as edge roughness in which led to domain wall pinning[164], suppression of available paths for domain motion[165], and magnetization reversal mechanism[166].

Domain wall pinning and blocking are associated with the disorder or defects of thin films. Due to the amorphous nature of our samples, the coercive field enhancement is unlikely associated with the pinning effects. The MFM images reveal the similar domain structure for Hall Bar device with the size $\sim 0.1 \mu m^2$, which is significantly smaller than the width of the smallest Hall bar device here. Therefore, the change in the magnetization reversal process is also unlikely caused by the pinning of the magnetic domains.

The effects of stress and strain can also modify the perpendicular magnetic anisotropy thanks to the magnetostrictive effect [60-62]. The induced uniaxial magnetic anisotropy ΔK_U is expressed as

$$\Delta K_U = \frac{3\sigma\lambda_s}{2} \quad 6-2$$

where λ_s and σ are magnetostriction and mechanical stress of the film respectively. Due to the large magnetostriction of TbFeCo ($\sim 800-1200$ ppm), the stress-induced anisotropy can be responsible for the change in the coercivity. Various thickness films ranging from 15 – 100 nm are studied. We concluded that the film is partially relaxed from surface stress reduction during Hall bar fabrications[157]. The growth stress can be introduced during film deposition[167] and appears to be the key element for as-growth mechanical stress. The TEM study shows no evident of micro-voids that cause the tensile stress due to the attractive force between the nearest neighbor atoms across the voids, suggesting the different kind of stress is introduced during the film growth. By amorphous nature, the film should experiences compressive stress during growth—heavy element ions highly compressed until system become disorder on the substrates.

6.3 Irradiation of TbFeCo films

Following the initial characterization, samples are irradiated with 2 MeV protons at the tandem Van de Graaf accelerator at Auburn University. The energy is selected so that particles would traverse the entire sample without significant loss of energy, thereby creating a uniform profile of defect as well as eliminating the effect of proton implantation[87]. The 2-MeV proton beam is perpendicular to sample surface. The initial fluence (Φ) of $1 \times 10^{15} \text{ H}^+/\text{cm}^2$ is chosen. Following the initial irradiation, the samples are characterized then exposed to the subsequent irradiation for the total fluence of $1.9 \times 10^{15} \text{ H}^+/\text{cm}^2$. The irradiation procedure is shown in **Table 6.1**.

Table 6.1 Proton irradiation procedure on TbFeCo materials

Sample	1 st rad: Total Dose (H^+/cm^2)	2 nd rad: Total Dose (H^+/cm^2)	Total Fluence (H^+/cm^2)
7x7mm thin film	1×10^{15}	9×10^{14}	1.9×10^{15}
500 μm Hallbar	1×10^{15}	9×10^{14}	1.9×10^{15}
50 μm Hallbar	1×10^{15}	9×10^{14}	1.9×10^{15}
500nm Hallbar	1×10^{15}	9×10^{14}	1.9×10^{15}

6.3.1 Simulation of proton irradiation

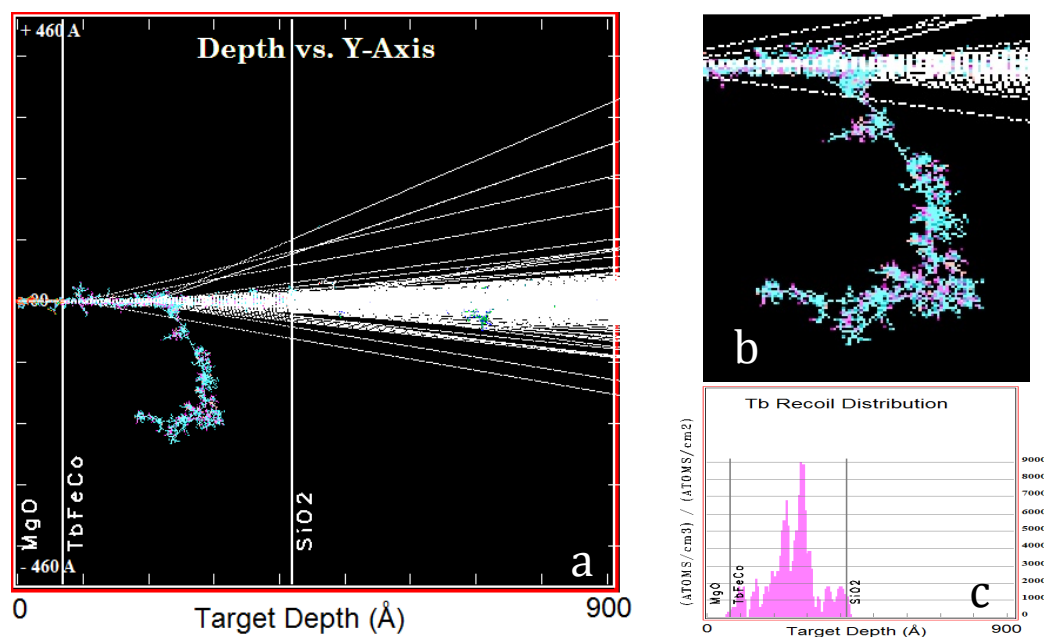


Figure 6.2 SRIM simulation results (a) depth profile of film structure reveals large cascades in TbFeCo layer (b) Zoom-in image of the large cascade (c) Tb recoil distribution is influenced by the large cascade signature (Courtesy of B.Weaver)

The Stopping and Range of Ions in Matters (SRIM) simulation is also used to study microstructural change during proton irradiation. The simulation results are shown in **Figure 6.4**. Small cascades (typically for 2 MeV proton) are created along the path of the proton beam accompanied by large cascades, which are only occurred in TbFeCo layer after total event of 4×10^5 (note that the dose is much smaller than our experimental dose $\sim 10^{15}$). The estimated cascade volume is 3645 nm^3 . Tb, Fe, and Co recoiled distributions are also influenced by these cascades. Such large cascades can leave behind voids or clusters, which may effect local composition as well as the stress of the film. To verify this assumption, the magnetic and transports properties of post-rad samples are

investigated in comparable fashions to the virgin samples in the next sessions.

6.3.2 Electric properties after proton irradiation

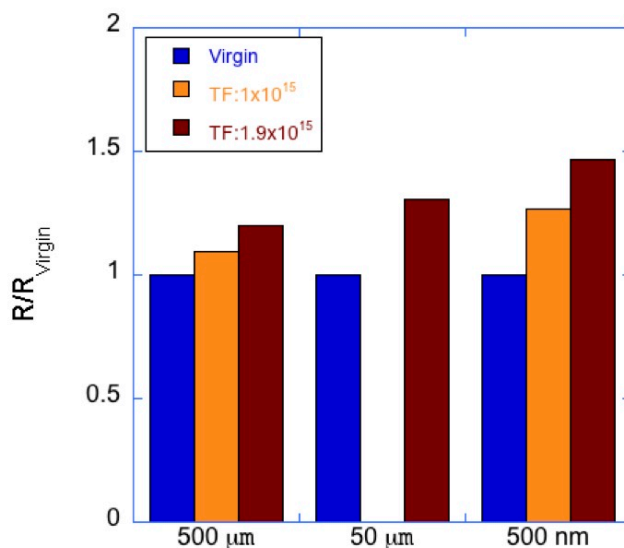


Figure 6.5 Resistance ratio of the irradiated and the virgin Hall bar at room temperature

Resistance measurement is performed at room temperature as a function of the radiation fluence. **Figure 6.5** summarizes the normalized resistance ratio to that of the virgin sample. The radiation results in the incremental increase of the electrical resistivity. As aforementioned, the creation of voids could be responsible for this change in the resistivity by increasing the scattering of electrons. It is common that the rise in resistance associated with materials becoming porous[168,169]. When the materials become more porous by the irradiation-induced defect formation, the areas for the conduction decrease while the current paths increase. Both of these changes could lead to the increase in the resistivity of material.

6.3.3 Magnetic properties after proton irradiation

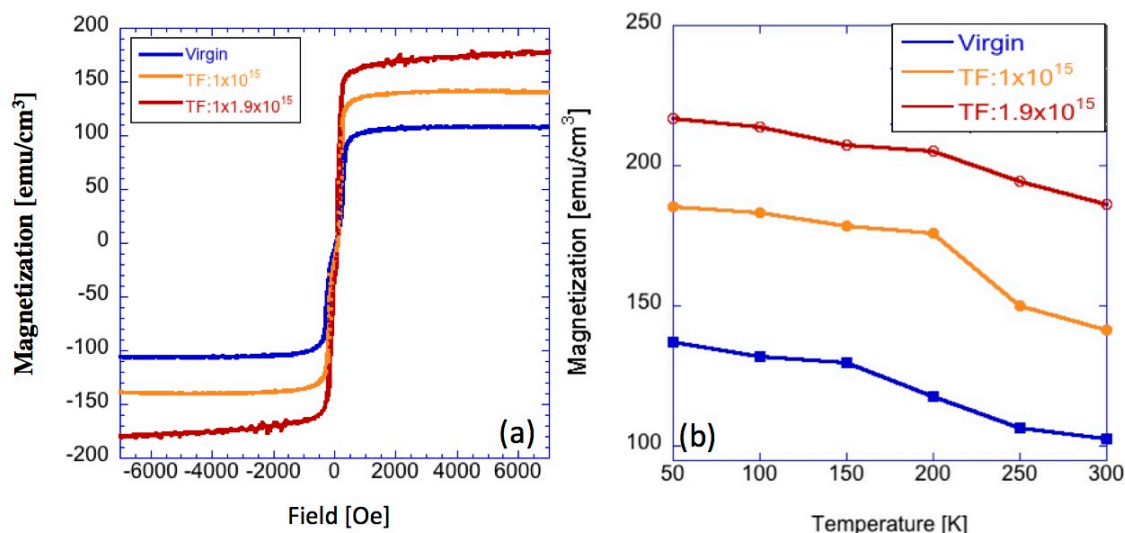


Figure 6.6 Comparison of pre-rad and post-rad measurement. **(a)** In-plane measurement of magnetization vs. magnetic field of $Tb_{30}Fe_{63.5}Co_{6.5}$ with 35nm thickness and **(b)** Saturation moment vs. temperature as a function of proton fluence.

In-plane VSM is used to measure the saturation magnetization, the magnetization as a function of applied magnetic field is shown in **Figure. 6.6a**. The saturated moment increases from 100 emu/cm^3 up to 180 emu/cm^3 monotonically with proton total fluence. The temperature dependence of the saturation moment extracted from in-plane VSM is plotted from 50 -300K, as shown in **Figure 6.6b**. The saturation moment increases as the temperature decrease. The monotonic increase of saturation moment after the proton exposure is also observed for the entire temperature range.

Both simulation and electrical transport suggest that the proton irradiation causes the voids or clusters in the amorphous TbFeCo. Clusters or voids could also directly modify magnetic local structure from rearrangement of elements. The creation of voids has been identified as a cause of swelling of materials which results in lessen the density

of alloy previously[170-172]. The volume expansion could displace atoms from as-growth position. Thus, the fundamental properties related to the distributions of elements such as exchange coupling, local anisotropy and short range order (SRO) would be deviated. It is possible that the displacement damages could lead to the composition inhomogeneity that manifests in the increase in the magnetization moment. However, such a monotonically increase of magnetic moment suggests a systematic modification that contradicts with the random distribution of irradiation-induced defects. Therefore, the local structure modification alone cannot account for such the changes in the magnetic moment.

In Chapters 4 and 5, it has been shown that the proton irradiation not only creates displacement damage, but also causes adiabatic heating that anneals films and leads to the change in the magnetic properties as well as the chemical ordering in different materials. The thermal effects on properties of amorphous materials prior to the crystallization are not extensively investigated since the amorphous material is meta-stable with respect to crystalline system. Generally, thermal annealing is performed at the elevated temperatures that are lower than the crystallization temperature in order to suppress the instability of physical properties in amorphous materials. The low temperature annealing of amorphous RE-TM metal typically does not affect the magnetic properties of materials since it is done at much lower than the Curie temperature of materials. For example, Zhou et al reported that annealing amorphous TbFeCo film at 100 °C more than an hour does not effect perpendicular anisotropy and coercivity of the film[161]. However, several studies reported the variation of magnetic properties of amorphous RE-TM after annealing at higher temperature ranging from 180~300 °C[161,173-175]. The

modifications of magnetic properties usually are described as the drastic reduction of K_U and the increase in M_S . The enhancement of M_S was due to the atomic rearrangement which destroys the pair ordering of the transition metals[173,174]. Such reduction in TM ordering results in the increase of net magnetic moment. Meanwhile Li et al [175] suggested that the alteration of M_S was due to the nanocrystallization that changes the local environment of magnetic elements. It is not conclusive which mechanisms are responsible for the enhancement of M_S .

6.3.4 Magneto transport properties after proton irradiation

(i) Proton irradiation after effects of T_{comp} and H_C

Temperature dependent of Hall resistance is measured as a function of applied magnetic field perpendicular to the film surface from 50K to 300K. **Figure 6.7a** shows H_C of the Hall bar with different widths as a function of the temperature before and after the proton irradiation. The increase of the coercive field is observed for all Hall bar devices after the irradiations.

In addition to the increased coercive field, we also observe the reverse polarity of the Hall loops along with rapidly decrease of H_C around 250K in 0.5 μm and 50 μm wide Hall bars after the irradiations. This temperature is known as the compensation temperature, T_{comp} in ferrimagnetic system, at which the coercivity diverges.

Figure 6.7b shows the dependent of the Hall resistivity (ρ_H) from 50K to 300K of the Hall bars. For 0.5 and 50 μm wide Hall bar devices, as the temperature increases, the Hall resistivity increases toward the compensation temperature, the value of the Hall resistivity transitions from negative to positive over T_{comp} . For the 500 μm wide Hall bar, the value of hall resistivity is not reversed since T_{Comp} (by extrapolation) is over 300K.

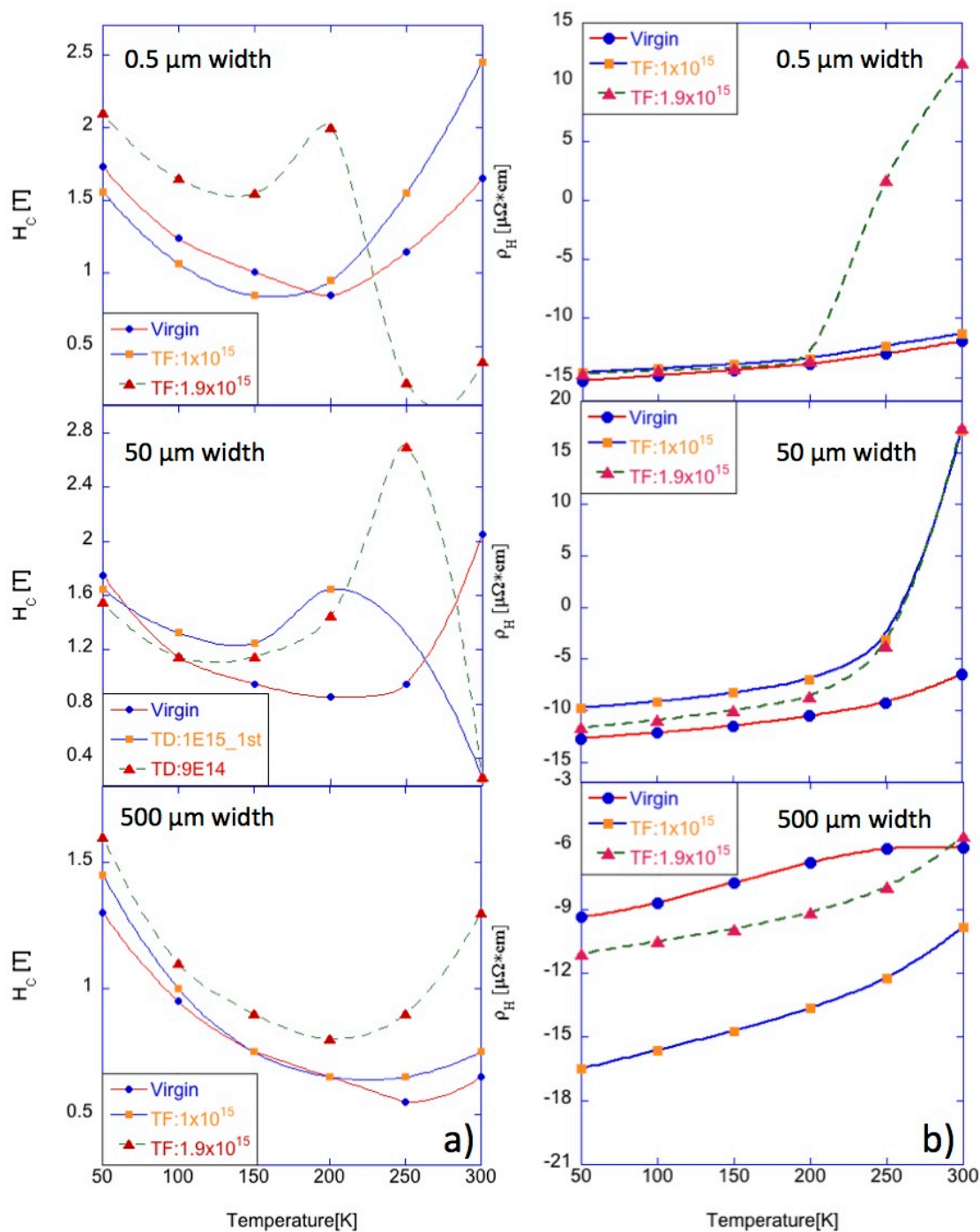


Figure 6.7 Pre-rad and post-rad comparison of (a) coercive field (H_C) and (b) Hall resistivity (ρ_H) as a function of temperature

The abrupt change of coercivity and Hall resistivity at the compensation

temperature is due to the competition of RE and TM moments, which governs the overall magnetization dynamic process as well as the polarity of the anomalous Hall resistance. The enhancement of perpendicular anisotropy is observed after proton irradiation particularly in the 500 μm wide Hall device.

The coercivity enhancement due to the irradiation in magnetic materials can be attributed to the increase in the pinning effect of the magnetic domain wall since the irradiation-induced point defects act as the additional pinning sites. The similar results on TbFeCo wire were found after Ga^+ ions irradiation[113]. The creation of defects may also indirectly enhance coercive field by modifying the internal stress of the films. Commonly, voids cause the tensile stress due to the attractive force between the nearest neighbor atoms across the voids. Therefore, in the presence of voids, the tensile stress could oppose the as-deposited compressive stress, resulting in the relaxation of the growth stress that leads to the coercivity enhancement in TbCoFe.

In contrast to reduction of K_U in previous reports[161,173-175], the improvement of K_U suggests that the thermal-spike from the proton irradiation does not result in the significant crystallization in TbFeCo while it reduces the TM pair orderings that result in the enhancement of M_S . The major difference of thermal spike and conventional annealing is that the heating time on materials. For thermal spike, the adiabatic heating is in picoseconds scale[176], which is much faster than conventional annealing time. Therefore, it is possible for proton irradiation to destroy magnetic pair ordering while preserving amorphicity of the system.

Another major finding is the effect on T_{comp} , which is reduced from above 300K

to ~ 250 K after the proton exposure. The lower compensation temperature of the ferrimagnet accompanies the lower Curie temperature. Hansen et al[59] studied the magnetic properties of wide range of composition of amorphous RE-TM alloy and found that a further increase of the TM content leads to a dramatic increase in T_{comp} and T_C due to the strong TM-TM exchange coupling interaction. Similar result is also found in amorphous GdFeCo system by Poon and his collaborators[177].

(ii) Sublattices' contribution to AHE and magnetization dynamic across compensation temperature

To evaluate the contribution of the sublattices' magnetization, localized atomistic simulations are performed to calculate temperature dependences of sublattices' moment by our collaborator, Li et al. **Figure 6.8** illustrates the temperature dependence of the magnetic moments of Tb, Co and Fe that are normalized to the magnetic moment of Tb at 0 K. The compensation temperature is 350K. At $T < T_{comp}$, the Tb moment contributes most to the total magnetization. As temperature increase, the Tb moment diminishes and then drops to minimum at T_{comp} , then the moment raises up at $T > T_{comp}$. Above T_{comp} the Tb moment becomes comparable to the TM moments. TM moments exhibit a similar temperature dependent behavior. However, the TM moments retain their values better above T_{comp} . The decrease of Tb moment above T_{comp} is because of the relatively low Curie Temperature of Tb ($T_c \sim 222$ K for Tb, $T_c > 1000$ K for Fe and Co).

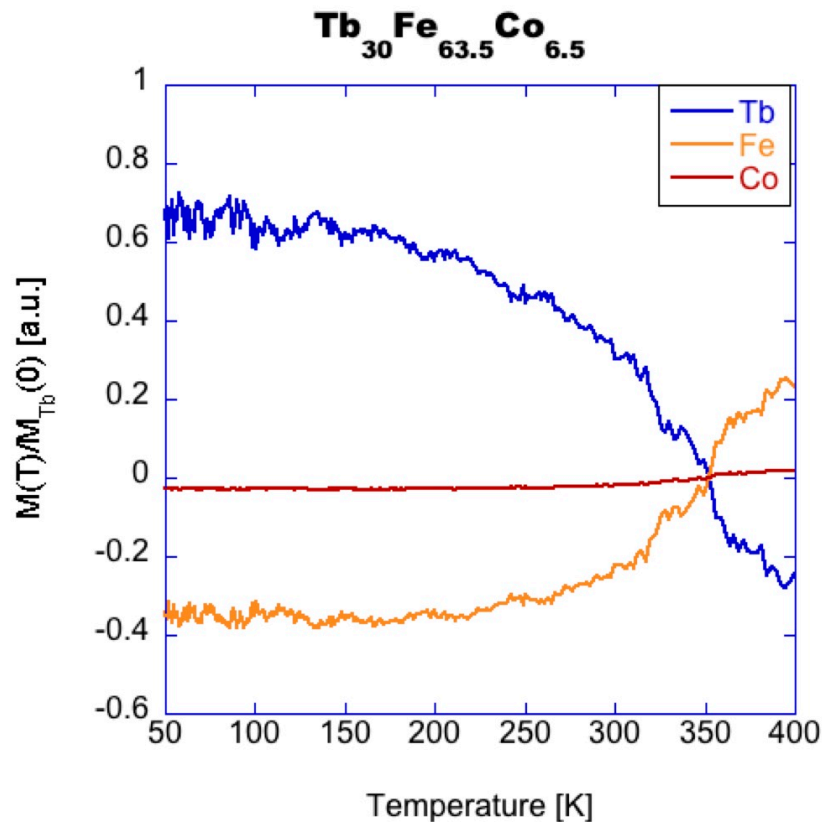


Figure 6.8 Atomistic simulation of sublattices' moment of $Tb_{30}Fe_{63.5}Co_{6.5}$ as a function of temperature. T_{comp} defined as the temperature in which exhibit lowest net magnetization $\sim 350\text{ C}^\circ$ (Courtesy of Xiaopu Li)

Up to now, the contribution of sublattices to Hall resistivity has not been fully clarified. McGuire [178] suggested that in amorphous RE-TM ferrimagnetic system, the AHE is associated with both RE and TM sublattices. The contribution of sublattice magnetization to anomalous Hall resistance can be described as

$$R_H = R_{Tb}M_{Tb} + R_{Fe}M_{Fe} + R_{Co}M_{Co} \quad 6-3$$

where M_{TM} and M_{RE} are the magnetizations of Fe/Co and Tb sublattice, respectively. The contribution of elements to the Hall resistance is not only governed by the sublattice magnetization but also the anomalous Hall coefficient of each element i.e. R_{TM} and R_{RE} .

The Hall resistivity coefficient can possess either negative or positive values depending on the combined effects from Hall coefficients of each sublattice. For instance, Kim et al [179] has studied the compositional effect on the value of R_S of Tb_xCo_{1-x} in the range of x from 25-32 at.%, and x_{comp} is at $x \sim 28$ at.%. The study revealed that the Hall coefficient changes from positive ($x < x_{comp}$, Co dominate) to negative ($x > x_{comp}$, Tb dominate).

Previous studies on the AHE of RE-TM systems have shown the dominant role of the transition metals on the AHE. Mimura et al [180] showed the strong effect of Ni in Gd-Ni alloys and suggested the transition metal plays the more important role for AHE contribution. In 1983, R. Malmhäll [181] also carried out the AHE studies of several TbFe alloys with Tb content ~ 25 at.%, the results also suggested the dominant role to Fe sublattice. It also should be noted that all studies on AHE of RE-TM system has shown that R_{RE} possesses negative value while R_{TM} is positive value.

Temperature dependent of anomalous Hall resistivity $\rho_H(T)$, which reflects temperature dependent of the sublattice magnetization, is further investigated. The Hall resistivity is determined by the relationship

$$\rho_H = R_H t \quad 6-4$$

where R_H is the Hall resistance at high field ($>2T$) and t is the thickness of the film.

As seen in **Figure 6.7b** the Hall resistivity of our TbFeCo is negative below T_{comp} . According to Eq. 6-4, M_{Tb} has to be positive indicating that Tb moment points in the same direction while Fe/Co moments point in the opposite direction with the applied field. Above T_{comp} , this spin configuration is reversed so that Hall resistivity becomes positive value.

As discussed before, the RE moments dominate below T_{comp} and are weakened as

the temperature raises up until the Tb moments are comparable to TM sublattice moments above T_{comp} . From the Hamiltonian equation of Heisenberg model, the sublattice moments align such that the total energy is minimized. In another word, how the moments align with the applied magnetic field is the competition between the anisotropy energy and the Zeeman energy, providing that the exchange integral term remains unchanged after the perturbation by the external H field. Below T_{comp} , Tb moments are in the opposite direction of Fe and Co moments under the applied field. The coercivity rapidly decreases above T_{comp} implying that the TM sublattice, which has a smaller anisotropy, governs the magnetization reversal process.

(iii) Antisymmetric magnetoresistance and domain wall density

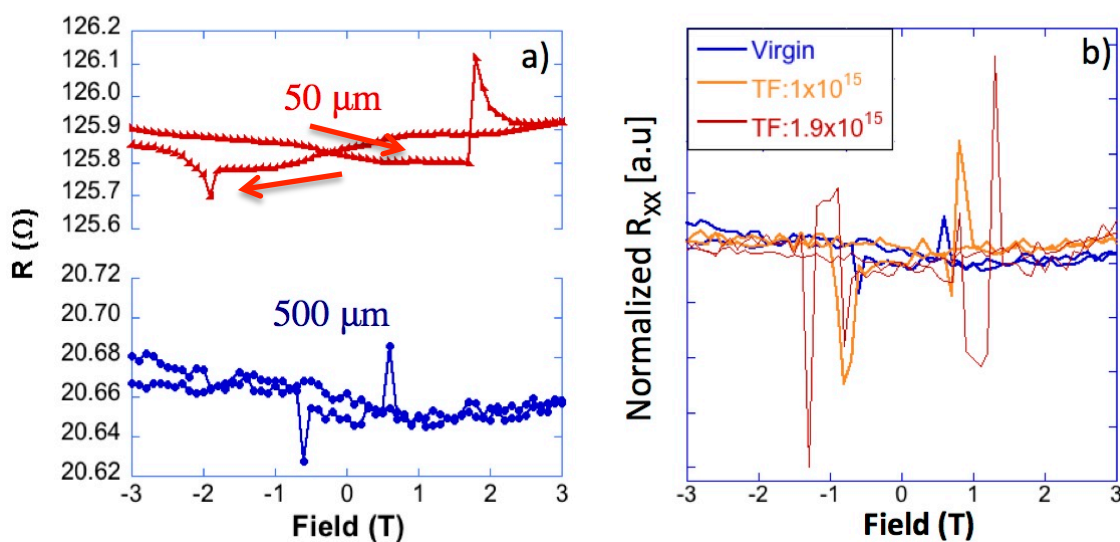


Figure 6.9 (a) Magnetoresistance of 50 μm and 500 μm wide Hall bars at 300K. Two antisymmetric peaks occurred around H_C **(b)** Normalized MR of 500 μm wide Hall bar as a function of radiation total fluence.

Figure 6.9a shows magnetoresistance (R_{xx}) measurements at room temperature for the 50 μm and 500 μm wide Hall bars respectively. The size dependence of the coercivity is also observed in the magneto-resistances of these two Hall bars. Two sharp peaks are observed at the magnetic fields corresponding to H_C in the AHE loops shown in **Figure 6.3a**. As the magnetic field ramps up in the positive direction, the resistance remains almost constant up to the positive H_C where the resistance suddenly increases and forms a positive sharp peak, and then the resistance decreases to almost the same value as before the positive H_C and remains constant value through the maximum 3 T. The same MR behavior was also observed as the magnetic field decrease. There is also a sharp peak at the negative H_C . This resistance peak is negative. These two antisymmetric magneto-resistance peaks are due to the presence of domain walls, electric current and magnetization vector where their directions are mutually perpendicular[182]. The opposite magnetizations across the domain wall cause the opposite Hall fields. This induces the circulating electric current around domain wall, leading the redistribution of the MR peak and the electric field. Similar phenomena have been observed in Pt/Co multilayer structures with PMA[182].

Figure 6.9b shows the MRs of the 500 μm wide Hall device under the different proton fluences. Similarly to the AHE measurement, the MR peak positions also increase after irradiation. MR peak values are normalized to the MR value of the final irradiation (TF: $1 \times 10^{15} \text{ H}^+/\text{cm}^2$) for comparison. MR ratio at 300K of the 500 μm wide Hall device is calculated as

$$MR\% = \frac{R(H_C) - R(0)}{R(0)} \times 100 \quad 6-5$$

where $R(H_C)$ and $R(0)$ are resistance at coercive field and zero field respectively.

The MR% of virgin sample is 0.13 % and increases to 0.44 % and then to 1.095 % after the final irradiation. MR peaks are strongly related with the magnetic domain density, and occur near the coercive field as a result of the multi-domain state of the film during the magnetization reversal process[113]. The monotonic increase of MR% as a function of irradiation fluence suggests that magnetic domain density is increased during magnetization reversal, indicating the reduction in the size of the magnetic domains after the proton exposure.

The induced point defects often act as pinning sites that obstructs the motion of the domain during the magnetization reversal, and thus lead to a higher magnetic domain density[113]. In addition to the domain wall pinning, the change in the intrinsic magnetic properties could also lead to the higher domain density. The domain size is determined by competition domain wall energy density (proportional to $\frac{K_U t}{D}$) and demagnetizing energy (proportional to $M_S^2 D$). The domain wall width (D) in equilibrium then is proportional to $\frac{\sqrt{t K_U}}{M_S}$ where t is the film thickness, K_U is perpendicular anisotropy[113,183,184]. With the magnetization increased 80% after the final irradiation, the domain size should be reduced accordingly, thus it results in the increase in the magnetic domain density.

6.4 Summary

The 2-MeV proton beam is used to irradiate TbFeCo films with the total fluence up to $1.9 \times 10^{15} \text{ cm}^{-2}$. Due to the ferrimagnetic nature, there exists a compensation temperature, T_{comp} , at which the magnetization is minimum. Consequently, the conventional magnetometer is not suitable to fully characterize these materials in vicinity of the compensation point. The magneto transport behavior is utilized in combination

with the conventional vibrating magnetometer to probe the effects of the proton irradiation effects on the microstructure and the magnetic properties of TbFeCo. It is found that the saturation moment along with coercive field increases, but the compensation temperature decreases after the proton exposure. The thermal spikes associated with the displacement damage is likely among the mechanisms to reduce the magnetic ordering of transition elements in this amorphous system, which lead to the enhancement of M_S . Meanwhile the formation of voids/clusters is mainly responsible for the coercivity enhancement via the domain wall pinning mechanism and the modification of the film strain state.

CHAPTER 7. Conclusions and future work

7.1 Summary

As the key elements of the MRAM technology, the STT-MTJ devices have been studied for their tolerance to irradiation. With the focus on ionization and displacement damage, the irradiation effects on the physical properties of MTJs are found to depend on the types of radiation, structures, and degrees of inherent structural order and disorder, as well as the device size. Major discoveries are summarized as follows.

The STT-MTJ devices with diameters ranging from 50 nm to 500 nm are exposed to multi-species irradiations including x-ray, heavy ions such as Neon, and proton. The STT-MTJ devices are considered to be “Rad Hard” with an exception that a couple of 60 nm devices failed state retention, which appears to be caused by single electron effect (SEE) phenomena, after a fluence of proton irradiation that is beyond the CMOS standard. The adiabatic heating process, a by-product of the ionization process, plays an important role for a small but appreciable (up to 18%) increase of TMR in MTJ devices after the accumulated irradiation of 10keV-energy x-rays reach the total ionization dose (TID) of 1Mrad(Si). In contrast to conventional annealing, the after-effect from electronic excitation of elements induces a very localized annealing process, which could innovate annealing methods especially for multilayer structures for which buried layers are difficult to anneal. To induce the displacement damages, 2 MeV-energy Neon ions and protons with total fluence up to 1×10^{12} particles/cm² are used to irradiate the MTJ devices separately. After Neon irradiation, all devices show a normal switching character and state retention. In addition TMR remained relatively unchanged despite the expected significant displacement damage (*dpa* ~1500 times of proton's), indicating no radiation-

induced damages to the MgO tunnel barrier. However, after proton irradiation, two devices with diameter 60 nm fail to retain the pre-set state and show unstable behavior during the state retention test, for which ionization damage that may be characterized as trapped charges at an oxide, interface is responsible.

Several novel perpendicular magnetic anisotropy material systems potentially for the spintronics application including interfacial anisotropy CoFeB/MgO and Co/Pd multilayers, $L1_0$ MnAl, and amorphous rare earth-iron-cobalt (RE-Fe-Co) are investigated for their tolerance to 2 MeV protons.

Proton irradiations with fluences up to 1×10^{14} H^+/cm^2 are used for CoFeB/MgO and Co/Pd samples. The x-ray diffuse scattering and fast Fourier transform (FFT) analysis of x-ray reflectivity suggest very little radiation induced-intermixing at the interfaces of magnetic layers. As a result, no measurable changes in magnetic properties have been observed as the materials retain perpendicular magnetic anisotropy and magnetization.

Incremental radiation doses approach is a suitable strategy for radiation effects research as it effectively probes the evolution of radiation damages. Proton radiation affects the highly ordered $L1_0$ MnAl system whereby the modification of magnetic properties results from the combined effect of irradiation-induced thermal annealing and atomic displacement. Virgin samples exhibit highly ordered growth with a chemical ordering parameter $S \sim 0.97$. After the 1st irradiation with a total fluence of 1×10^{14} H^+/cm^2 , S is reduced to ~ 0.8 , and further down to ~ 0.72 when the fluence increases to 1×10^{15} H^+/cm^2 that can be attributed to the displacement damages caused by the proton beam. At the final irradiation with the total fluence 2×10^{15} H^+/cm^2 , the trend in the

change of the chemical ordering is reversed with the recovery of an S of ~ 0.81 thanks to the irradiation-induced annealing which recovers the chemical ordering in MnAl. Despite the change in the chemical ordering, the magnetic properties and magneto-transport properties of the MnAl thin film exhibit very small changes during the irradiation process, which makes it a promising material candidate for the “Rad Hard” spintronic devices.

In amorphous rare earth transition metal alloys (TbFeCo), the proton irradiations with the fluence of up to $2 \times 10^{15} \text{ H}^+/\text{cm}^2$ are used to irradiate the sample with a normal incident angle, i.e. the proton beam is perpendicular to the sample surface. Both displacement and ionization damages are observed. Effects of defect formations are observed through a small enhancement of the coercive field that originates from domain wall pinning, and an increase in the electric resistivity as the thin film becomes more porous. The most intriguing effect is from the ionization damages, for which the thermal spike associated with the ionization process results in the reduction of the TM-TM ordering of alloy, which modifies the magnetic properties of the RE-TM alloy. The magnetization increase monotonically from $100 \text{ emu}/\text{cm}^3$ to $180 \text{ emu}/\text{cm}^3$ with the irradiation fluence, and the compensation temperature of the films is lowered simultaneously. Due to the high magnetostriction coefficient of TbFeCo, irradiation can induce the thermal spikes that relax the internal stress via the inter-defect interaction. Though TbFeCo does not exhibit “Rad Hard” properties, one can still utilize the irradiation technique as an effective means for the modification of the magnetic properties of RE-TM alloys.

7.2 Suggested future work

There still remain many aspects to explore in order to understand the radiation interaction with magnets as well as to utilize irradiation as a process to manipulate or investigate the magnetic properties and spin dependent transport in magnetic materials despite the microstructure. Followings are some recommendations for future study.

(i) “Rad hard” evaluation:

Different ion species irradiation

Radiation environments vary significantly in the range of particle types and energies, and it is evident that the irradiation damage varies greatly in accordance with the radiation species/energy/dosage. Irradiation studies with different ions species such as thermal neutron, alpha particles, gamma rays are much needed in order to establish a comprehensive perspective on this subject.

Utilization of in-situ measurements

The use of in-situ measurement as simple as I-V characterization across MTJs may provide a dynamic view of damages creations, which give a more profound understanding of critical factors for radiation hardness in materials.

(ii) Irradiation as a material process tool:

Local and transient thermal annealing

I propose that the x-ray irradiation can be used as a localized thermal annealing for MTJ devices via adiabatic heating. Such annealing has the advantage as “selective annealing” since the generated heat is dependent on the x-ray absorption coefficient of materials. Typically the x-ray adsorption coefficients of transition metals (typically in the MTJ devices) are greater than that of Silicon (the underlying CMOS structure). This

new technique could help the integration of MTJ devices to Si CMOS circuits and improve the performance of MTJs.

Non-destructive technique for ferromagnetic patterning

The irradiation has been demonstrated to “pattern” magnetic materials recently[185], in which a low energy proton beam is used to pattern on a 100 nm-scale of $[\text{Co}/\text{Pd}]_n$ magnetic array with perpendicular magnetic anisotropy from $[\text{Co}_3\text{O}_3/\text{Pd}]_n$ as-deposited films. The recovery of chemical ordering of $L1_0$ MnAl suggests that proton irradiation can induce ordering as well as the disordering of crystalline materials depending on the degrees of inherent structural ordering and other factors. With more systematic study, the irradiation could be used for non-destructive patterning to realize patterning with a sub 100 nanometer resolution.

Magnetic modification/investigation tool

Irradiation with magnetic ion species is particularly appealing. The implanted magnetic species can be manipulated at different time scales, which may help to elucidate the dynamic exchange interaction between the implanted species and the local magnetic environment.

For amorphous RE-TM alloys, the origin of the large magnetic anisotropy remains an interesting theme. The irradiation process could help to investigate this subject by modifying the short range ordering in these amorphous systems. Initial study with different incident angles has been performed on GdFeCo to investigate the PMA of this material. Preliminary results show different modifications between 90° degree and 45° .

BIBLIOGRAPHY

- [1] W. Shockley, J. H. Hollomon, R. Maurer, and F. Seitz, *Imperfections in Nearly Perfect Crystals* (John Willey and Sons, 1952).
- [2] T. Skotnicki, J. A. Hutchby, T.-J. King, H. S. P. Wong, and F. Boeuf, *Circuits and Devices Magazine*, IEEE **21**, 16 (2005).
- [3] T. H. Ning, *ECS Transactions* **6**, 3 (2007).
- [4] T. H. Ning, in (2010), p. 3.
- [5] S. A. Wolf, *Science* **294**, 1488 (2001).
- [6] S. A. Wolf, J. Lu, M. R. Stan, and E. Chen, in (2010).
- [7] A. Fert, *Thin Solid Films* (2008).
- [8] H. Ohno, *Nat Mater* (2010).
- [9] M. Marinella, in *2013 IEEE Aerospace Conference* (IEEE, 2013), pp. 1–11.
- [10] M. N. Baibich, J. M. Broto, A. Fert, F. Nguyen Van Dau, F. Petroff, others, *Phys Rev Lett* **61**, 2472 (1988).
- [11] I. Schuller, C. M. Falco, J. Hilliard, J. Ketterson, B. Thaler, R. Lacoce, and R. Dee, in (1979), pp. 417–421.
- [12] N. F. Mott, in (1936), pp. 699–717.
- [13] C. Chappert, A. Fert, and F. N. Van Dau, *Nat Mater* **6**, 813 (2007).
- [14] G. Prinz, *Science* **282**, 1660 (1998).
- [15] M. Gijs, S. Lenczowski, and J. Giesbers, *Phys Rev Lett* **70**, 3343 (1993).
- [16] P. M. Tedrow and R. Meservey, *Phys Rev Lett* (1971).
- [17] P. M. Tedrow and R. Meservey, *Phys Rev B* (1973).
- [18] M. Julliere, *Physics Letters A* **54**, 225 (1975).

- [19] J. Moodera, L. Kinder, T. Wong, and R. Meservey, *Phys Rev Lett* **74**, 3273 (1995).
- [20] T. Miyazaki and N. Tezuka, *Journal of Magnetism and Magnetic Materials* **139**, L231 (1995).
- [21] S. Yuasa, *J. Phys. Soc. Jpn.* **77**, 1001 (2008).
- [22] D. Wang, C. Nordman, J. M. Daughton, Z. Qian, J. Fink, D. Wang, C. Nordman, J. M. Daughton, Z. Qian, and J. Fink, *Ieee T Magn* **40**, 2269 (2004).
- [23] Y. Sakuraba, M. Hattori, M. Oogane, Y. Ando, H. Kato, A. Sakuma, T. Miyazaki, and H. Kubota, *Appl Phys Lett* **88**, 192508 (2006).
- [24] W. H. Butler, X. G. Zhang, T. C. Schulthess, and J. M. MacLaren, *Phys Rev B* **63**, 054416 (2001).
- [25] S. Parkin, C. Kaiser, A. Panchula, and P. M. Rice, *Nat Mater* (2004).
- [26] S. Yuasa, T. Nagahama, A. Fukushima, Y. Suzuki, and K. Ando, *Nat Mater* **3**, 868 (2004).
- [27] J. Mathon and A. Umerski, *Phys Rev B* **63**, 220403 (2001).
- [28] Y. M. Lee, J. Hayakawa, S. Ikeda, F. Matsukura, and H. Ohno, *Appl Phys Lett* **90**, 212507 (2007).
- [29] B. N. Engel, J. Akerman, B. Butcher, R. W. Dave, M. DeHerrera, M. Durlam, G. Grynkewich, J. Janesky, S. V. Pietambaram, N. D. Rizzo, J. M. Slaughter, K. Smith, J. J. Sun, and S. Tehrani, *Ieee T Magn* **41**, 132 (2005).
- [30] J. C. Slonczewski, *Journal of Magnetism and Magnetic Materials* **159**, L1 (1996).
- [31] L. Berger, *Phys. Rev., B Condens. Matter* **54**, 9353 (1996).

- [32] J. Barnas, A. Fuss, R. Camley, P. Grünberg, and W. Zinn, *Phys. Rev., B Condens. Matter* **42**, 8110 (1990).
- [33] J. C. Slonczewski, *Journal of Magnetism and Magnetic Materials* **247**, 324 (2002).
- [34] R. Sbiaa, S. Y. H. Lua, R. Law, H. Meng, R. Lye, and H. K. Tan, *J Appl Phys* **109**, (2011).
- [35] S. Mangin, D. Ravelosona, Y. Henry, and J. A. Katine, ... *Bulletin* (2008).
- [36] Y. Huai, *AAPPS Bulletin* (2008).
- [37] M. Gajek, J. J. Nowak, J. Z. Sun, P. L. Trouilloud, E. J. O'Sullivan, D. W. Abraham, M. C. Gaidis, G. Hu, S. Brown, Y. Zhu, R. P. Robertazzi, W. J. Gallagher, and D. C. Worledge, *Appl Phys Lett* **100**, 132408 (2012).
- [38] H. Kōno, *J. Phys. Soc. Jpn.* **13**, 1444 (1958).
- [39] A. J. J. Koch, P. Hokkeling, M. G. von d Steeg, and K. J. de Vos, *J Appl Phys* **31**, S75 (1960).
- [40] A. Sakuma, *J. Phys. Soc. Jpn.* **63**, 1422 (1994).
- [41] T. Sands, J. P. Harbison, M. L. Leadbeater, S. J. Allen, G. W. Hull, R. Ramesh, and V. G. Keramidas, *Appl Phys Lett* **57**, 2609 (1990).
- [42] C. Yanar, J. M. K. Wiezorek, W. A. Soffa, and V. Radmilovic, *Metall and Mat Trans A* **33**, 2413 (2002).
- [43] J. H. Huang, Kuo, P. C., and S. C. Shen, *Ieee T Magn* **31**, 2494 (1995).
- [44] T. M. Rosier, Y. W. He, and N. A. El-Masry, *Mater Lett* **26**, 227 (1996).
- [45] Ching-Ming Lee, Lin-Xiu Ye, Jia-Mou Lee, Wan-Ling Chen, Chao-Yuan Huang, Gung Chern, and Te-Ho Wu, *Ieee T Magn* **45**, 3808 (2009).

- [46] M. Nakayama, T. Kai, N. Shimomura, M. Amano, E. Kitagawa, T. Nagase, M. Yoshikawa, T. Kishi, S. Ikegawa, and H. Yoda, in *J Appl Phys* (2008), p. 07A710.
- [47] N. Nishimura, T. Hirai, A. Koganei, T. Ikeda, K. Okano, Y. Sekiguchi, and Y. Osada, *J Appl Phys* **91**, 5246 (2002).
- [48] B. Dai, T. Kato, S. Iwata, and S. Tsunashima, *Ieee T Magn* **48**, 3223 (2012).
- [49] H. J. Leamy and A. G. Dirks, *J Appl Phys* (1979).
- [50] Y. TAKENO, K. KANEKO, and K. GOTO, *Jpn J Appl Phys* **1** **30**, 1701 (1991).
- [51] J. Coey, J. Chappert, J. Rebouillat, and T. Wang, *Phys Rev Lett* **36**, 1061 (1976).
- [52] Y. SUZUKI, S. TAKAYAMA, F. KIRINO, and N. OHTA, *Ieee T Magn* **23**, 2275 (1987).
- [53] V. G. HARRIS, K. D. AYLESWORTH, B. N. DAS, W. T. ELAM, and N. C. KOON, *Phys Rev Lett* **69**, 1939 (1992).
- [54] Y. H. Fang, Kuo, P. C., C. Y. Chou, S. C. Chen, N. W. Cheng, and P. L. Lin, *Journal of Magnetism and Magnetic Materials* **310**, e930 (2007).
- [55] M. T. Rahman, X. Liu, M. Matsumoto, A. Morisako, S. Meguro, and K. Akahane, *J Appl Phys* **97**, 10C515 (2005).
- [56] M. J. Hadley, R. Atkinson, and R. J. Pollard, *Journal of Magnetism and Magnetic Materials* **246**, 347 (2002).
- [57] S. Q. Yin, X. Q. Li, X. G. Xu, J. Miao, and Y. Jiang, *Ieee T Magn* **24**, 3129 (1988).

- [58] B. D. Cullity and C. D. Graham, *Introduction to Magnetic Materials* (John Wiley & Sons, 2011).
- [59] P. Hansen, C. Clausen, G. Much, M. Rosenkranz, and K. Witter, *J Appl Phys* **66**, 756 (1989).
- [60] S. Nakagawa, M. Yamada, and N. Tokuriki, *Ieee T Magn* **42**, 3773 (2006).
- [61] A. Bur, T. Wu, J. Hockel, C.-J. Hsu, H. K. D. Kim, T.-K. Chung, K. Wong, K. L. Wang, and G. P. Carman, *J Appl Phys* **109**, 123903 (2011).
- [62] M. Ohta, K. Yamada, Y. Satake, A. Fujita, and K. Fukamichi, *Mater Trans* **44**, 2605 (2003).
- [63] U. Gradmann and J. Müller, *Physica Status Solidi (B)* **27**, 313 (1968).
- [64] B. Engel, C. England, R. Van Leeuwen, M. Wiedmann, and C. Falco, *Phys Rev Lett* **67**, 1910 (1991).
- [65] J. G. Gay and R. Richter, *Phys Rev Lett* **56**, 2728 (1986).
- [66] Y. Wu, J. Stöhr, B. Hermsmeier, M. Samant, and D. Weller, *Phys Rev Lett* **69**, 2307 (1992).
- [67] B. Engel, M. Wiedmann, Van Leeuwen RA, and C. Falco, *Phys. Rev., B Condens. Matter* **48**, 9894 (1993).
- [68] B. Újfalussy, L. Szunyogh, P. Bruno, and P. Weinberger, *Phys Rev Lett* **77**, 1805 (1996).
- [69] P. Bruno, *Phys. Rev., B Condens. Matter* **39**, 865 (1989).
- [70] T. Koide, T. Shidara, K. Yamaguchi, A. Fujimori, H. Fukutani, N. Nakajima, T. Sugimoto, T. Katayama, and Y. SUZUKI, *Phys. Rev., B Condens. Matter* **53**, 8219 (1996).

- [71] N. Nakajima, T. Koide, T. Shidara, H. Miyauchi, H. Fukutani, others, *Phys Rev Lett* (1997).
- [72] S. Monso, B. Rodmacq, S. Auffret, G. Casali, F. Fettar, B. Gilles, B. Dieny, and P. Boyer, *Appl Phys Lett* **80**, 4157 (2002).
- [73] A. Manchon, C. Ducruet, L. Lombard, S. Auffret, B. Rodmacq, B. Dieny, S. Pizzini, J. Vogel, V. Uhlir, M. Hochstrasser, and G. Panaccione, *J Appl Phys* **104**, 3914 (2008).
- [74] L. E. Nistor, B. Rodmacq, S. Auffret, and B. Dieny, *Appl Phys Lett* (2009).
- [75] Shimabukuro, Nakamura, Akiyama, Ito, *Physica E Low Dimens Syst Nanostruct* **42**, 4 (2010).
- [76] S. Ikeda, K. Miura, H. Yamamoto, K. Mizunuma, H. D. Gan, M. Endo, S. Kanai, J. Hayakawa, F. Matsukura, and H. Ohno, *Nat Mater* **9**, 721 (2010).
- [77] A. V. Narlikar, *Irradiation Effects and Cationic Disorder in HTS* (Nova Science Pub Incorporated, 2003).
- [78] I. J. I. Jun, M. A. Xapsos, S. R. Messenger, E. A. Burke, R. J. Walters, G. P. Summers, and T. Jordan, *IEEE Trans. Nucl. Sci.* **50**, 1924 (2003).
- [79] A. Holmes-Siedle and L. Adams, *Handbook of Radiation Effects* (OUP Oxford, 2002).
- [80] J. K. Shultis and R. E. Faw, *Fundamentals of Nuclear Science and Engineering Second Edition* (CRC Press, 2007).
- [81] K. E. Sickafus, R. W. Grimes, J. A. Valdez, A. Cleave, M. Tang, M. Ishimaru, S. M. Corish, C. R. Stanek, and B. P. Uberuaga, *Nat Mater* **6**, 217 (2007).
- [82] Y. Matsushima, Y. Chimi, N. Ishikawa, and T. Kambara, *Nuclear Instruments*

- and ... (2006).
- [83] F. Ono, Y. Chimi, N. Ishikawa, and H. Kanamitsu, Nuclear Instruments and ... (2007).
- [84] J. Liu, C. Chen, J. Talnagi, S. Wu, and M. Harmer, Proceedings of Space Nuclear Conference 2007 1 (2007).
- [85] D. Ravelosona, C. Chappert, V. Mathet, and H. Bernas, Appl Phys Lett **76**, 236 (2000).
- [86] I. Škorvánek and A. Zentko, Phys. Stat. Sol. (a) **99**, 275 (1987).
- [87] D. G. Fisher, R. B. Murray, and C. P. Swann, J Appl Phys **56**, 1055 (1984).
- [88] C. G. Kim, H. C. Kim, S. S. Yoon, D. G. Park, and J. H. Hong, Journal of Magnetism and Magnetic Materials **203**, 217 (1999).
- [89] D. G. Park, C. G. Kim, H. C. Kim, J. H. Hong, and I. S. Kim, J Appl Phys **81**, 4125 (1997).
- [90] H. C. Kim, S. C. Yu, C. G. Kim, H. S. Han, W. K. Cho, and D. H. Kim, J Appl Phys **87**, 7115 (2000).
- [91] M. C. Ridgway, T. Bierschenk, R. Giulian, B. Afra, M. D. Rodriguez, L. L. Araujo, A. P. Byrne, N. Kirby, O. H. Pakarinen, F. Djurabekova, K. Nordlund, M. Schleberger, O. Osmani, N. Medvedev, B. Rethfeld, and P. Kluth, Phys Rev Lett **110**, 245502 (2013).
- [92] T. Banerjee, T. Som, D. Kanjilal, and J. S. Moodera, The European Physical Journal Applied Physics **32**, 115 (2005).
- [93] M. D. Sacher, J. Sauerwald, J. Schmalhorst, and G. Reiss, J Appl Phys **98**, 103532 (2005).

- [94] D. Kobayashi, Y. Takehashi, K. Hirose, S. Onoda, T. Makino, T. Ohshima, S. Ikeda, M. Yamanouchi, H. Sato, E. C. Enobio, T. Endoh, and H. Ohno, in (2013), pp. 1–5.
- [95] H. Hughes, K. Bussmann, and P. J. McMarr, *Nuclear Science* (2012).
- [96] F. Ren, A. Jander, P. Dhagat, and C. Nordman, *Nuclear Science, IEEE Transactions on* **59**, 3034 (2012).
- [97] C. Hammond, *The Basics of Crystallography and Diffraction* (Oxford University Press, 2009).
- [98] S. Kittiwatanakul, Ph.D. Dissertation, UVa 2014 1 (2014).
- [99] N. W. Ashcroft and N. D. Mermin, *Solid State Physics* (2011).
- [100] H. Bremers, J. Hesse, H. Ahlers, and J. Sievert, *Journal of Alloys and ...* (2004).
- [101] K. Barmak, J. Kim, L. H. Lewis, K. R. Coffey, M. F. Toney, A. J. Kellock, and J. U. Thiele, *J Appl Phys* **98**, 3904 (2005).
- [102] D. J. Sellmyer and R. Skomski, *Advanced Magnetic Nanostructures* (Springer Science & Business Media, 2006).
- [103] J. Daillant and A. Gibaud, *X-Ray and Neutron Reflectivity* (Springer Science & Business Media, 2009).
- [104] R. I. Barabash, G. E. Ice, and P. E. A. Turchi, *Diffuse Scattering and the Fundamental Properties of Materials* (Momentum Press, 2009).
- [105] E. T. De Lacheisserie, D. Gignoux, and M. Schlenker, (2004).
- [106] N. Nagaosa, *J. Phys. Soc. Jpn.* **75**, 042001 (2006).
- [107] N. Nagaosa, J. Sinova, S. Onoda, A. H. MacDonald, and N. P. Ong, *Reviews of*

- Modern Physics **82**, 1539 (2010).
- [108] J. Smit, *Physica* **21**, 877 (1955).
- [109] J. Smit, *Physica* **24**, 39 (1958).
- [110] L. Berger, *Phys Rev B* **2**, 4559 (1970).
- [111] C. L. Chien and C. R. Westgate, *The Hall Effect and Its Applications* (Plenum Publishing Corporation, 1980).
- [112] A. Chtchelkanova, S. A. Wolf, and Y. Idzerda, *Magnetic Interactions and Spin Transport* (Springer Science & Business Media, 2003).
- [113] S. Li, T. Amagai, X. Liu, and A. Morisako, *Appl Phys Lett* **99**, 122501 (2011).
- [114] G. Bergmann, *Physics Reports* **107**, 1 (1984).
- [115] H. Meng and J.-P. Wang, *Appl Phys Lett* **88**, 2506 (2006).
- [116] X. Zhu and J. G. Zhu, *Magnetics* (2006).
- [117] H. Moriceau, F. Mazen, C. Braley, F. Rieutord, A. Tauzin, and C. Deguet, *Nucl Instrum Methods Phys Res B* **277**, 84 (2012).
- [118] H. J. Woo, H. W. Choi, G. D. Kim, J. K. Kim, W. Hong, Y. Y. Ji, W. B. Choi, and Y. H. Bae, (2004).
- [119] US5374564 (n.d.).
- [120] D. E. Savage, J. Kleiner, and N. Schimke, *Journal of Applied ...* (1991).
- [121] L. J. Brillson, *Surfaces and Interfaces of Electronic Materials* (John Wiley & Sons, 2010).
- [122] R. S. Bauer, *Surfaces and Interfaces: Physics and Electronics* (Elsevier, 2012).
- [123] D. M. Fleetwood and R. D. Schrimpf, *Defects in Microelectronic Materials and Devices* (CRC Press, 2008).

- [124] M. Endo, S. Kanai, S. Ikeda, F. Matsukura, and H. Ohno, *Appl Phys Lett* **96**, 212503 (2010).
- [125] R. Gontarz and T. Lucinski, *Journal of Magnetism and Magnetic Materials* **101**, 253 (1991).
- [126] L. F. Schelp, M. Carara, A. D. C. Viegas, M. A. Z. Vasconcellos, and J. E. Schmidt, *J Appl Phys* **75**, 5262 (1994).
- [127] J. R. Schwank, M. R. Shaneyfelt, and P. E. Dodd, *IEEE Trans. Nucl. Sci.* **60**, 2074 (2013).
- [128] C. Pellegrini and J. Stöhr, *Nucl Instrum Methods Phys Res A* **500**, 33 (2003).
- [129] F. Biggs, R. Lighthill, and S. Corporation, *Analytical Approximations for X-Ray Cross Sections II* (1971).
- [130] Y. M. Lee, J. Hayakawa, S. Ikeda, F. Matsukura, and H. Ohno, arXiv **cond-mat.mtrl-sci**, 042506 (2006).
- [131] G.-X. Miao, K. B. Chetry, A. Gupta, W. H. Butler, K. Tsunekawa, D. Djayaprawira, and G. Xiao, *J Appl Phys* **99**, (2006).
- [132] X. Liu, D. Mazumdar, W. Shen, B. D. Schrag, and G. Xiao, *Appl Phys Lett* **89**, 023504 (2006).
- [133] W. G. Wang, C. Ni, G. X. Miao, C. Weiland, L. R. Shah, X. Fan, P. Parson, J. Jordan-Sweet, X. M. Kou, Y. P. Zhang, R. Stearrett, E. R. Nowak, R. Opila, J. S. Moodera, and J. Q. Xiao, *Phys Rev B* **81**, 144406 (2010).
- [134] T. Maruyama, Y. Shiota, T. Nozaki, K. Ohta, N. Toda, M. Mizuguchi, A. A. Tulapurkar, T. Shinjo, M. Shiraishi, S. Mizukami, Y. Ando, and Y. SUZUKI, *Nature Nanotech* **4**, 158 (2009).

- [135] S. Kanai, M. Yamanouchi, S. Ikeda, Y. Nakatani, F. Matsukura, and H. Ohno, *Appl Phys Lett* **101**, 122403 (2012).
- [136] J. R. Schwank, M. R. Shaneyfelt, D. M. Fleetwood, J. A. Felix, P. E. Dodd, P. Paillet, and V. Ferlet-Cavrois, *IEEE Trans. Nucl. Sci.* **55**, 1833 (2008).
- [137] Y. Conraux, J. P. Nozières, V. Da Costa, M. Toulemonde, and K. Ounadjela, *J Appl Phys* **93**, 7301 (2003).
- [138] J. Schmalhorst, S. Kämmerer, M. Sacher, and G. Reiss, *Phys Rev B* (2004).
- [139] J. Schmalhorst and G. Reiss, *Journal of Magnetism and Magnetic Materials* (2004).
- [140] D. Kobayashi, Y. Kakehashi, K. Hirose, S. Onoda, T. Makino, T. Ohshima, S. Ikeda, M. Yamanouchi, H. Sato, E. C. Enobio, T. Endoh, and H. Ohno, *IEEE Trans. Nucl. Sci.* **61**, 1710 (2014).
- [141] R. R. Katti, J. Lintz, L. Sundstrom, T. Marques, S. Scoppettuolo, and D. Martin, in *2009 IEEE Radiation Effects Data Workshop (in Conjunction with NSREC 2009)* (IEEE, 2009), pp. 103–105.
- [142] C. Chappert, *Science* **280**, 1919 (1998).
- [143] A. Mougin, T. Mewes, M. Jung, D. Engel, A. Ehresmann, H. Schmoranzler, J. Fassbender, and B. Hillebrands, *Phys Rev B* **63**, 060409 (2001).
- [144] C.-H. Lai, C.-H. Yang, and C. C. Chiang, *Appl Phys Lett* **83**, 4550 (2003).
- [145] P. Esquinazi, D. Spemann, R. Höhne, A. Setzer, K. H. Han, and T. Butz, *Phys Rev Lett* **91**, 227201 (2003).
- [146] D. R. Olander, (1976).
- [147] B. E. Warren and X. Diffraction, New York (1990).

- [148] A. Gupta and D. Kumar, Nucl Instrum Methods Phys Res B **244**, 202 (2006).
- [149] Y. Cui, W. Yin, W. Chen, J. Lu, and S. A. Wolf, J Appl Phys **110**, 103909 (2011).
- [150] J. H. Park, Y. K. Hong, S. Bae, J. J. Lee, J. Jalli, G. S. Abo, N. Neveu, S. G. Kim, C. J. Choi, and J. G. Lee, J Appl Phys **107**, 09A731 (2010).
- [151] A. Gerber, A. Milner, L. Goldshmit, M. Karpovski, B. Lemke, H. U. Habermeier, and A. Sulpice, Phys Rev B **65**, 054426 (2002).
- [152] D. Rosenblatt, M. Karpovski, and A. Gerber, Appl Phys Lett **96**, 022512 (2010).
- [153] M. Haidar and M. Bailleul, Phys Rev B (2013).
- [154] M. A. Angadi and V. Thanigaimani, J Mater Sci Lett **9**, 1087 (1990).
- [155] V. A. Gopar, D. Weinmann, R. A. Jalabert, and R. L. Stamps, Phys Rev B (2004).
- [156] Y. Mimura, N. Imamura, T. Kobayashi, A. Okada, and Y. Koshiro, J Appl Phys **49**, 1208 (1978).
- [157] N. Anuniwat, M. Ding, S. J. Poon, S. A. Wolf, and J. Lu, J Appl Phys **113**, 043905 (2013).
- [158] C. Stanciu, A. Tsukamoto, A. Kimel, F. Hansteen, A. Kirilyuk, A. Itoh, and T. Rasing, Phys Rev Lett **99**, 217204 (2007).
- [159] C. E. Graves, A. H. Reid, T. Wang, B. Wu, and S. de Jong, Nat Mater (2013).
- [160] M. Ding and S. J. Poon, arXiv (2013).
- [161] Y. Zhou, C. Yang, D. Zhou, X. Zhao, and J. Zhang, in (2000), pp. 506–509.
- [162] R. C. O'Handley, *Modern Magnetic Materials* (Wiley-Interscience, 1999).

- [163] O. Ersen, V. Parasote, V. Pierron-Bohnes, M. C. Cadeville, and C. Ulhaq-Bouillet, *J Appl Phys* **93**, 2987 (2003).
- [164] F. Cayssol, D. Ravelosona, C. Chappert, J. Ferre, and J. P. Jamet, *Phys Rev Lett* **92**, 107202 (2004).
- [165] J. P. Attane, D. Ravelosona, A. Marty, V. D. Nguyen, and L. Vila, *Phys Rev B* **84**, 144418 (2011).
- [166] V. D. Nguyen, L. Vila, A. Marty, J. C. Pillet, L. Notin, C. Beigne, S. Pizzini, and J. P. Attane, *Appl Phys Lett* **100**, 252403 (2012).
- [167] H. Windischmann, *J. Vac. Sci. Technol. A* **9**, 2431 (1991).
- [168] M. T. Rahman, X. Liu, and A. Morisako, *J Appl Phys* (2006).
- [169] P. S. Liu, T. F. Li, and C. Fu, *Materials Science and Engineering: A* (1999).
- [170] T. Kimoto, H. Shiraishi, and A. Hishinuma, *Journal of Nuclear Materials* **133**, 540 (1985).
- [171] M. L. Grossbeck, *Effects of Radiation on Materials* (ASTM International, 2004).
- [172] T. Kimoto and H. Shiraishi, *Journal of Nuclear Materials* **132**, 266 (1985).
- [173] T. Katayama, K. Hasegawa, K. Kawanishi, and T. Tsushima, *J Appl Phys* **49**, 1759 (1978).
- [174] R. Hasegawa, *J Appl Phys* **45**, 4036 (1974).
- [175] Z. G. Li, D. J. Smith, E. E. Marinero, and J. A. Willett, *J Appl Phys* **69**, 6590 (1991).
- [176] A. Miotello and R. Kelly, *Nucl Instrum Methods Phys Res B* **122**, 458 (1997).
- [177] M. Ding and S. J. Poon, *Journal of Magnetism and Magnetic Materials* **339**, 51

(2013).

- [178] T. R. McGuire, R. J. Gambino, and R. C. Taylor, *J Appl Phys* **48**, 2965 (1977).
- [179] T. W. Kim, S. H. Lim, and R. J. Gambino, *J Appl Phys* **89**, 7212 (2001).
- [180] Y. Mimura, N. Imamura, and Y. Kushiro, *J Appl Phys* **47**, 3371 (1976).
- [181] R. Malmhäll, *J Appl Phys* **54**, 5128 (1983).
- [182] X. M. Cheng, S. Urazhdin, O. Tchernyshyov, C. L. Chien, V. I. Nikitenko, A. J. Shapiro, and R. D. Shull, *Phys Rev Lett* **94**, 017203 (2005).
- [183] S. HASHIMOTO, Y. OCHIAI, and K. ASO, *J Appl Phys* **66**, 4909 (1989).
- [184] B. Kaplan and G. A. Gehring, *Journal of Magnetism and Magnetic Materials* **128**, 111 (1993).
- [185] S. Kim, S. Lee, J. Ko, J. Son, M. Kim, S. Kang, and J. Hong, *Nature Nanotech* **7**, 567 (2012).